THESIS FOR THE DEGREE OF LICENTIATE OF ENGINEERING

High Temperature Corrosion of Superheaters in Biomass- and Waste-Fired Boilers: Combat on two fronts

Towards a better understanding of corrosion mechanisms and the development of solutions

Julien Phother-Simon

Department of Chemistry and Chemical Engineering

CHALMERS UNIVERSITY OF TECHNOLOGY

Gothenburg, Sweden 2019

High Temperature Corrosion of Superheaters in Biomass- and Waste-Fired Boilers: Combat on two fronts
Towards a better understanding of corrosion mechanisms and the development of solutions
Julien Phother-Simon

Department of Chemistry and Chemical Engineering
Chalmers University of Technology
SE-412 96 Gothenburg
Sweden
Telephone + 46 (0)31-772 1000

Cover:
(First row) Drawing: Schematic drawing of the experimental setup depositing KCl continuously.
(Second row) Left photograph: Photograph of 304L samples after 24 hours at 600 °C in 5%O_2 + 20%H_2O.
(Second row) Middle photograph: SEM image using BSE of the plan view of a "high amount of KCl"-area from a 304L sample, after 24 hours at 600 °C in 5%O_2 + 20%H_2O.
(Second row) Right photograph: SEM image using BSE of a cross-sectional view of a "high amount of KCl"-area from a 304L sample, after 24 hours at 600 °C in 5%O_2 + 20%H_2O.

ABSTRACT

Carbon dioxide is a greenhouse gas contributing to the greenhouse effect and a significant contribution comes from the use of fossil fuels. Utilizing more renewable fuels is therefore a solution to decrease the net release of CO_2 emissions to the atmosphere. This can be achieved by substituting fossil fuels, such as coal and oil, with renewable fuels, such as biomass and waste. However, the combustion of these renewable fuels releases corrosive species that deteriorate superheaters and other critical parts of the plants, resulting in lower electrical efficiency and higher maintenance costs. It is therefore necessary to understand and investigate the corrosion attack that occurs in this type of environment, in order to find sustainable material solutions.

The aim of this thesis is to increase knowledge on accelerated corrosion in biomass- and waste-fired boilers and to develop solutions that mitigate the corrosion.

In order to increase knowledge on accelerated corrosion in these environments, the corrosiveness of alkali salts (e.g NaCl or KCl) towards stainless steels has been investigated in several laboratory studies. However, a large discrepancy in corrosion attack has been observed between laboratory and field investigations. Therefore, a new setup was developed in laboratory in order to better mimic the boiler environment in a well-controlled manner. The present study involves two commercial stainless steels: 304L (18% Cr – 8% Ni type of alloy) and Sanicro 28 (higher chromium and nickel contents). The exposures were performed under continuous KCl deposition in an environment containing O_2 and H_2O at 600 °C for 24 hours. The results showed:
- Continuous KCl deposition caused a corrosion attack similar to the attack observed in boilers.
- Continuous KCl deposition accelerated the corrosion attack compared to pre-deposited KCl.
- Regions with large amounts of deposited KCl experienced faster corrosion.
- The alloy with higher chromium and nickel content exhibited an increased corrosion resistance in this environment.

Increasing knowledge on corrosion mechanisms is important for the development of efficient ways of mitigating corrosion. It is possible to mitigate a corrosion attack in two ways: improving the materials or changing the surrounding environment of the materials.

A solution to improving the materials is the utilization of coatings. Three different nickel-based coatings (NiCr, NiAl and NiCrAlY) HVAF (High Velocity Air Fuel)-sprayed onto a low-alloyed steel (16Mo3) were investigated. Their protectiveness was tested in two different environments for boiler purposes: A mildly corrosive environment ($O_2 + H_2O$) and a highly corrosive environment ($O_2 + H_2O + KCl$). The results showed that the NiCr coating did not remain protective since chlorides were detected within the coating and at the coating/substrate interface. In contrast, NiAl and NiCrAlY coatings performed well in both environments with minor oxidation.

The other approach to mitigating corrosion is changing the surrounding environment of the materials. A field study investigated the potential of a new superheater position in a boiler, predicted with CFD (Computational Fluid Dynamics) calculations. The impact of different operational parameters of the boiler on the deposit composition and amount were tested. The results showed that it is possible to decrease the amount of corrosive species (chlorides) in the deposits by changing the settings of the boiler. Moreover, the corrosion attack of a fixed installation of several superheater materials was investigated after 8000 hours. The analysis focused on 347H (18% Cr – 8% Ni type of alloy) material and revealed a corrosion attack similar to the new setup with continuous KCl deposition in laboratory.

Keywords: Oxidation, KCl, Stainless steels, Deposits, Ni-based coatings, Biomass, Waste

LIST OF PUBLICATIONS

This thesis is based on the following papers:

Paper I

J. Phother-Simon, T. Jonsson, J.Liske

"Continuous KCl addition in high temperature exposures of 304L – A way to mimic a boiler environment"

Manuscript

Paper II

J. Eklund, J. Phother, E. Sadeghi, S. Joshi, J. Liske

"High Temperature Corrosion of HVAF-Sprayed Ni-Base Coatings for Boiler Applications"

Submitted to Oxidation of Metals (2018)

Paper III

Maria Dolores Paz, Julien Phother-Simon, Lars Mikkelsen, Torbjörn Jonsson

"Increased steam temperature with Steamboost superheater – The effect of the combustion in deposits and high temperature corrosion"

Proceedings paper (Impact of Fuel Quality, Prague, 2016)

Statement of the author's contribution

Paper I: I was the main author of the paper and performed all the experimental and analytical work.

Paper II: I co-authored the paper and assisted in the corrosion tests and analyses of the exposed samples.

Paper III: I co-authored the paper and assisted in the microscopy analyses, the ion chromatography and the work performed in the boiler.

ACKNOWLEDGEMENTS

Contents

1. Introduction

Carbon dioxide is a greenhouse gas (GHG) contributing to the greenhouse effect. The principle of the greenhouse effect relies on GHGs confining the heat on Earth's surface. The more GHGs in the atmosphere, the more heat is confined, which makes Earth's climate livable. However, since the industrial revolution, humans have increased the concentration of carbon dioxide in the atmosphere more than a third [1]. Such a change usually occurs over thousands of years but is now happening over decades. This results in changes in the climate, such as more intense storms, drier droughts or changes faster than some living beings may be able to adapt to [1]. It is, therefore, necessary to decrease the amount of GHGs released to the atmosphere in order to minimize climate changes.

Consequently, several countries have agreed to mitigate the phenomenon [2, 3]. A significant contribution to the release of carbon dioxide to the atmosphere comes from the use of fossil fuels [1]. Utilizing more renewable fuels is, consequently, a solution to decrease the net release of CO_2 emissions to the atmosphere. However, the combustion of renewable fuels, such as biomass and waste, results in the formation of corrosive deposits and gases. From a corrosion point of view, the resulting flue gas contains mainly water vapor, alkali chlorides, and hydrogen chloride [4-10]. Such species are highly corrosive towards superheaters [11-22], resulting in lower electrical efficiency and higher maintenance costs. For powerplants using fossil fuels (e.g. coal-fired powerplants), the corrosion rate is considerably lower. Therefore, the steam temperature can be kept high e.g. 650 °C, while for biomass and waste powerplants, the range of temperature is kept between 350 and 550 °C [23]. However, one drawback is that electrical efficiency decreases as well when the steam temperature is reduced. For this reason, it is necessary to investigate these corrosion phenomena, in order to find suitable solutions.

The aim of this thesis is to increase knowledge on accelerated corrosion in biomass- and waste-fired boilers and to develop solutions in order to mitigate corrosion.

In order to increase the knowledge on the accelerated corrosion in biomass and waste boilers, several laboratories studies have investigated the corrosiveness of alkali salts such as NaCl or KCl [11-22]. However, there is substantial contrast in corrosion rates between field- and laboratory-exposed samples. The field samples encounter a considerable accelerated corrosion attack compared to the laboratory exposed samples. Therefore, the corrosiveness of a novel laboratory setup is investigated. This setup aims to better mimic the boiler environment in order to study the propagation of corrosion on stainless steels. Laboratory studies are usually performed with a fixed amount of KCl(s) deposited on the samples *ex-situ* prior to exposure [24] or with a layer of KCl(s) covering the sample [15, 21]. However, this rather static manner of applying the salt does not simulate the deposit formation that occurs on e.g.

superheater tubes in boilers. Therefore, a laboratory setup with continuous deposition of KCl(s) has been developed as an attempt to obtain a more corrosive environment, closer to boiler conditions.

Increasing knowledge on corrosion mechanisms is crucial for the development of efficient ways for mitigating corrosion. A corrosion attack can be mitigated in two ways: improving the materials or changing the surrounding environment of the materials.

Coatings are a solution to improve the materials. They may also be a good compromise between price and performance. However, at high temperatures, it has been observed that coatings encounter several issues, such as poor adhesion to the substrate or high levels of porosity [25, 26]. In order to improve the performance of coatings, a thermal spraying technique has been developed: HVAF (High Velocity Air Fuel). This technique has shown the ability to produce denser coatings with improved substrate adhesion [27-29]. Therefore, three different nickel-based coatings (NiCr, NiAl and NiCrAlY) HVAF (High Velocity Air Fuel)-sprayed onto a low-alloyed steel (16Mo3) were investigated. Their protectiveness was tested in two different environments for boiler purposes: A mildly corrosive environment (O_2 + H_2O) and a highly corrosive environment (O_2 + H_2O + KCl).

The second approach to mitigating corrosion is changing the environment surrounding the materials. A field study was conducted in order to investigate the potential of a new superheater position in a boiler, predicted with CFD (Computational Fluid Dynamics) calculations. Several different settings of the boiler were tested observe their influence on the deposits. Moreover, the corrosion attack of a fixed installation of several superheater materials was also investigated after 8000 hours of exposure in the boiler.

2. Biomass and waste fired boilers

The power production of plants, or so-called boilers utilizes the hot flue gas generated by the combustion of fuels, which is used to heat water to steam using several heat exchangers, such as superheaters and water walls. The superheated steam goes through a steam turbine for electrical power production.

Two types of boilers are commonly used for biomass and waste: Grate Firing boilers (GF) and Fluidized Bed Combustion (FBC) boilers.

Grate Firing boilers

Combustion occurs on a grate in this type of boiler. The fuel is added from the top of the grate and is transported to the bottom of the grate (e.g. with rotary or vibrating grates). Air is injected from below the grate in order to provide the combustion process with oxygen and reduce the temperature of the metal grate. This type of boiler exhibits good performance in burning low-moisture and high-alkali-content fuels. Moreover, difficult fuels, such as straw or high-alkaline-containing crops, are preferably burnt in this type of boiler rather than an FBC boiler due to the high agglomeration tendency of these fuels [30].

Fluidized Bed Combustion boilers

In this type of boiler, the fuel is combusted in a hot bed of particulate materials (mainly sand) and ash. The result is a blend of gas and solids that promote rapid heat transfer and chemical reactions within the bed. The fluidization of the bed is obtained by injecting air from the bottom of the bed. The type of fluidization of the bed depends on several parameters such as the velocity of the gas, particles' physical properties (size, shapes, and density) or the bed's geometries. Among the different regimes of fluidization that can be defined, two of them are widely used: Bubbling Fluidized Bed (BFB) and Circulation Fluidized Bed (CFB). CFB boilers display a higher efficiency than BFB boilers due to the solid separators that recycle unburnt particles to the lower part of the furnace.

Fluidized Bed technology exhibits good fuel flexibility [30].

Fuels in biomass and waste boilers

The substitution of fossil fuels with renewable fuels in power plants is a way of reducing the net emission of CO_2 released to the atmosphere. Several countries, such as Sweden, have decided to make a change concerning the fuels used in power plants. The tendency is that the amount of biomass and waste used as an alternative fuel keeps increasing [3, 31]. An example of this trend can be seen in the Händelö plant located in Norrköping, Sweden, where total substitution of fossil fuels with renewable fuels has almost been achieved (Figure 1):
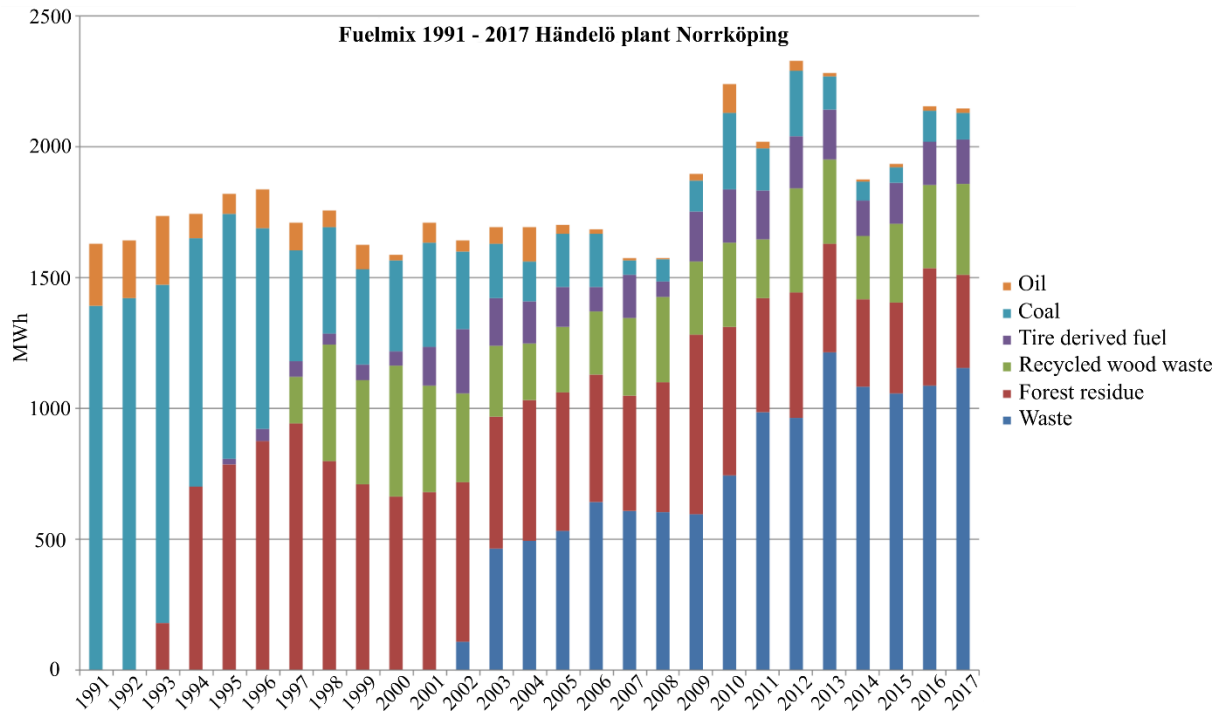
Figure 1: Power generation by fuel type from 1991 to 2017 at the Händelö plant (owned by E.ON Värme AB) in Norrköping, Sweden [32].

However, the change in fuels is not without consequences; as the composition of renewable fuels are different from fossil fuels, the flue gas produced during combustion is also different. Compared to fossil fuels, the content of water vapor and alkali chlorides is higher in biomass- and waste-fired plants, which results in a higher level of hydrochloric acid (HCl) and a lower level of sulfur dioxide (see Table 1). It has been reported that the severe corrosion attack encountered in biomass- and waste fired-boilers is usually due to the presence of alkali chlorides in the flue gas, as well as in a chlorine-containing environment [11-21]. Critical parts of a power plant, such as superheaters and water walls, are severely damaged by the corrosion processes that occur at high temperatures in such environments.

Table 1: Approximate flue gas composition (volume %) in waste-, biomass- and coal-fired boilers [4-10].

Fuel	O_2 (%)	H_2O (%)	SO_2 (ppm)	HCl (ppm)	KCl + NaCl (ppm)
Coal	~ 4-5	~ 4-16	~ 400-1200	~ 10-50	-
Biomass	~ 5-10	~ 10-20	~ 0-70	~ 25-1000	~ 5-50
Waste	~ 5-11	~ 10-20	~ 0-150	~ 250-1300	< 120

3. Oxidation theory

3.1. Thermodynamics

Non-noble metals are prone to be thermodynamically unstable when surrounded by a gas-containing environment. This results in the formation of oxides, carbides, nitrides, sulfides, or mixtures, depending on the composition of the surrounding environment [33]. With oxidation, the chemical reaction occurring between the metal M and oxygen O is as follows:

$$xM(s) + \left(\frac{y}{2}\right)O_2(g) \rightarrow M_xO_y(s) \tag{1}$$

In order to ascertain if the formation of an oxide will spontaneously occur, one can look at the change in Gibbs free energy ΔG under constant pressure and temperature. The value of Gibbs free energy reveals if the reaction will occur spontaneously or not:

- If ΔG < 0, the reaction will occur spontaneously.
- If ΔG > 0, the reverse reaction is favored.
- If ΔG = 0, the system is at equilibrium state and no reaction is favored.

Gibbs free energy is expressed via the following equation:

$$\Delta G = \Delta G^0 + RTln\left(\frac{a_{M_xO_y}}{(a_M^x)\left(a_{O_2}^{\frac{y}{2}}\right)}\right) \tag{2}$$

Where ΔG^0 is the standard Gibbs free energy, R is the universal gas constant, T is the temperature, and a is the activity of the products and reactants. The activities of solids are approximatively equal to 1, and the activities of gases are equal to their respective partial pressure. The equation can be simplified at equilibrium (when $\Delta G = 0$):

$$\Delta G° = RTln(p_{O_2}^{y/2}) \tag{3}$$

The partial pressure of oxygen at equilibrium is called the equilibrium partial pressure or dissociation pressure. An oxide will be formed only if the partial pressure of oxygen at a given temperature is higher than the equilibrium partial pressure of oxygen at the same given temperature. In order to predict if a metal will oxidize or if an oxide will be reduced, plotting the ΔG° of the formation of an oxide as a function of temperature results in the Ellingham diagram (Figure 2). This diagram shows if the formation of an oxide is thermodynamically favorable at a given temperature and partial pressure of oxygen. The lower the ΔG° is, the more stable the oxide is. The slopes of the lines are positive, which means that oxides become more unstable when the temperature increases. However, this diagram does not provide any information on the kinetics of the reactions (or growth rate).
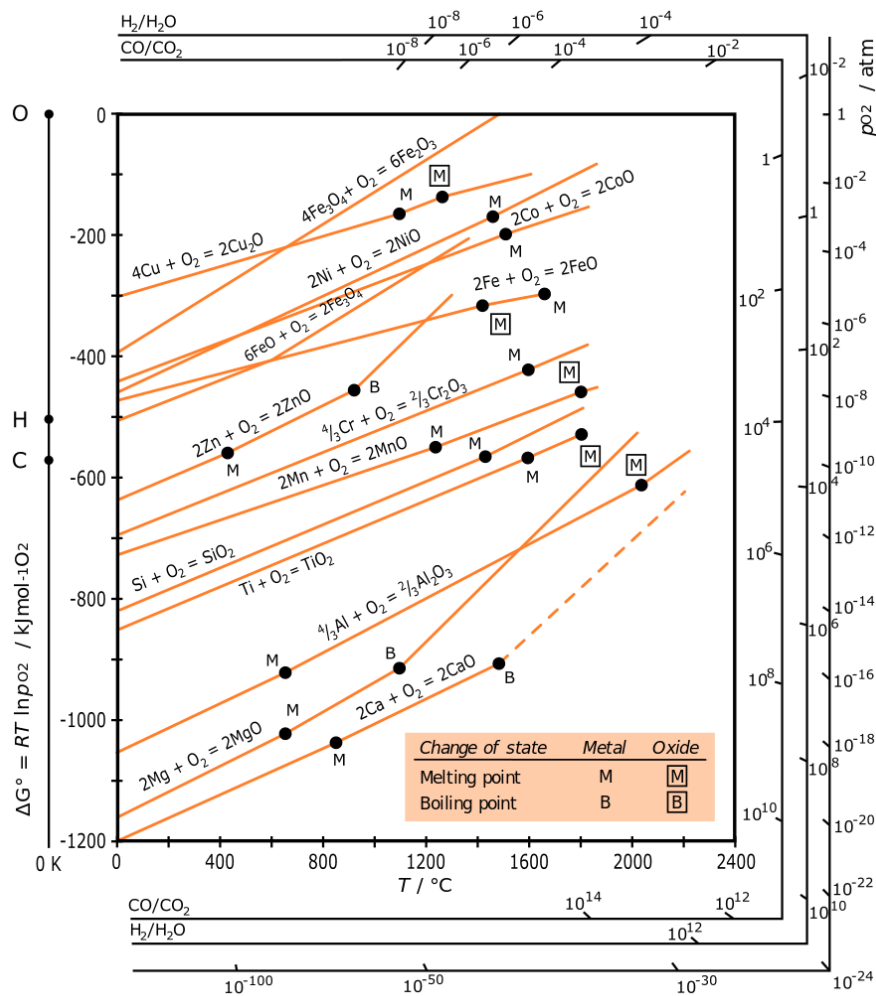
Figure 2: Ellingham diagram of various oxides [34].

3.2. Oxide formation

The oxidation process starts with the adsorption of oxygen on the surface of a metal. The adsorption and oxide formation steps are both influenced by crystal defects at the surface, surface preparation, surface orientation, and impurities in the metal and gas [33]. The oxide will keep growing until a continuous film covers the surface. The reaction can then proceed only through solid-state diffusion of the reactants through the film. However, crack formation within the oxide scale may expose unprotected areas of the substrate to the environment, leading to an acceleration of the oxidation rate. A schematic drawing in Figure 3 illustrates this process. The initial steps of oxidation are rather fast even at room temperature, however, once the continuous layer has formed, the oxidation rate decreases drastically as the diffusion rates are very slow at this temperature. However, as the temperature increases, so do the diffusion rates.
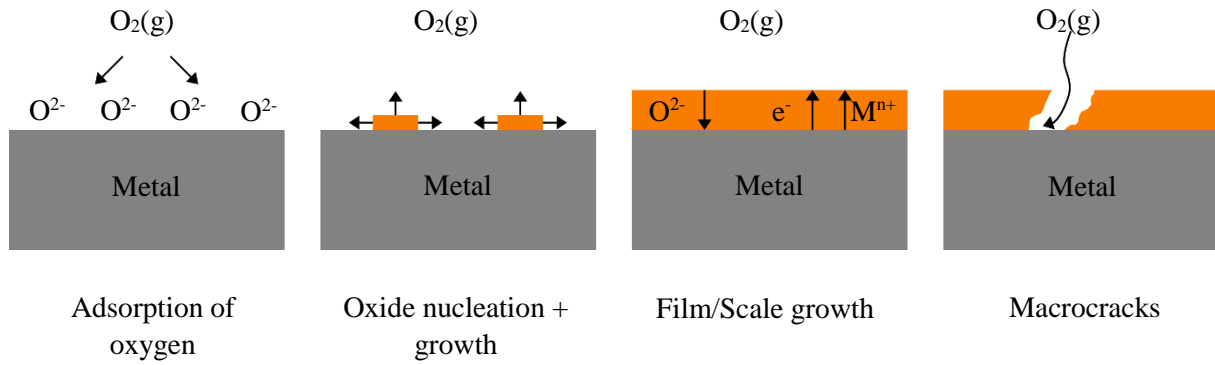
Figure 3: Schematic illustration of the oxidation process (after [33]).

3.3. Diffusion processes

When a continuous oxide film has been formed, the growth of the scale occurs through solid-state diffusion of reactants (atoms, ions, and/or electrons). Their transport depends on the presence of defects within the oxide. All metals and oxides have defects that can be grouped into three types: point defects (e.g. vacancies and interstitials), linear and planar defects (e.g. dislocations and grain boundaries) and bulk defects (e.g. precipitates and voids). Point, linear, and planar defects can combine with each other and lead to two different types of compounds: stoichiometric and non-stoichiometric.

In stoichiometric compounds, the proportions of the elemental composition can be expressed with whole numbers [35]. Alumina (Al_2O_3) is an example of a compound close to ideal stoichiometry as it exhibits a low defect content, which results in a continuous and dense layer once an oxide has formed. In a stoichiometric crystal, the defects present in the oxide must maintain electro-neutrality, which is the case for Frenkel and Schottky defects (see Figure 4) [33]. The Frenkel defect consists of a cationic vacancy and an interstitial cation, while the Schottky defect consists of a cationic vacancy and an anionic vacancy [33].
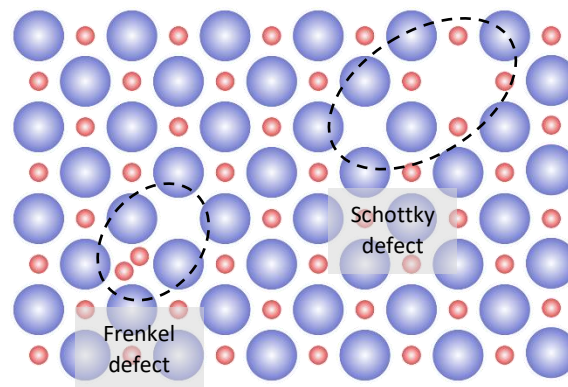
Figure 4: Schematic drawing of the Frenkel and Schottky defects(after [36]).

However, most compounds are non-stoichiometric and exhibit an excess or deficit of either oxygen or metal, e.g. FeO (wüstite) commonly written $Fe_{1-x}O$, where a deficit of metal is dominant. The compound is, therefore, considered as a semi-conductor. By definition, there are two types of semi-conductors [33]:

- The p-type semiconductor: Electric conductivity is due to the formation of electron holes caused by the removal of metal ions or the addition of oxygen ions. The charge is transferred by positive carriers.

- The n-type semiconductor: Electric conductivity is due to the formation of concentrations of electrons caused by the removal of oxygen ions or the addition of metal ions. The charge is transferred by negative carriers.

This classification allows the prediction of the electrical properties of an oxide and, therefore, a better understanding of the diffusion mechanisms through the oxide. For example, FeO (wüstite) shows a deficit of metal, which is considered as a cation vacancy, resulting in the charge being transferred by positive carriers, holes. The oxide is, therefore, a p-type semiconductor that grows outward.

Defects within the oxide also allow the transport of atoms or ions through the oxide scale, which is called diffusion. This phenomenon occurs in two different ways: lattice diffusion and short-circuit diffusion [33].

Lattice diffusion:

This type of diffusion occurs within the bulk material due to the presence of point defects leading to several diffusion mechanisms (Figure 5):

- The interstitial mechanism: The migration of an atom or ion at an interstitial site to a neighboring interstitial site. This mechanism has a higher probability of occurring when the interstitial ion or atom is smaller than the atoms located at the lattice sites.

- The vacancy mechanism: The migration of an atom or ion at a normal lattice site to a neighboring unoccupied lattice site. This results in a vacancy created where the atom or ion was located, which can be interpreted as a vacancy migration.

- The interstitialcy mechanism: The migration of an interstitial ion or atom to a normal lattice site, which causes the original ion or atom at that lattice site to migrate to a neighboring interstitial site.
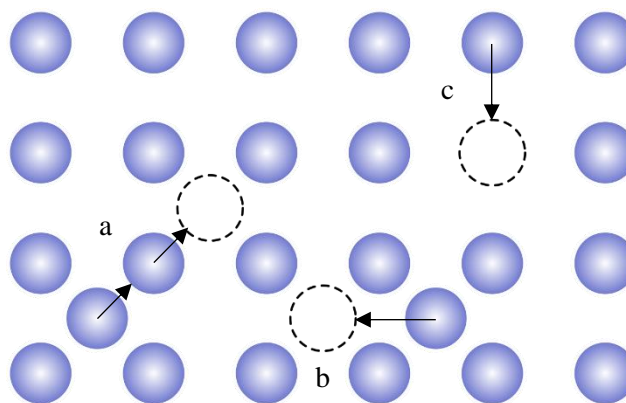
Figure 5: Representation of a) interstitialcy diffusion, b) interstitial diffusion and c) vacancy diffusion (after [37]).

Short-circuit diffusion

This type of diffusion takes place within two-dimensional defects, such as grain boundaries and dislocations. These defects can be seen as fast transport paths through the oxide, as the diffusion coefficients are higher than lattice diffusion. The activation energies for short-circuit diffusion are 0.5-0.7 times those for lattice diffusion [33]. Therefore, this type of diffusion is dominant at low temperatures, which is considered to be below 0.8 times the melting temperature of the alloy/metal [38]. Lattice diffusion increases with increasing temperature, while the short-circuit diffusion contribution diminishes until it becomes negligible once a temperature close to the melting temperature of the alloy/metal is reached. However, in this thesis, short-circuit diffusion is considered as the investigations were performed at 600 °C or below.

3.4. Oxidation kinetics

While thermodynamics indicates if a reaction may occur spontaneously in a given environment, kinetics provides information about the rate of this reaction in the same given environment. In oxidation, kinetics reveals how fast a metal or an alloy oxidizes. Plotting the weight change of a sample as a function of time results in a mass gain curve. This mass gain is caused by oxygen uptake during oxide formation. There are three main ideal oxidation rate behaviors: linear, parabolic, and logarithmic (Figure 6). However, a combination of these behaviors is required in order to explain the mass gain curves observed in experimental studies. Breakaway behavior illustrates well this phenomenon due to the interaction of the protective oxide scale (primary protection) with the environment, such as the formation of potassium chromates (see Section 6.2) or the spallation of the oxide scale, which leads to the breakdown of this primary protection.
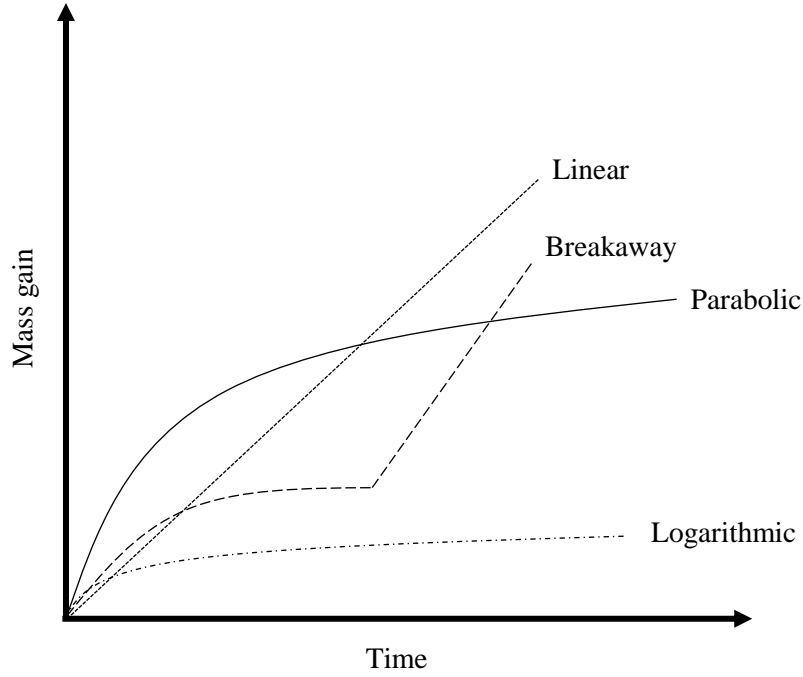
Figure 6: Various kinetic laws of metal oxidation

3.4.1. Linear behavior

Linear behavior exhibits a constant oxidation rate. This is due to the rate-limiting step being a surface or a phase boundary process or reaction, such as the adsorption of oxygen on a metal surface. It is common to observe this behavior at early stages of the oxidation process or in thin or highly porous oxides [33].

This behavior can be expressed by the following equation:

$$x = k_l t \tag{4}$$

where x is the oxide thickness, k_l is the linear rate constant and t is the time.

3.4.2. Parabolic behavior

Parabolic behavior is the most common behavior observed for metals at high temperature. The rate-limiting step is the transport of ions (or electrons) through an oxide scale. As the thickness of the oxide scale increases, the diffusion rates decrease, resulting in a lower oxidation rate.

This behavior can be expressed by the following equation formulated by Carl Wagner [39]:

$$x^2 = k_p t + C \tag{5}$$

where x is the oxide thickness, k_p is the parabolic constant, t is the time and C is the integration constant.

Carl Wagner based this model on the following assumptions:

- The oxide formed is compact and adherent.
- The transport of ions and electrons is the rate-limiting step.
- Equilibrium is established at both, the metal/oxide and oxide/gas interfaces.

10

- Equilibrium is also established within the oxide.
- The oxide shows only small deviations from stoichiometry.
- Oxygen solubility within the metal can be neglected.

3.4.3. Logarithmic behavior

Logarithmic behavior is commonly observed at low temperatures, generally below 300-400 °C [33]. A fast oxidation rate can be seen in the early stages, followed by a drastic decrease in the oxidation rate. The rate-limiting step is still being discussed but some possible explanations have been suggested e.g. the transport of ions or electrons due to electric fields [33].

This behavior can be expressed by the following equation:

$$x = k_{log} \log(t + t_0) + A \tag{6}$$

where x is the oxide thickness, k_{log} is the logarithmic rate constant, t is the time and A is a constant.

3.4.4. Breakaway behavior

Breakaway behavior occurs when an alloy or metal exhibiting either a parabolic or logarithmic behavior, loses its primary protection (the protective oxide layer) through the spallation of the oxide layer, cracks within the layer, or the breakdown of the protective layer via interaction with the environment. This results in a fast-growing secondary protection (a fast-growing oxide) leading to accelerated corrosion, as seen by the sudden increase in mass gain. The fast-growing oxide dictates the corrosion behavior of the alloy from that point on. Thus, the oxide layers formed as a result of the breakaway can be labelled as secondary protection.

4. Materials

4.1. Steels

Pure iron is a ductile material. Iron has three allotropic forms: ferrite (α), which has a body-centered cubic (bcc) structure, austenite (γ), which has a face-centered cubic (fcc) structure, and δ, which is a body-centered cubic.

However, by adding small amounts of carbon to the iron the material becomes less ductile as the movement of dislocations within the crystal structure are restrained. Carbon has therefore a role as a hardening agent. Consequently, carbon enhances the mechanical properties of the material, such as hardness, yield strength, or tensile strength [40]. These solid solutions of iron and carbon are defined as steels.

Other elements can be added in order to change the final properties of the steel and promote the stabilization of a phase. For example, adding titanium, chromium, molybdenum, or aluminum will stabilize the ferritic phase at room temperature, while adding silicon, manganese, nickel, or carbon will stabilize the austenitic phase at room temperature. The stabilization of the phases is caused by the added elements that share the same crystal structure with the corresponding allotropic form. Not only do alloying elements promote the stabilization of one phase, but they also change the final properties of the steel. Chromium is the most important alloying element with respect to corrosion. Chromium improves the corrosion resistance properties of steels, leading to a type of steel commonly called stainless steel. This resistance comes from the ability of stainless steels to form a chromium-rich oxide layer on top of the alloy, protecting it from further oxidation. The minimum chromium content of ferritic stainless steels is 10.5 %, while it is 18 % for austenitic stainless steels. Ferritic stainless steels and austenitic stainless steels are the most common steels used in industry. They have totally different properties due to their crystal structure, which make them suitable for specific applications.

4.2. Materials investigated

This study focused on two commercial austenitic stainless steels, 304L and Sanicro 28 (higher nickel and chromium content than 304L) in the first part. In the second part, nickel-based coatings (NiCr, NiAl and NiCrAlY) thermally sprayed over a low-alloyed steel (16Mo3) were investigated. Finally, another commercial austenitic stainless steel, 347H, was investigated in the field exposure. The chemical compositions of these materials are given in Table 1.

Table 2: Chemical compositions (wt%) of the different materials investigated (First table: stainless steels. Second table: coatings and substrate)

Material	Fe	C	Cr	Ni	Mn	Si	Mo	N	Cu	P	S	Al	Nb
304L	Bal.	0.02	18.5	10.2	1.41	0.55	-	0.08	-	-	-	-	-
347H	Bal	0.05	17.7	10.1	1.6	0.57	-	-	-	0.03	0.002	-	0.64
Sanicro 28	Bal.	0.02	27	31	1.77	0.6	3.5	-	1	0.02	0.001	-	

Material	Fe	C	Cr	Ni	Mn	Si	Mo	Al	Y	O
16Mo3	Bal.	0.15	0.01	-	0.5	0.3	0.3	-	-	-
NiCr	-	-	21.3	Bal.	-	-	-	-	-	0.1
NiAl	-	-	-	Bal.	-	-	-	5.7	-	0.2
NiCrAlY	-	-	21.2	Bal.	-	-	-	7.3	0.9	0.2

304L:

The 304L grade steel is the most widely used commercial stainless steel and was supplied by Outokumpu. Its low carbon content (<0.03 wt.%) denoted by "L", compared to its higher carbon content grade (<0.08 wt.%) gives it the ability to minimize the precipitation of chromium carbides. These carbides would deplete the chromium content within the steel, which leads to a weaker corrosion resistance.

Sanicro 28:

This grade of austenitic stainless steel is often used in highly corrosive environments and was supplied by Sandvik. Compared to 304L, both chromium and nickel content are higher. Sanicro 28 exhibits good resistance to stress-corrosion cracking (usually not the case for austenitic stainless steels) and to high temperature corrosion.

16Mo3:

This low-alloyed steel grade is a ferritic steel. It is widely used in powerplants, exhaust systems, and incineration plants. It is known for its good mechanical properties up to 500 °C and a low price compared to stainless steels. However, due to its low content of chromium, this alloy is unable to form a chromium-rich oxide layer. Thus, its corrosion resistance is due to an iron-oxide layer, which is less protective than chromium-containing alloys.

Coatings NiCr, NiAl and NiCrAlY:

These three commercial gas-atomized powders were supplied by H.CStarck GmBH and were used for spraying on a 16Mo3 substrate. The powders had a particle size distribution of 45±22 µm.

5. Corrosion products

Understanding the properties of the corrosion products is relevant in order to increase knowledge on corrosion mechanisms that occur when metals or alloys are exposed to certain environments. The corrosion products resulting from the interaction of the materials and the environments investigated will be discussed in the next section. The corrosion products were observed in both boiler and laboratory environments.

Chemical composition and microstructure vary between the materials investigated, which leads to differences in the corrosion mechanisms and the oxide scales formed.

5.1. Oxides in high-temperature corrosion

Oxides play a major role in the corrosion resistance of metals and alloys. Depending on the composition, the oxides differ in ion diffusivities, crystal structure, and, consequently, corrosion resistance. An oxide is considered protective when it exhibits the following properties [41]:

- Good adhesion to the substrate
- Dense and continuous layer
- Slow growth rate
- Similar thermal expansion coefficients between the substrate and the oxide
- Low electrical conductivity and low diffusion coefficients for metal ions and oxygen
- High melting point
- High temperature plasticity

The crystal structure of many oxides formed at high temperatures mainly consists of cubic and hexagonal close-packed oxygen ions, with metal ions located at interstitial sites. The properties of the most important corrosion products investigated herein are described below [33]:

Wüstite – $Fe_{1-y}O$

Wüstite has a rock salt structure: iron and oxygen atoms form sub-lattices of a cubic close-packed type. It is only stable above 570 °C and in low oxygen-activity environments. Wüstite is a highly non-stoichiometric oxide due to metal vacancies, since the non-stoichiometry varies between $Fe_{0.85}$ and $Fe_{0.95}$. Based on previous observations, wüstite is a p-type semiconductor. The presence of many defects results in a high mobility for ionic transport [33]. The presence of chromium in an alloy hinders the formation of wüstite.

Magnetite – Fe_3O_4

Magnetite has the inverse spinel structure at and below room temperature. The distribution of the divalent and trivalent iron ions becomes randomized between the octahedral and tetrahedral sites at higher temperatures. At high oxygen activity, magnetite is metal-deficient, which makes it a p-type semiconductor. However, at low oxygen activity, metal excess becomes dominant, making magnetite a N-type semiconductor [33].

Hematite – Fe_2O_3

Hematite has a corundum structure, where the oxygen atoms form a slightly distorted hexagonal close packing, in which two-thirds of the octahedral sites are occupied by iron atoms [33].

The non-stoichiometry of hematite is small with oxygen deficiency, which makes it a n-type semiconductor in the range of 650-800 °C, and a p-type semiconductor at higher temperatures.

General corrosion properties of iron oxides

The formation of these three oxides depends on oxygen activity and temperature. From a corrosion point of view, wüstite is the least protective oxide among the three, magnetite comes in second place, while hematite is the most protective.

Eskolaite – Cr_2O_3

Eskolaite, or chromia, has the corundum structure and is considered to be a p-type semiconductor. Eskolaite is a slow-growing and dense oxide that has a small amount of defects compared to iron oxides, which makes it eligible as a protective oxide [33]. The formation of eskolaite is the reason why chromium is added to steels to obtain corrosion resistant steels called stainless steels.

General corrosion properties of Cr-containing oxides

Of the stainless steels studied, eskolaite usually forms a mixed solid solution with hematite, resulting in $(Fe_{1-x}Cr_x)_2O_3$.

Spinel-type solid solution – $(Fe,Cr,Ni)_3O_4$

Oxides based on iron, chromium and nickel may form solid solutions with a spinel-type structure. It is a complex structure that consists of cubic closed-packed oxygen atoms and metal ions that occupy the tetrahedral and octahedral sites. Divalent cations (e.g Fe, Zn, Ni, Mn, Mg) are located at the tetrahedral sites and the trivalent cations (e.g Fe, Cr, Al) are located at the octahedral sites. The composition of a spinel-type solid solution depends on the amount of those elements as well as the oxygen activity at the oxide/metal interface.

General corrosion properties of spinel type oxides

It has been shown that in the case of 304L at 600 °C in a corrosive environment, the spinel oxide region formed is more complex and consists of regions of spinel oxide and regions of mixed metal/oxide. This characteristic microstructure may influence the properties/oxidation in the following ways [42]:

- A network of interfaces between oxide/metal and oxide/oxide is created and may act as fast transport paths for ions.

- Regions rich in iron and nickel may become voids after playing the role of sources of ions for the outward growing oxide [43]. The voids created within the spinel may contribute and cause spallation.

Alumina – Al_2O_3

Alumina exists mostly in two allotropic forms: α-Al_2O_3 and γ-Al_2O_3. α-Al_2O_3 has a corundum structure with oxygen atoms forming a hexagonal close packing, where two-thirds of the octahedral sites are occupied by aluminum atoms.

γ-Al_2O_3 exhibits the cubic structure and usually forms below 900 °C and is a transient oxide (not thermodynamically stable). After 900 – 1000 °C γ-Al_2O_3 changes to α-Al_2O_3, the only thermodynamically stable form of alumina. α-Al_2O_3 has a high degree of stoichiometry due to its high lattice energy and large bandgap, resulting in a very low concentration of defects [33]. Consequently, the diffusion rates of ions through the oxide are low, leading to a slow growing oxide. α-Al_2O_3 therefore exhibits high corrosion resistance.

5.2. Metal chlorides

When exposed to a chlorine-containing environment, such as alkali chlorides (KCl, NaCl…), hydrochloric acid, or chlorine, metals can react and form metal chlorides ($FeCl_2$, $FeCl_3$, $CrCl_2$, $CrCl_3$ and $NiCl_2$). Thermodynamic phase stability diagrams of the systems Fe-O_2-Cl_2, Cr-O_2-Cl_2, and Ni-O_2-Cl_2 at 600 °C are shown in Figure 7. Based on the date in these diagrams, metal chlorides are stable when oxygen activities are low, which corresponds to metal/oxide interface conditions where they are usually detected [44].
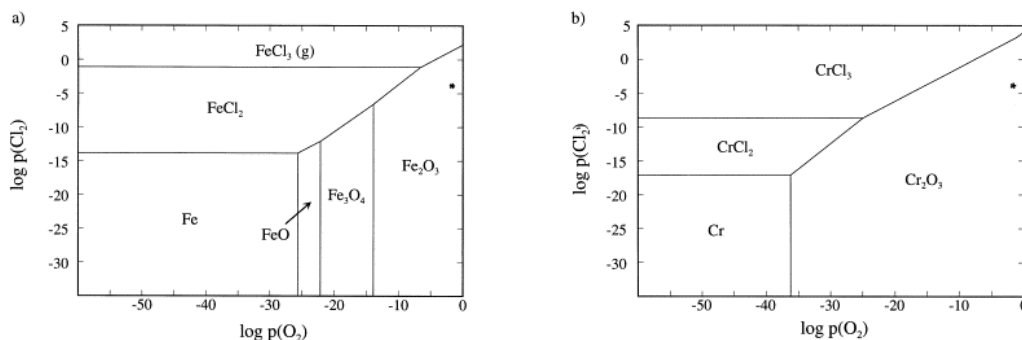
Figure 7:Thermodynamic stability diagrams of the systems Fe-O_2-Cl_2 (a), Cr-O_2-Cl_2 (b) and Ni-O_2-Cl_2 (c) at 600 °C [44].

6. Corrosion mechanisms

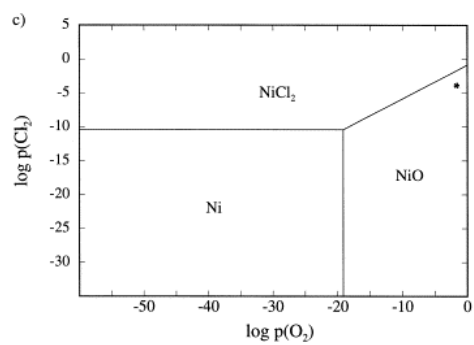The corrosion resistance of stainless steels is primarily attributed to the chromium present in the alloy, forming a chromium-rich oxide layer on top of the bulk material. This layer is the first protective feature that separates and protects the substrate from the environment.

The introduction of biomass and waste in boilers has exhibited accelerated corrosion attacks on superheaters, compared to traditional coal-fired boilers. For this reason, the protective layer deteriorates faster, exposing the substrate to the surrounding environment. The composition of the fuel is the reason the breakaway of this protective layer happens; the breakaway is caused by the release of many corrosive compounds.

In the following sections, the mechanisms that cause an accelerated corrosion of the investigated materials are described.

6.1. Chromium evaporation

The effect of water vapor on chromium containing alloys has been intensively investigated [45-49]. The corrosion resistance of stainless steels relies on the formation of a chromium-rich oxide scale (primary protection) on top of the bulk material. This layer is formed when the stainless steel is exposed to a dry atmosphere containing typically 5% O_2 at 600 °C for 24 hours [22]. Introducing water vapor into the environment may deteriorate the protective layer following the reaction below:

$$Cr_2O_3(s) + 2H_2O(g) + 3/2O_2(g) \rightleftharpoons 2CrO_2(OH)_2(g) \tag{7}$$
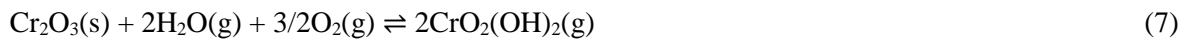
The formation and evaporation of chromic acid may, therefore, deplete the chromium-rich oxide in chromium. However, its protectiveness remains until the depletion of chromium becomes too substantial. This may lead to breakaway corrosion where an iron-rich oxide scale (secondary protection) begins to grow rapidly, instead of the chromium-rich slow-growing scale.

The supply of chromium occurs via grain boundaries diffusion at 600 °C, which explains the morphology of the corrosion products observed, for example, after exposure in O_2 and H_2O for 168 hours, as shown in Figure 8 [47]. As the transport of chromium is faster at the grain boundaries, the surrounding area is more protected than the center of a grain. This explains the island-like shape of the growing oxides on top of the substrate, where the iron oxide becomes thicker towards the center of the grain and thinner towards the grain boundaries. The cross section in Figure 8b) shows that the island-like feature consists of an outward-growing scale, which is hematite (Fe_2O_3), and an inward-growing scale which is a spinel-type oxide (($Fe,Cr,Ni)_3O_4$) [47].
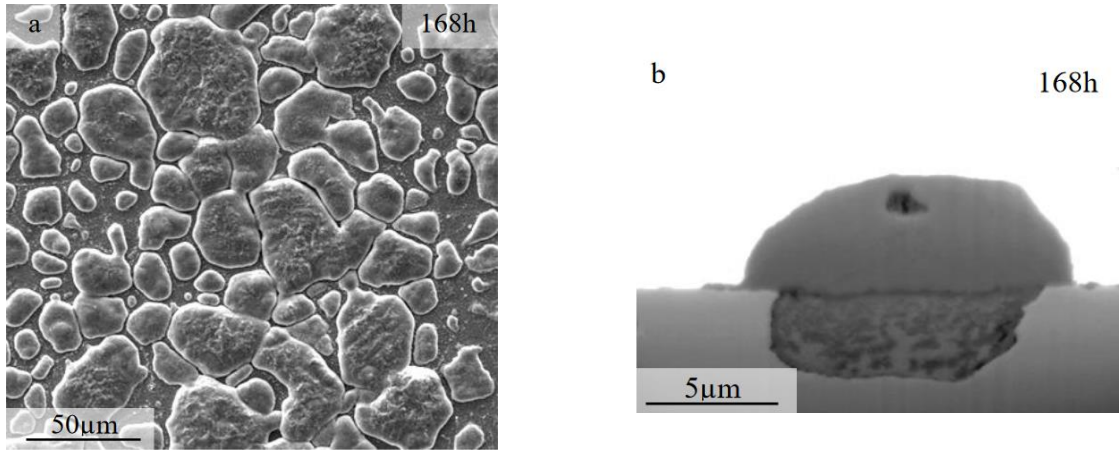
Figure 8: a) SE images of 304L samples exposed to 5% O2 and 40% H2O for 168h at 600 °C and b) BSE images of FIB cross-sections of an oxide island [47].

6.2. Alkali chromate formation

The amount of alkali chlorides in biomass and waste is considerably higher than fossil fuel [50-52]. The combustion of biomass and waste releases alkali chlorides in a volatile form, which is part of the flue gas that approaches the superheaters. A typical flue gas composition of biomass- and waste-fired boilers is given in Table 1 [4-10].

It has been shown that breakaway of the protective layer occurs in the presence of alkali compounds [20-22]. This phenomenon occurs due to the reaction between the alkali ion and the chromium-rich oxide, which leads to the depletion of chromium from the primary protection:

$$Cr_2O_3(s) + 4KCl(s) + 2H_2O(g) + 3/2O_2(g) \rightleftharpoons 2K_2CrO_4(s) + 4HCl(g) \qquad (8)$$

If the depletion of chromium from the primary protection becomes too substantial, breakaway of the protective layer occurs, leading to the growth of an iron-rich fast-growing oxide scale (secondary protection). The loss of the primary protection followed by the rapid growth of the secondary protection is a rather fast process. Thus, the overall corrosion resistance of stainless steels in alkali rich environments is often dictated by the properties of the secondary protection.

6.3. Active oxidation or chlorine cycle

Active oxidation (or the chlorine cycle) is a mechanism that was suggested first by McNallan [53] and was extended by Grabke [13]. It involves the transport of chlorine (Cl_2) from the oxide/gas interface to the metal/oxide interface. Chlorine is considered to be more aggressive than HCl during short-time exposures [54]. The presence of chlorine is obtained through the reaction of alkali chlorides with the oxide scale, or through the oxidation of HCl (the Deacon process) [13]:

$$4NaCl(s) + Cr_2O_3(s) + 5/2O_2(g) \rightleftharpoons 2Na_2CrO_4(s) + 2Cl_2(g) \qquad (9)$$

$$2NaCl(s) + Fe_2O_3(s) + 1/2O_2(g) \rightleftharpoons Na_2Fe_2O_4(s) + Cl_2(g) \qquad (10)$$

$$2HCl(g) + 1/2O_2(g) \rightleftharpoons Cl_2(g) + H_2O(g) \qquad (11)$$
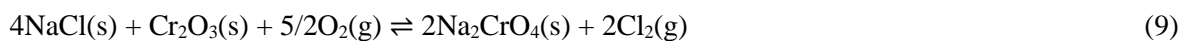
When chlorine gas penetrates the oxide scale, it reacts with the substrate and forms corresponding chlorides at the metal/oxide interface. As the oxygen pressure is low at this interface, the formation of metal chlorides is favorable:

$$Fe(s) + Cl_2(g) \rightleftharpoons FeCl_2(s) \qquad (12)$$

At this temperature, the equilibrium vapor pressure of metal chlorides is considerable (e.g. $p(FeCl_2)$ = 4.10^{-5} bar at 500 °C [13]), which results in the continuous evaporation of the species that diffuses through the oxide scale via cracks and pores. The gradient of oxygen pressure between the bulk material and the environment oxidizes the metal chlorides to Fe_3O_4 and/or Fe_2O_3 in regions with a higher oxygen pressure (towards the environment):

$$3FeCl_2(g) + 2O_2(g) \rightleftharpoons Fe_3O_4(s) + 3Cl_2(g) \qquad (13)$$

$$2FeCl_2(g) + 3/2O_2(g) \rightleftharpoons Fe_2O_3(s) + 2Cl_2(g) \qquad (14)$$

Based on the reactions 13 and 14, the released chlorine may either go through the same process described previously (chlorine cycle) or return to the surrounding atmosphere.

The active oxidation is suggested to explain the acceleration of corrosion in the presence of chlorine-containing species. However, one aspect of the suggested mechanism has not been fully explained; this is the diffusion of $Cl_2(g)$ through the oxide scale. Active oxidation starts with almost no incubation time after the introduction of HCl or alkali chlorides onto the sample. Therefore, the authors ([13]) have suggested that chlorine must use fast diffusion paths. However, if a molecule of chlorine is able to reach the interface via molecular diffusion through cracks and pores, then the molecule of oxygen (264 pm) should also be able to do so because it is smaller than $Cl_2(g)$ (396 pm). The activity of oxygen may, therefore, be too high to form metal chlorides at the metal/oxide interface. The outward diffusion of metal chlorides is also debatable as metal chloride molecules are larger than $Cl_2(g)$. Another issue is the prediction that metal chlorides must be located at the metal/oxide interface where oxygen activity should be sufficiently low. However, chlorine-rich areas have also been found in the outer part of the scale [55].

6.4. Electrochemical approach

This approach [56] involves a flux of anions and cations related to an electronic current, instead of the transport of gaseous chlorine species through an oxide scale. The formation of Cl^- is suggested to occur on the surface of the oxide via the reduction of $Cl_2(g)$ as shown below, and the formation of electrons via metal oxidation:

$$Cl_2(g) + 2e^- \rightarrow 2Cl^-(ads) \tag{15}$$

$$M(s) \rightarrow M^{n+} + ne^- \tag{16}$$

Chloride ions may also be produced from HCl and alkali chlorides[57]:

$$2HCl(ads) + 1/2O_2(ads) + 2e^- \rightarrow H_2O(g) + 2Cl^-(ads) \tag{17}$$

$$2KCl(s) + 1/2O_2(g) + H_2O(g) + 2e^- \rightarrow 2KOH(g) + 2Cl^-(ads) \tag{18}$$
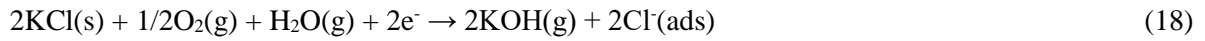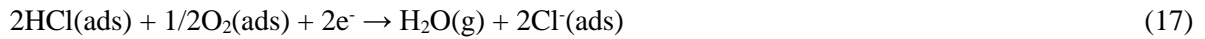
Considering that case, the present authors suggested that chloride ions have high mobility on the surface of the oxide. The grain boundaries of the oxide may be considered as internal surfaces that allow chloride ions to behave in the same way as on a surface [58]. This enables access to the metal/oxide interface and, therefore, the formation of metal chlorides. However, it has been reported that metal chlorides could also be located within the oxide scale [56], which agrees with findings that metal chlorides are not only located at the metal/oxide interface [55]. Their position is determinated by the speed of the inward and outward transports of chloride ions and cations respectively.

7. Experimental setup and strategy

In order to understand the corrosion mechanisms that occur in biomass and waste boilers, it is necessary to investigate both simple (laboratory) and complex (field) environments. Investigations performed in laboratory allow a more simplified and well-controlled environment, while field investigations allow the direct observation of the corrosiveness in a boiler environment. Thus, laboratory exposures allow the study of single parameters, such as water vapor content or a specific salt, in order to understand the role of each in the corrosion mechanisms that occur in biomass and waste boilers. Both types of investigation aim to increase knowledge on corrosion mechanisms and to develop solutions for mitigating corrosion.

7.1. Investigation of accelerated corrosion caused by continuous KCl addition

Due to the complex environment present in a boiler, it is necessary to perform laboratory exposures in order to understand precisely the influence of different parameters. This study investigates the corrosiveness of a setup that continuously deposits KCl on samples during exposures. Two commercial stainless steels were used: 304L and Sanicro 28 (higher chromium and nickel contents). The chemical compositions of the materials investigated are listed in Table 2.

Exposures under continuous KCl deposition

This study focuses on the development and the analysis of a setup that better mimics the boiler environment. The motivation for this study is based on differences in the corrosion morphologies observed between field and laboratory samples. Field samples exhibit signs of severe corrosion e.g. deep grain boundaries attacks, while laboratory samples do not display similar features.

Therefore, comparisons of the corrosion morphologies between former ways of applying salt and this novel method were the first concern. For this reason, already well-known materials were used, such as 304L and Sanicro 28, instead of newly developed alloys in order to make the comparisons reliable between laboratory exposures.

Sample preparation

Sanicro 28 was provided by Sandvik, and 304L was provided by Outokumpu. The materials were received as plates and then cut into coupons with the following dimensions: 15x15x2 mm^3 with a hole of 1.5 mm diameter drilled at 2 and 7.5 mm from the edges. All samples were ground with 500 grit SiC from Struers and then polished to a mirror-like surface with 9, 3, and 1 µm diamond solutions DP-Suspension P using DP-Lubricant Yellow. As a final step, the samples were cleaned in acetone and then ethanol using an ultrasonic bath Elmasonic P from Elma.

Exposures and characteristics of the setup

The exposures under continuous KCl deposition were performed in an atmosphere of 5 % O_2 + 20 % H_2O and balanced with nitrogen. The water vapor content was established using the nafion membranes FC 125-240-5MP from Perma Pure. The flow rate used was 2.5 cm/s, and the rate was measured with a flowmeter Definer 220 from Bios. A 3-zone furnace ETF 80/12-III, from Entech Energiteknik AB equipped with a 70-mm diameter silica tube from Quarzglas Komponenten und Service QCS GmbH was used. An alumina boat with KCl(s) from VWR BDH Chemicals was placed upstream at 700 °C where the calculated vapor pressure of KCl(s) was 65.9 ppm, while the samples were placed downstream at 600 °C where the calculated vapor pressure was 3.4 ppm. Therefore, massive condensation of the salt in the sample area was expected during the exposure. The vapor pressures of KCl(g) at these two temperatures were calculated using the software FactSage 7.2 and the FTslat database. The positions of the KCl boat and the samples remained consistent for all exposures. A schematic drawing of the setup is shown in Figure 9. The duration of the exposures was set to 24 hours.
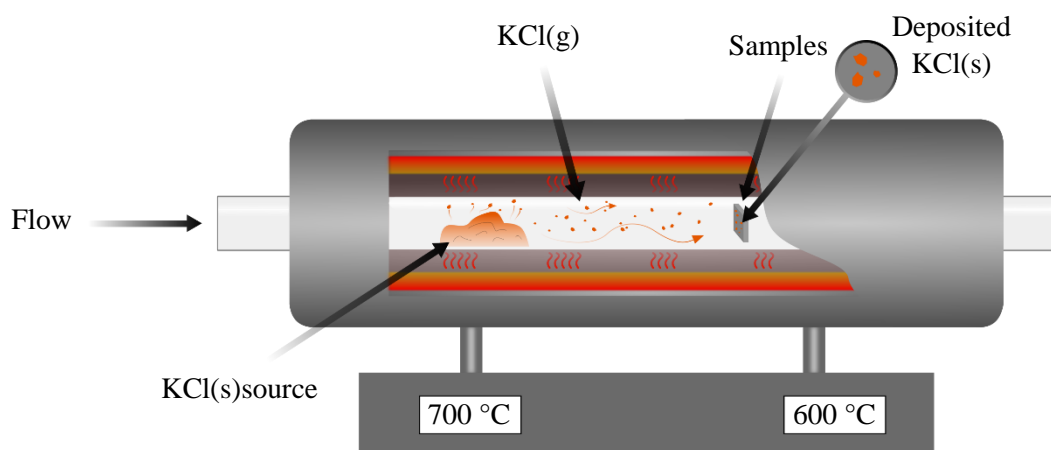
Figure 9: Schematic drawing of the experimental setup.

The temperature gradient profile in the furnace is shown in Figure 10. The gradient was measured two times in order to find the temperature variance between two experiments as the furnace was turned off in between. The measurements were performed by moving a thermocouple 20-25301000 from Pentronic forward every 1 cm from one side of the tube to the other side for a total length of 75 cm, see Figure 11. The position of the thermocouple remained consistently at the center of the furnace (co-axial). It can be seen in Figure 10 that the temperature gradient between the source of KCl(s) and the samples remained stable between two experiments, once the temperatures at each location had been reached.
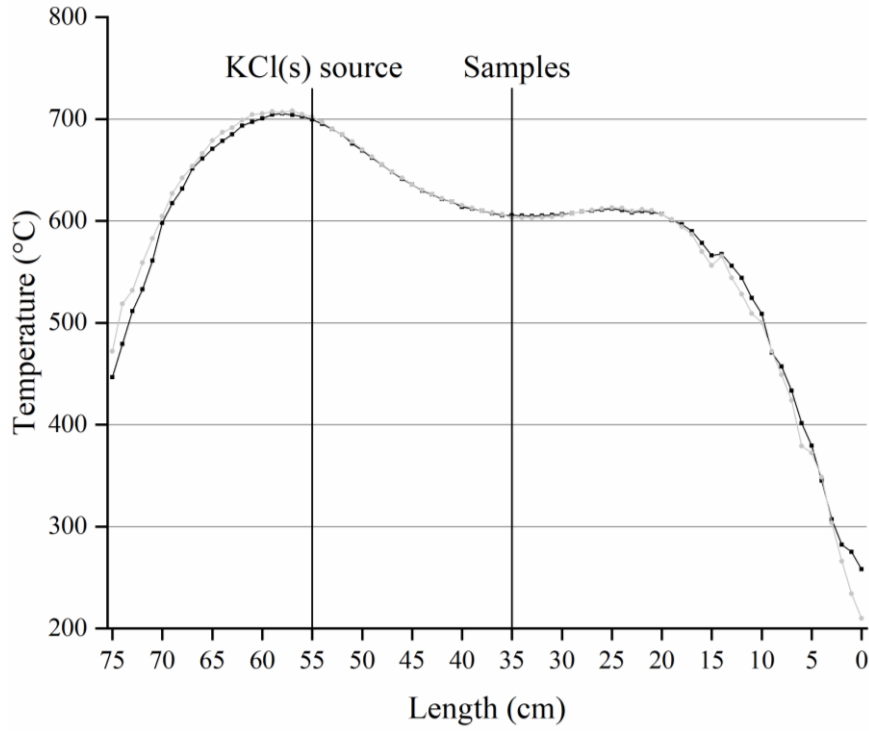
Figure 10: Temperature profile for the 3-zone heating furnace measured twice with a shutdown in between.
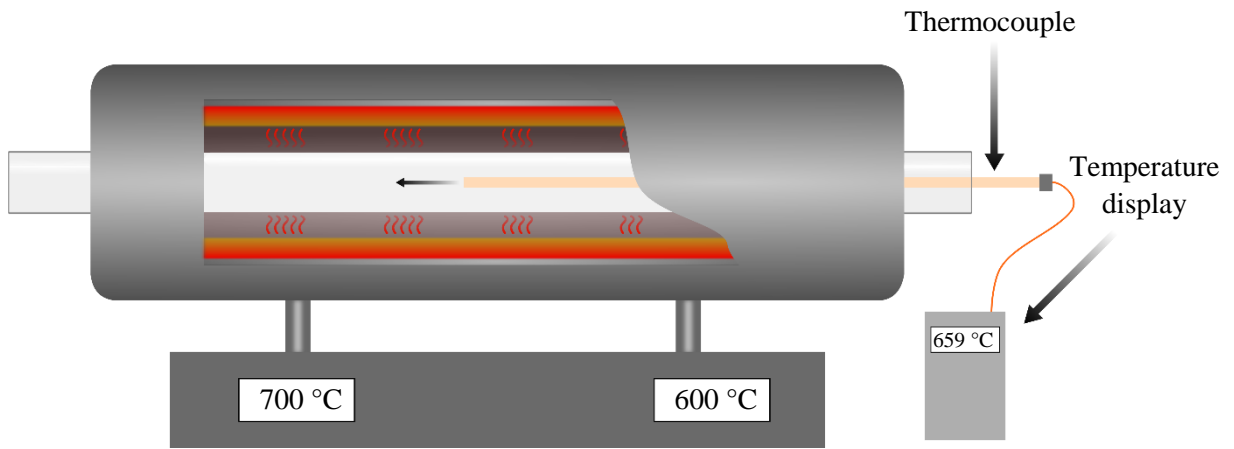
Figure 11: Schematic drawing of profile temperature measurements.

Due to the diameter of the tube and the laminar flow, a temperature spread of [-2.5 – 0] °C was considered. This uncertainty was empirically confirmed by an average of measurements performed by shifting a thermocouple 1 cm in one direction, from the center, during the measurement of the profile temperature. The highest temperature was localized at the original measurement point, which was on the rotation axis of the tube, while the measurements performed by shifting the thermocouple 1 cm in one direction exhibited a lower temperature of maximum 2.5 °C , see Figure 12. Considering the location of the samples exposed at 600 °C, such a temperature difference will induce a variation of vapor pressure of KCl(s) of ±0.4 ppm, which is negligible.

$-2.5\ °C \le \Delta T \le 0\ °C$

Thermocouple

1 cm

1 cm

Furnace

Figure 12: Schematic drawing in a profile view of the temperature uncertainty observations.

The amount of KCl deposited during the exposures is shown in Figure 13. The side positions averaged half the amount of KCl deposi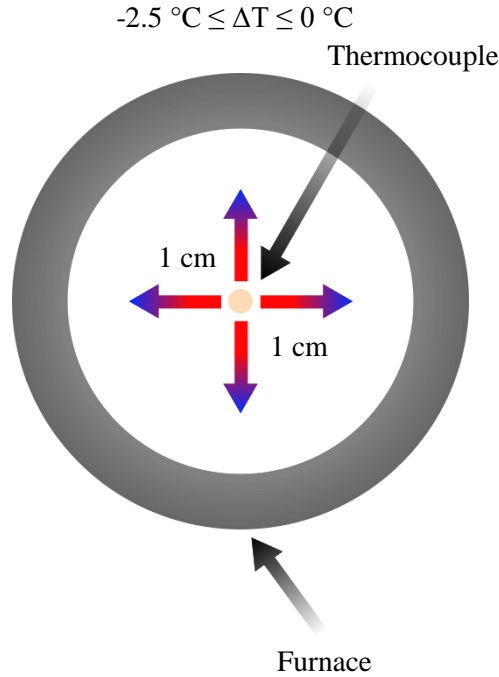ted at the middle position. The amount of KCl deposited every 24 hours for one week remained relatively consistent, with an average of 0.95 mg/cm^2 $\pm$0.31 mg/cm^2 per day at the middle position, and 0.44 mg/cm^2 $\pm$0.11 mg/cm^2 at the sides. In other words, this laboratory setup showed a reproducible KCl deposition for every experiment.

The measurements were performed using two parallel gold foils, whose mass gains of KCl were measured discontinuously every 24 hours for one week due to the deposition. Every 24 hours, the two gold foils were taken out of the furnace and weight measured, while a set of two new gold foils were placed for the next 24 hours. One of the gold foils was aligned with the axis of the tube furnace (middle position) while the second gold foil was located at one of the sides, in order to replicate the position of future samples at the same locations. The side positions were located 1.8 cm apart from the middle position, and 1.5 cm apart from the walls of the tube furnace. Figure 14 shows a schematic drawing of the positions of the samples in the furnace.
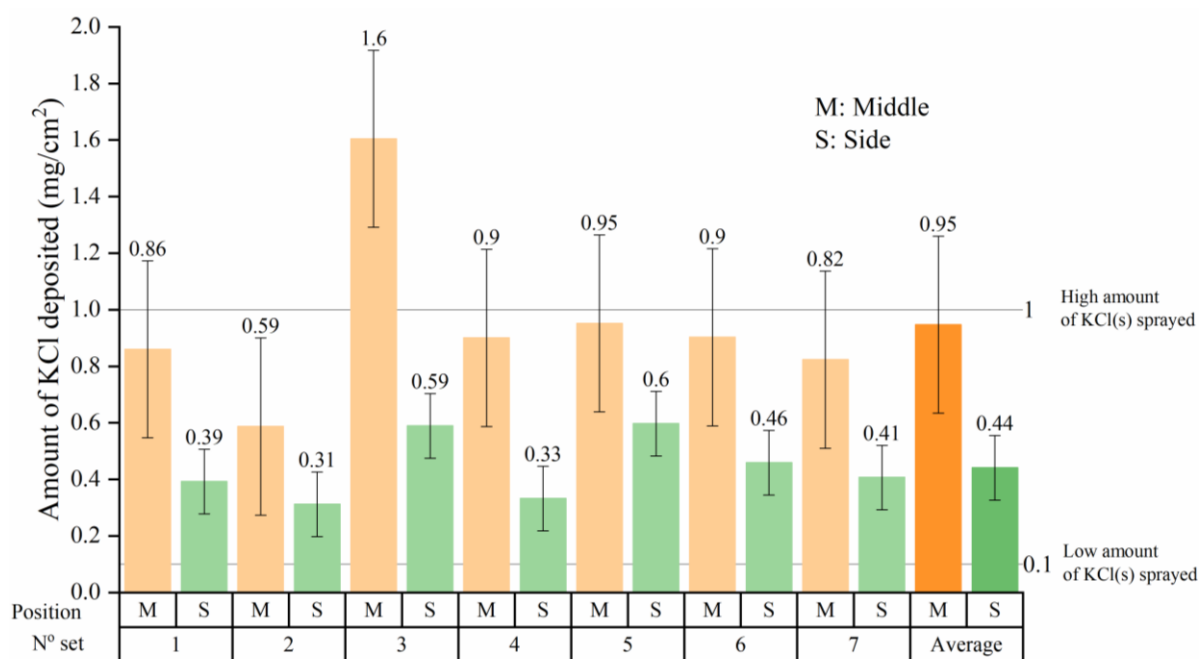
Figure 13: Amounts of KCl deposited on gold foils every 24 hours for one week at two sample positions. The reference lines represent the two different amounts of KCl(s) sprayed onto the samples prior to exposure (previous method).
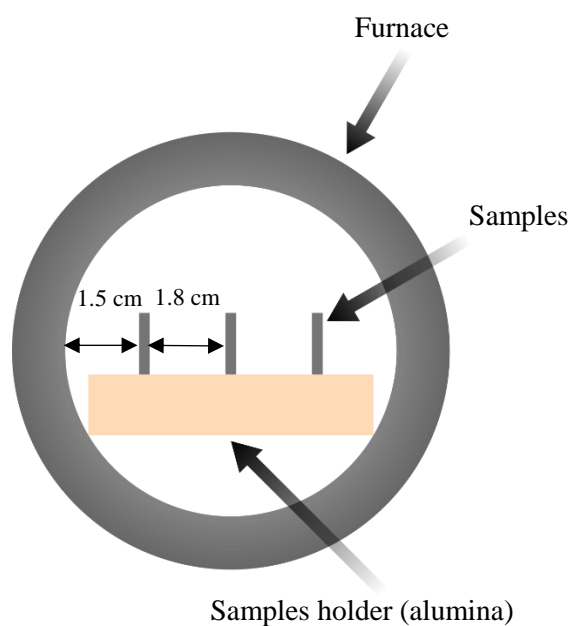

Figure 14: Schematic drawing of the sample positions within the furnace in a cross-sectional view.

7.2. Solutions for mitigation of corrosion

Mitigating the corrosion that occurs in biomass- and waste-fired boilers is crucial in order to reduce maintenance costs and preserve the highest electrical efficiency possible. Superheaters experience severe corrosion in such environments, therefore, the solutions investigated were focused on this issue.

It is possible to mitigate a corrosion attack in two ways: improving the materials or changing the surrounding environment of the materials.

7.2.1. Mitigation of corrosion by improving materials: Coatings

It is possible to improve the materials in two ways: design and development of new alloy compositions and/or the utilization of coatings. Coatings as protective layers have been widely used through the years for several applications. However, coatings often exhibit issues, such as a high level of porosity, poor adhesion to the substrate and oxide formation during thermal spraying [25, 26]. These issues result in failure of the coatings as protective layers. Moreover, in biomass and waste boilers, the presence of corrosive species such as water vapor and alkali chlorides makes the presence of defects within the coating pernicious. Consequently, it is essential to reduce the presence of defects in order to enhance the performance of the coatings. A novel spraying technique named HVAF (High Velocity Air Fuel) has been developed, and it has exhibited better adhesion between the coating and the substrate as well as low levels of porosity [27-29].

The present study focused on the corrosion behavior of three nickel-based coatings HVAF-sprayed onto a low-alloyed steel substrate. The chemical compositions of the coatings and substrate are given in Table 2.

Sample preparation

The substrate was a low-alloyed steel, 16Mo3, in the shape of rod with a diameter of 25 mm.
Prior to the thermal spraying, the 16Mo3 substrate was grit blasted with alumina particles with a size of 63 ± 10 µm. The purpose of this step was to clean the surface and make it rougher in order to achieve better adhesion of the coating.
A 16Mo3 rod of half a meter was set in a horizontal rotating mandrel during the spraying. A HVAF gun M3™ Supersonic from Uniquecoat was used to spray the coatings. The parameters used during the operation are shown in Table 3 and were determined based on preliminary coating tests in order to reduce the porosity of the coating. The rod was then cut into pieces of 5 mm thickness, and the uncoated-surfaces were also sprayed. The average thickness of the coating sprayed was approximatively 250 µm. After spraying, the samples were ground and polished down to 4000 grit with SiC paper, reaching a final thickness between 215 and 260 µm.

Table 3: Spraying parameters.

Nozzle type	3L2G
Air pressure (MPa)	0.8
Fuel 1 Pressure-Propane (MPa)	0.7
Fuel 2 Pressure-Propane (MPa)	0.7
Carrier gas Pressure-N2 (MPa)	0.4
Feed rate (g/min)	150
Pass velocity (m/min)	50
Pass spacing (mm/rev)	5
Spray distance (mm)	300
Number of passes	8

Exposures

The samples were weighed before and after exposure using a Sartorius^{TM} balance with five decimal accuracy. KCl was deposited on the samples by spraying a solution of water-ethanol (20/80) containing the salt. The samples were subsequently dried with warm air. The total amount of salt deposited on each sample was 1.0 mg/cm^2.

The samples were then exposed in a horizontal silica tube furnace in two different environments:

- 600 °C – 20% H_2O – 5% O_2 - 168h – With 1 mg/cm^2 KCl
- 600 °C – 20% H_2O – 5% O_2 - 168h – Without KCl

The water vapor content was established using the nafion membranes FC 125-240-5MP from Perma Pure, and the flow was calibrated using a flowmeter Definer 220 from Bios in order to reach 3.1 cm/s. Two samples were mounted vertically in an alumina boat parallel to the flow for every experiment.

7.2.2. Mitigation of corrosion by altering the environment of materials

In parallel with laboratory studies, it is necessary to investigate the corrosion behavior of materials in boiler environments. It is also crucial to correlate laboratory and field investigations in order to enhance the understanding of corrosion mechanisms.

In this field investigation, the study focused on the potential of a new location for superheaters in a grate-fired boiler. The new superheaters used are called Steamboost and are located over the last part of the grate. The idea is that corrosive species are released over the first part of the grate, which makes the flue gas less corrosive in the last part of the grate, where the Steamboost superheater is located. This position was suggested using Computational Fluid Dynamics (CFD) calculations [59].

The field exposures were performed in an AffaldPlus Combined Heat and Power (CHP) plant located in Næstved, Denmark. This is a 27 MW grate-waste-fired boiler. Its nominal capacity is 8t/h. The combustion system was based on the latest state-of-the art technology from Babcock & Wilcox Vølund, a combination of the technologies from the Vølund systems, CFD calculations, and combustion technologies. A schematic drawing of the plant that shows the location of the performed tests is presented in Figure 15.
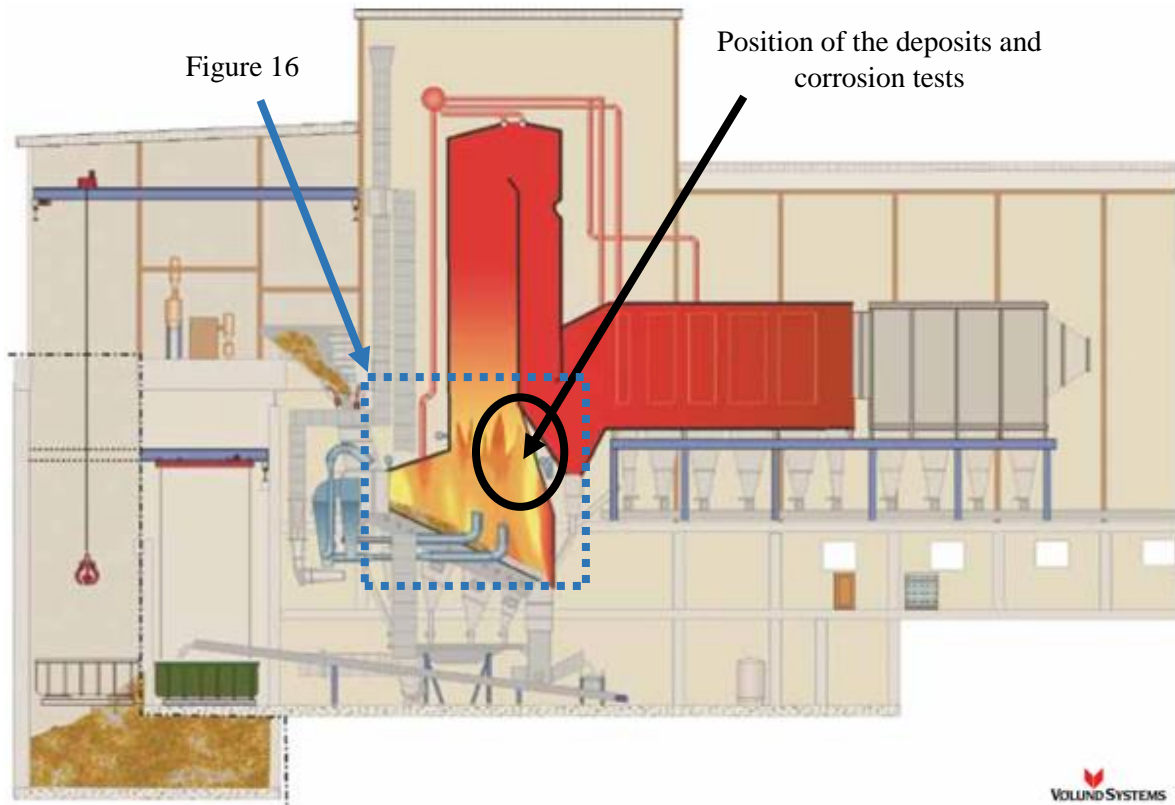
Figure 15: Schematic drawing of the combined Heat and Power plant AffaldPlus in Denmark [59, 60].

The investigation consists of two parts:

- Deposit test: Different ways of running the boiler were tested in order to study the influence on the deposit composition at the Steamboost position using an air-cooled probe.
- Corrosion test: A corrosion probe (not investigated in the present thesis) as well as a fixed installation with various material grades connected to the main steam of the plant were installed at the Steamboost position.

Figure 16: Schematic drawing of the principle of the Steamboost.

Figure 16 presents a schematic drawing of the principle of the Steamboost. Corrosive species are released over the first part of the grate, which results, in a less corrosive environment over the last part of the grate.

Deposit test

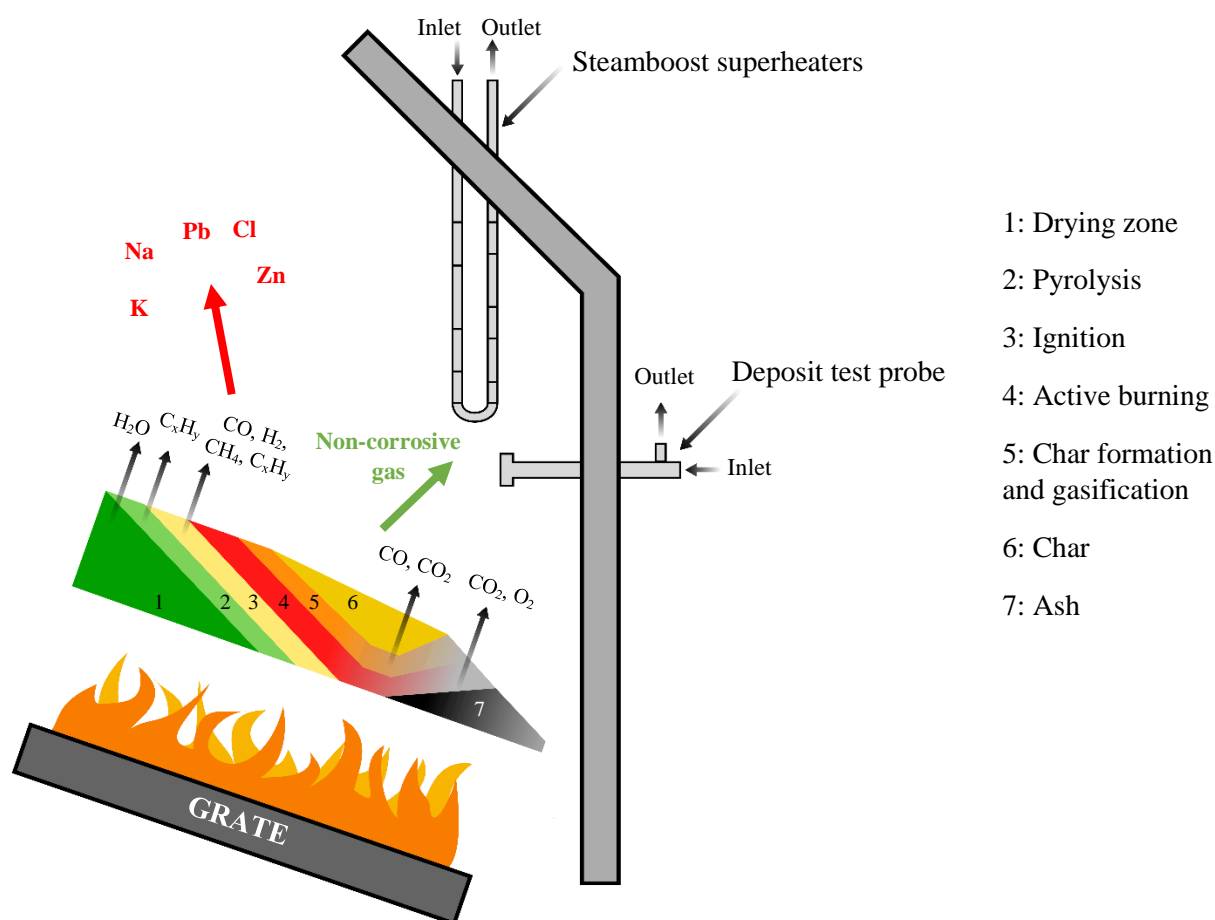The purpose of the deposit test was to run the boiler with different air flow settings to study the influence on the deposits at the Steamboost position. The duration of each exposure was 2 hours per setting for a total of 29 settings tested. Every setting had a different distribution and amount of air combined with grate operation. According to the CFD calculations (Figure 16), the corrosive species were released over the first part of the grate so that the corrosiveness of the flue gas released from the last part of the grate was lower. The air-cooled probe inserted carried nine samples, three per location on the probe, see Figure 17. Two temperatures were investigated: 525 °C and 700 °C.

The exposed samples were rings of high-alloyed stainless steel Sanicro 28, to avoid the influence of corrosion products during the deposit tests. The samples were then stored in desiccators with a drying agent, Sicapent® from Sigma-Aldrich.
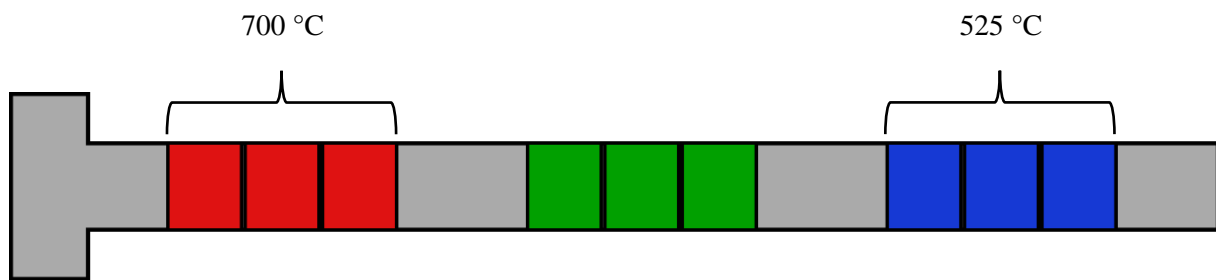
Figure 17: Schematic drawing of the probe carrying the nine samples for the deposit tests (only two temperatures investigated)

<u>Corrosion test</u>

The superheater was composed of three loops of several materials welded together and that were exposed for 8000 hours. Each loop carried the exact same materials, the difference was the steam temperature, which was increased from the first loop to the last loop. The Steamboost superheaters were connected to the main steam of the plant which had an inlet temperature of 340 °C at the entrance of the installation, and an outlet temperature of 470 °C at the exit. This resulted in a metal temperature of approximatively 525 °C.

8. Analytical techniques

Several different analytical techniques were used to investigate the exposed samples from the field and the laboratory, and these are described and explained in this section. It is necessary to use a wide range of techniques in order to gain full understanding of the phenomena.

8.1. X-Ray Diffraction – XRD

This technique is used to determine the crystalline phases present in the sample. It relies on the principle of coherent elastic X-ray scattering. A beam of incident monochromatic X-rays is generated and orientated towards the sample where the beam interacts with the crystal structure of the sample. The X-rays will then scatter in several directions but will diffract in some specific directions due to the periodicity of the crystal. The scattered X-rays can either have destructive or constructive interferences. Constructive interferences are produced when the conditions of Bragg's law are satisfied, resulting in the diffraction of the incident beam. This law relates the wavelength of electromagnetic radiation to the diffraction angle and the lattice spacing in crystalline samples via the following equation [61, 62]:

$$n\lambda = 2d \sin(\theta) \tag{19}$$

where d is the spacing between the diffracting planes, λ is the wavelength of the incident X-ray beam, θ is the incident angle and n is an integer. A physical representation of the phenomenon is shown in Figure 18:
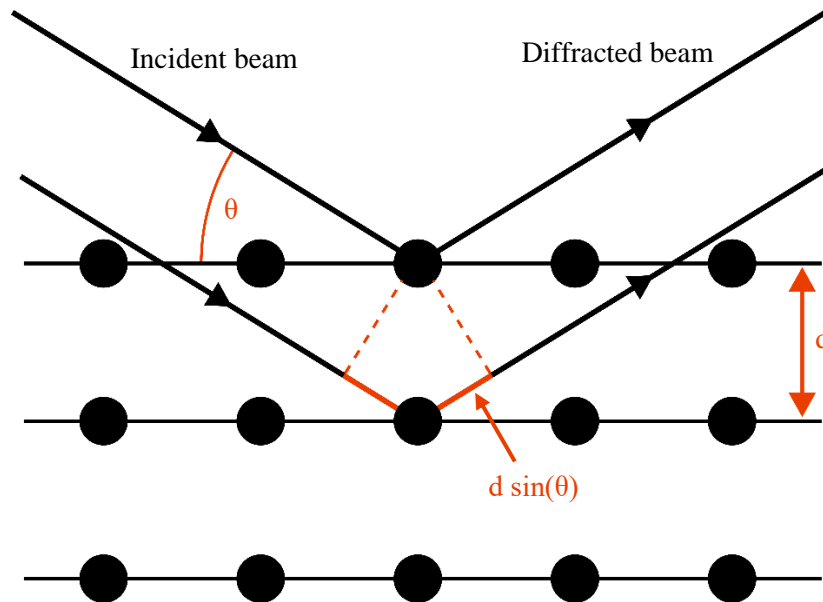

Figure 18: Representation of Bragg's law.

As the wavelength of the monochromatic beam of X-rays is fixed, the incident angle θ is the parameter that will vary during measurements. A standard setup for XRD consists of one source of X-rays, a sample location, and a detector, which is called Bragg-Brentano geometry (Figure 19). Moreover, different

scanning modes are available and, these allow different purposes, such as a grazing incidence setup to obtain information mostly thin films by choosing a low angle of incidence for the X-rays.

An XRD analysis consists of measuring the intensity of the diffracted beam as a function of 2θ, resulting in diagrams called diffraction patterns. The patterns are compared with a database in order to identify the different phases.
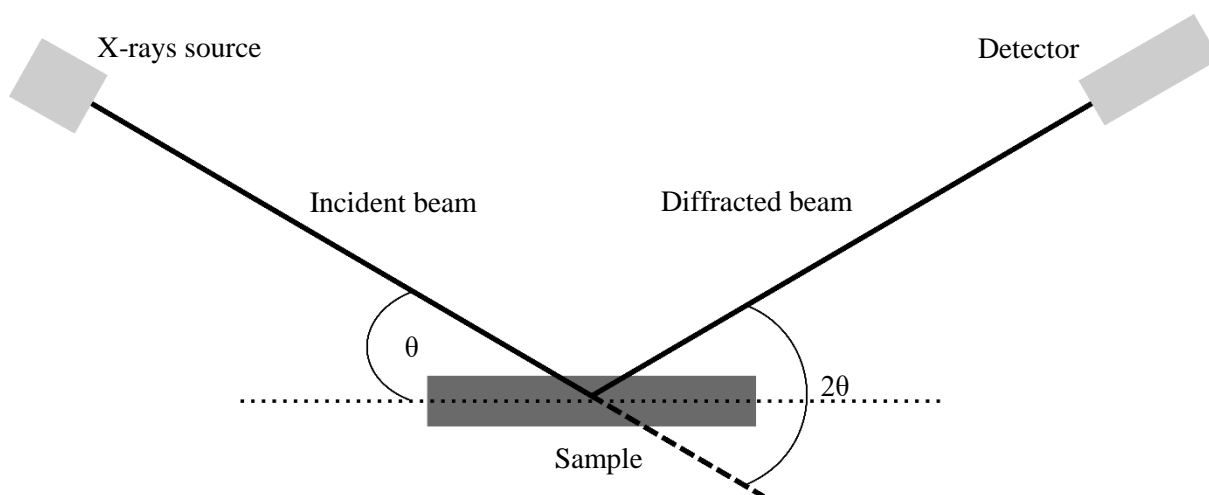
Figure 19: Schematic representation of a diffractometer with Bragg-Brentano geometry.

The diffractometer used for the XRD characterization was a Siemens D5000 with a Göbel mirror. The wavelength used was a specific Cu K_α ($\lambda = 1.54178$ Å) and was generated by a copper anode X-ray tube. The incident angle was 7.5°, and the measuring range was [10° - 60°].

8.2. Scanning Electron Microscope (SEM)

Microscopy is a powerful technique of characterization for corrosion science that provides information on grain size, morphology, or chemical compositions. This technique relies on the interaction between an incident beam of electrons and the atoms of the sample. Several types of interactions can occur, and these interactions produce different types of products of interaction, such as Auger electrons or backscattered electrons, depending on the depth reached by the incident beam in the sample, see Figure 20. The depth depends on the accelerating voltage of the electrons; the higher it is, the deeper the electrons have reached.

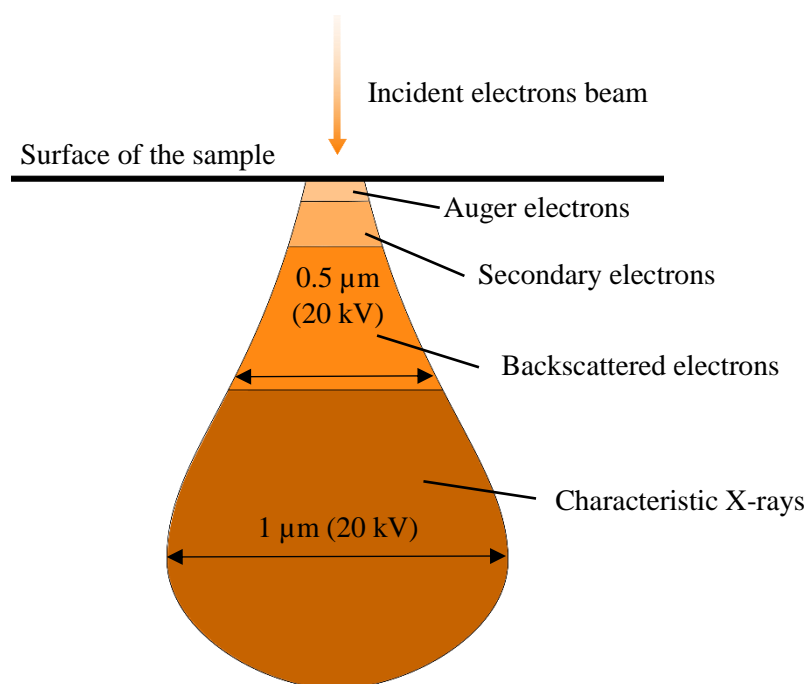*Figure 20: Schematic illustration of the interaction volume and the products of interaction.*

Secondary electrons

This type of electron is produced via inelastic scattering interactions between the incident electron and an electron of the K shell of the atom. The incident electron ejects the electron located at the K shell of the atom, producing a so-called "secondary electron" with a lower energy (<50 eV). These electrons are mainly located near the surface, and, thus, they provide information about the surface, such as topography and morphology [63].

Backscattered electrons

This type of electron comes from elastic scattering interactions between the incident electron and the atom. As heavy elements have a higher atomic number, the number of electrons reflected (backscattered) is larger than with light elements. Heavy elements therefore appear brighter in the image. Backscattered electrons are used to detect the different phases caused by the differences in chemical composition. An accelerating voltage of 20 kV was used when performing the chemical analysis. This resulted in a resolution of 0.5 µm (see Figure 20) [63].

Characteristic X-rays for Energy Dispersive X-ray Spectroscopy (EDX)

Another possible interaction is the excitation of an electron from the inner shell of an atom, resulting in its ejection and the creation of an electron hole. The atom is subsequently in an excited state, which is resolved when an electron from the outer shell fills the vacant place. The difference in energy between the outer shell (higher energy) and the inner shell produces an X-ray. As the energy difference between

the two shells produces characteristic X-rays, it is possible to perform map distribution and estimate the abundance of elements in the area of interest [63].

The SEM used in this study was a FEI Quanta 200 equipped with an Oxford Instruments X-Max^N 80EDX detector. The accelerating voltage used for imaging was 10 kV (~2-3 nm resolution), and 20 kV was used for EDX analysis (~1 µm resolution).

8.3. Broad Ion Beam (BIB)

A BIB was used to prepare cross sections of the exposed samples. BIB provides high quality cross sections using a mild milling with argon ions. The main asset of this tool is that it provides the same quality of milling as the Focus Ion Beam (FIB) technique, but with a larger area of interest (2-3 mm). Mechanical stresses, degradation of oxide scales, and clogging of pores/voids from the mechanical polishing technique are avoided when the BIB technique is used. It relies on three individual ion sources that are focused on an area. The samples are prepared by gluing a piece of silicon wafer on top of the sample to protect the surface, then they are preliminarily cut using a low speed saw in order to expose a cross-sectional area of interest. The sample is then attached to the sample holder of the BIB and adjusted to set the desired section that is to be milled. This is achieved by setting the length of the sample protruding from a mask covering and protecting the rest of the sample. The ion beams perpendicularly hit the mask and the sample, see Figure 21.
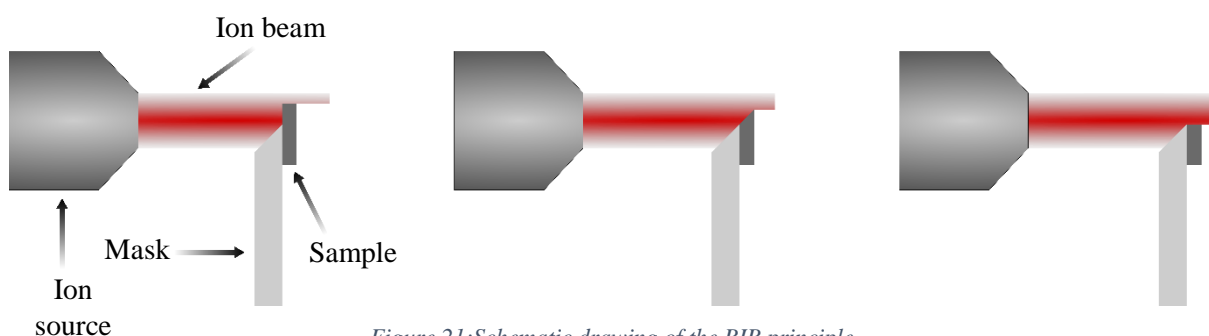
Figure 21:Schematic drawing of the BIB principle.

The BIB used was a Leica TIC 3X and the sessions were operated at 6.5 kV for a duration of 12 hours.

8.4. Ion Chromatography (IC)

The Ion Chromatography technique allows the quantification of water-soluble ions, such as Cl^- or SO_4^{2-}. It was therefore used during field investigations to investigate the influence of different boiler settings on the amount of these ions found in the deposits.

The exposed samples were first leached in a known volume of MilliQ water to dissolve the ions. The obtained solution was then pumped with an eluent through a column containing a stationary phase. This stationary phase sorts the different ions present in the solution. The sorting is based on the charge and size of the ions. The ions that exhibit less affinity with the stationary phase are less retained in the column, which results in a fast elution time. While the ions that exhibit more affinity with the stationary

phase are more retained in the column and have a slower elution time. A detector at the end of the column records the conductivity of the total solution as a function of time and compares it to a standard solution with a known concentration.

This technique analyzes cations and anions separately, depending on the column used. Only anions are considered in this study. A schematic representation of the technique is shown in Figure 22.
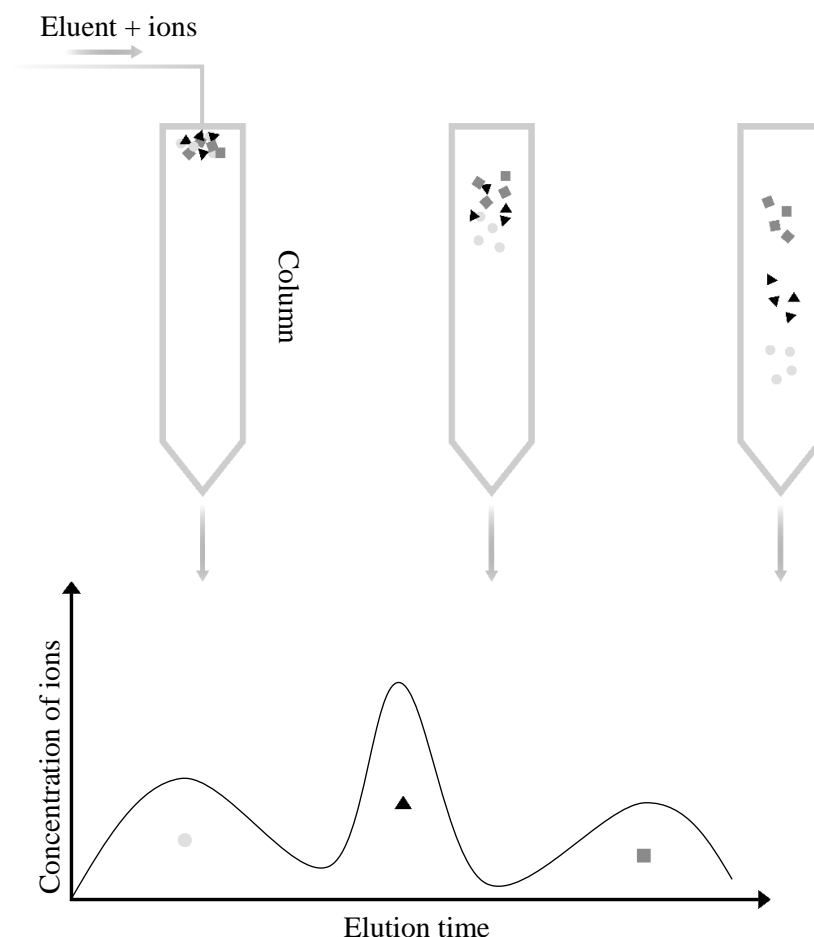
Figure 22: Schematic representation of the ion chromatography technique (top). Signal of the detected ions as a function of time (bottom).

The equipment used was a Dionex ICS-90 Ion Chromatography (IC) system with an IonPac AS4A-SC analytic column. The eluent used was a 1.8 mM sodium carbonate/1.7 mM sodium bicarbonate solution, and the flow rate was 2 mL/min. The samples were leached in 10 mL Milli-Q water and placed in an ultrasonic bath for 10 minutes

8.5. Ultrasonic measurements

Material loss measurements were performed in order to characterize the corrosion rate of samples from field exposures. The thickness of each sample was measured at eight different points of the ring, before and after the exposure, using an Olympus 27MG ultrasonic thickness gage with a 0.01 mm resolution.

9. Results and discussions

The corrosion of critical parts in biomass- and waste-fired has been demonstrated and studied often [10-21, 53-56, 64, 65]. In order to find suitable solutions, it is necessary to understand the different processes involved in corrosion in such environments and temperatures. Consequently, it is essential to investigate both laboratory and field exposed samples. Laboratory investigations are crucial in order to understand the importance and influence of parameters, while field investigations are relevant in order to compare the laboratory results with observations in boilers.

9.1. Investigation of accelerated corrosion caused by continuous KCl addition

Laboratory investigations are essential to understanding of the corrosion mechanisms. A boiler environment is complex, and it is necessary to isolate and understand the influence of the different major parameters. A considerable difference in corrosion rates between field [14, 66] and laboratory [24, 67, 68] exposed samples has been observed. Field samples encounter a considerably accelerated corrosion attack compared to laboratory exposed samples. A novel laboratory setup was therefore developed to better mimic the boiler environment.

Exposures under continuous KCl deposition

Several investigations of the corrosive effect of KCl at high temperatures were performed earlier with either a fixed amount of KCl(s) deposited on samples before exposure [24] or with a layer of KCl(s) covering a sample [15, 21]. However, this rather stationary technique of investigating the effect of salt does not simulate the deposit formation (see Section 9.3.2) that occurs in boilers and is mostly relevant for studies on the initiation of corrosion. When focusing on the propagation of a corrosion attack, the supply of KCl may decrease or even become negligible. In addition, a corrosion attack and deposit formations occur simultaneously, probably affecting each other. Therefore, a laboratory setup with continuous deposition of KCl(s) on the samples was developed to better study the propagation of a corrosion attack.

A characteristic of this setup is the presence of a gradient of the salt deposition on a sample's surface. Figure 23 is a representative photograph of exposed samples directly after outtake from the furnace. The distribution of KCl(s) on the sample surfaces is heterogeneous. This leads to the need to use the BIB technique, as larger areas of interest must be analyzed. More KCl(s) deposition was also observed at the top than at the bottom of the samples, which shows that a gradient in the amount of KCl(s) was present between these two positions on the samples. Moreover, the deposition of salt was also heterogeneous between the samples. The middle samples exhibited substantial deposition while the deposition was lower in the side samples. As a consequence, two areas of interest were defined based on apparent KCl(s)

deposition and on different levels of suspected corrosiveness; the top part of a middle sample was suspected to be the most corroded area of an exposure (labelled "high amount of KCl"), while the bottom part of a side sample was suspected to be the least corroded area (labelled "low amount of KCl"). Several exposures using the same experimental parameters were performed to investigate the reproducibility of the exposure setup.

It was found that replicating the deposition of KCl(s) between each exposure is possible and reliable based on the measurements of KCl(s) deposition and the reproducible morphology of the deposition observed on the samples.
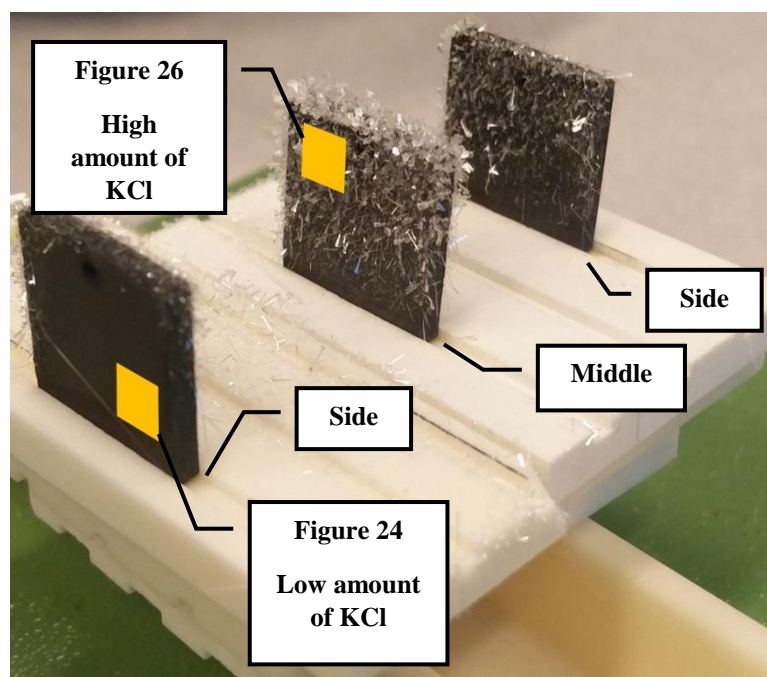

Figure 23:Photograph of 304L samples after an exposure for 24 hours at 600 °C in 5% O_2 + 20% H_2O under continuous KCl deposition.

9.1.1. Stainless steel 304L

Characterization of the "low amount of KCl" area of 304L

Optical inspection of this area revealed no substantial deposition of KCl(s). The lack of visually observable KCl(s) was confirmed with SEM/EDX analysis where the presence of salt on the surface was negligible (Figure 24a). However, despite the lack of KCl(s) agglomerations on the surface, the corrosion attack was severe already after a 24-hours exposure.

The surface is completely covered by iron oxide. The cross-sectional view in Figure 24b confirms the plan-view observations; the oxide layer consisted of an outward growing oxide Fe_2O_3 on top and an inward growing spinel oxide $(Fe,Cr,Ni)_3O_4$ below.

The thickness of the oxide scale varied between 9 and 15 µm with no visible signs of a steel grain boundaries attack. The morphology of this corrosion attack is similar 304L samples exposed with 0.1 mg/cm^2 of KCl(s) applied *ex-situ* prior to exposure (Figure 25).
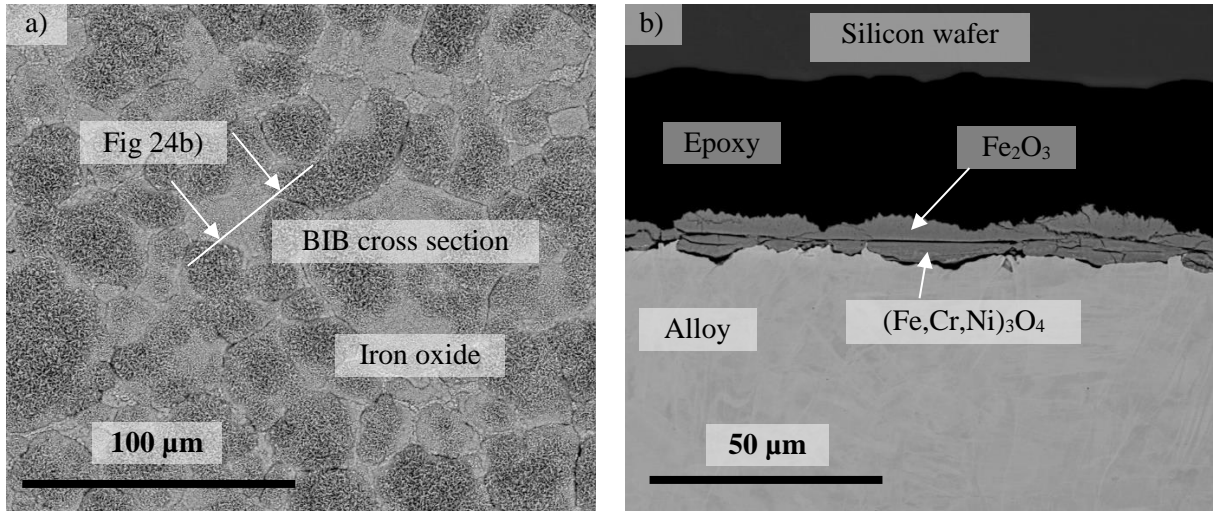
Figure 24:SEM image using BSE of a) the plan view of a "low amount of KCl"-area of a 304L sample after 24 hours in 5% O_2 + 20% H_2O exposure under continuous KCl deposition at 600 °C and b) a cross-sectional view.
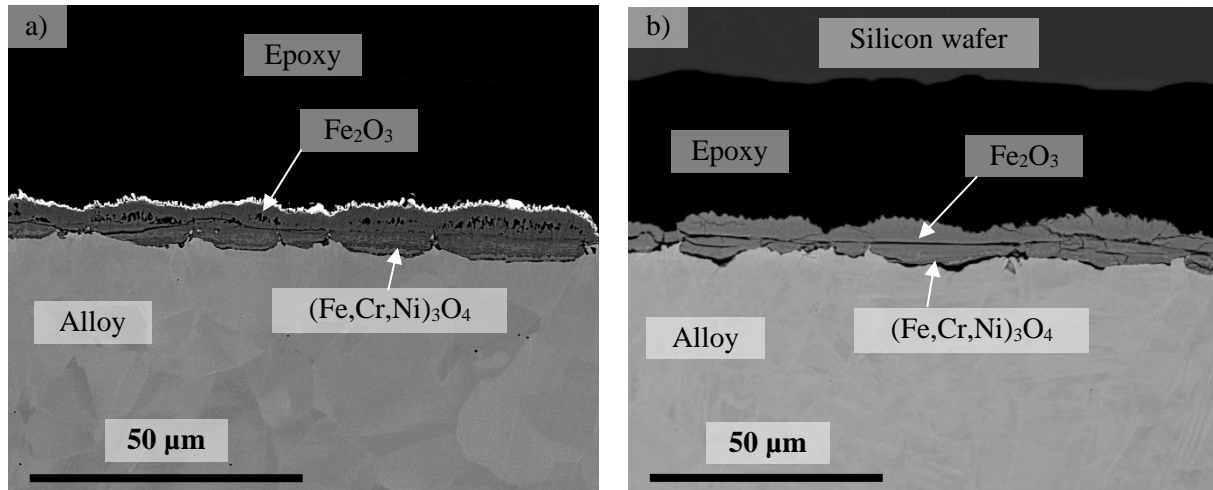

Figure 25: SEM image using BSE of a cross section of a) 304L sample exposed to 0.1 mg/cm² KCl(s) applied prior to exposure after 24 hours at 600 °C in 5% O_2 + 40% H_2O [24] b) 304L sample exposed to KCl(s) under continuous KCl deposition after 24 hours at 600 °C in 5% O_2 + 20% H_2O.

The corrosion morphology of the samples with KCl(s) applied prior to exposure was consistent with the features previously observed on the samples exposed under continuous KCl deposition: an outward growing Fe_2O_3 layer on top and an inward growing spinel type layer $(Fe,Cr,Ni)_3O_4$ below. Moreover, the samples with salt applied prior to exposure exhibited a total oxide thickness between 7 and 9 µm (9 and 15 µm under continuous KCl deposition with no visible sign of a steel grain boundaries attack. Thus, the areas designated as "low amount of KCl"-area exhibited corrosion features similar to the corresponding exposures where salt was applied prior to exposure.

Characterization of the "high amount of KCl"-area of 304L

Large agglomerations of deposited KCl(s) crystals were labelled as high amount of KCl areas. The largest crystals were removed gently using an air duster to make the sample preparation more convenient.

Figure 26 shows the plan view of a) a surface covered with KCl(s) b), a spalled area, and c) a cross-sectional view of the area marked in Figure 26a.
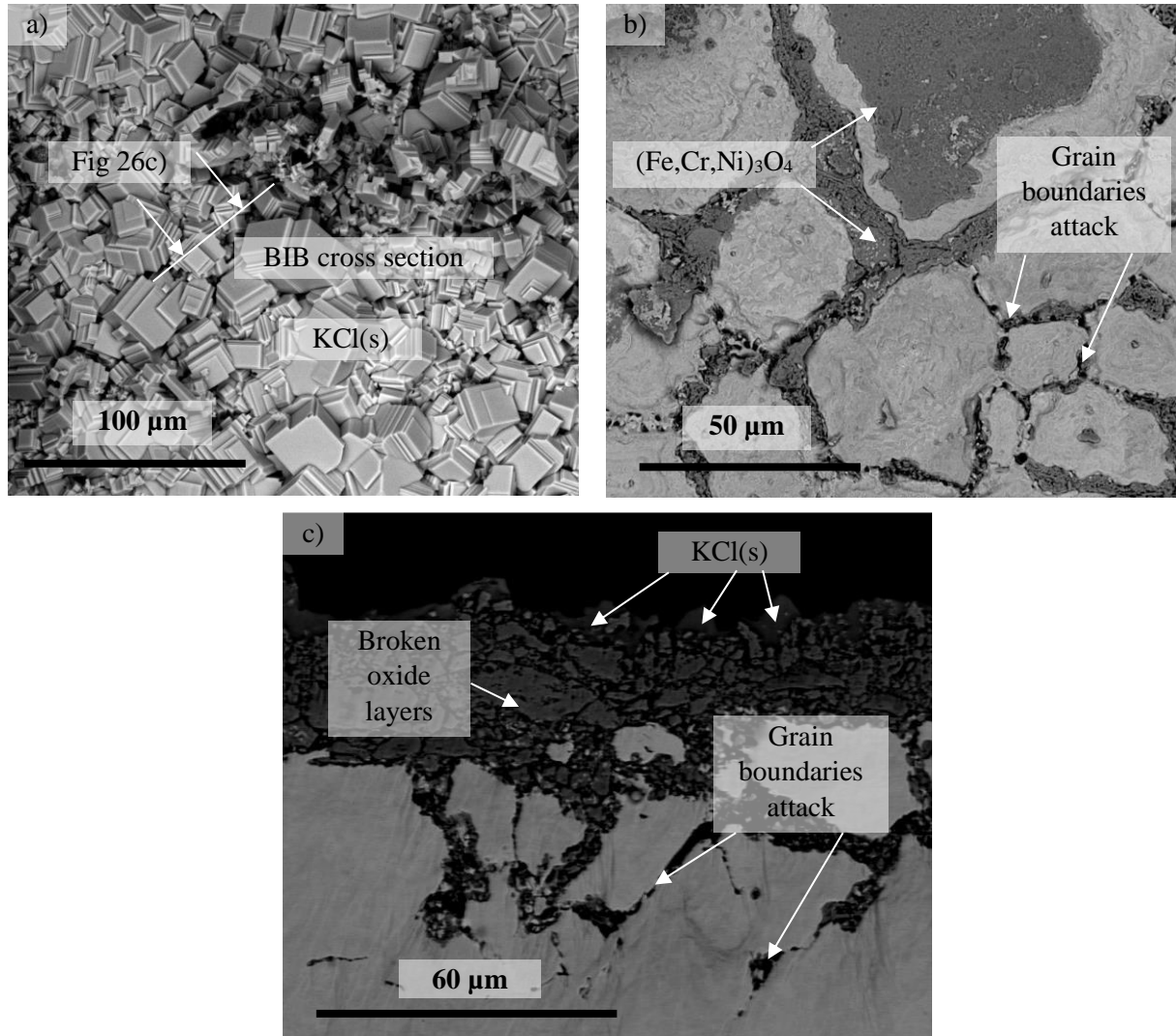

Figure 26: SEM image using BSE for a) the plan view, b) a spalled area and c) a cross sectional view of a "high amount of KCl"-area after 24 hours at 600 °C in 5% O_2 + 20% H_2O.

Figure 26a shows that the sample's surface was totally covered by KCl(s) crystals. An area where part of the corrosion product layer as well as KCl(s) crystals spalled is shown in Figure 26b. A steel grain boundaries attack can be clearly seen in the plan view, and this was later on confirmed with the cross-sectional view in Figure 26c. These grain boundaries attacks can reach between 30 and 50 µm depth. This attack seems to be correlated to the amount of KCl(s) present on the surface, which has been observed in a previous study [24]. In the publication mentioned, 304L was exposed after an amount of KCl(s) of 0.1 mg/cm^2 or 1.0 mg/cm^2 was applied onto the sample prior to exposure. The exposures were also performed with and without the presence of SO_2(g). The results showed that the grain boundaries attack increased with a higher amount of available chlorine. Either by increasing the amount of KCl(s) from 0.1 mg/cm^2 to 1.0 mg/cm^2 or by introducing SO_2(g) to the surrounding environment causing the release of HCl(g) via sulphation of KCl(s) as follows:

41

$$2KCl(s) + SO_2(g) + H_2O(g) + 1/2O_2(g) \rightleftharpoons K_2SO_4(s) + 2HCl(g) \tag{20}$$
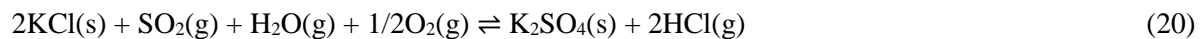
The maximum depth reached by the grain boundaries attacks in the previous study was approximatively 10 µm. Thus, this novel approach of depositing KCl(s) continuously reproduces a more corrosive environment than the previous method used. However, when compared to samples exposed in a waste-fired boiler for 24 hours, the depth of the grain boundaries attacks reached approximatively 140 µm (Figure 27).
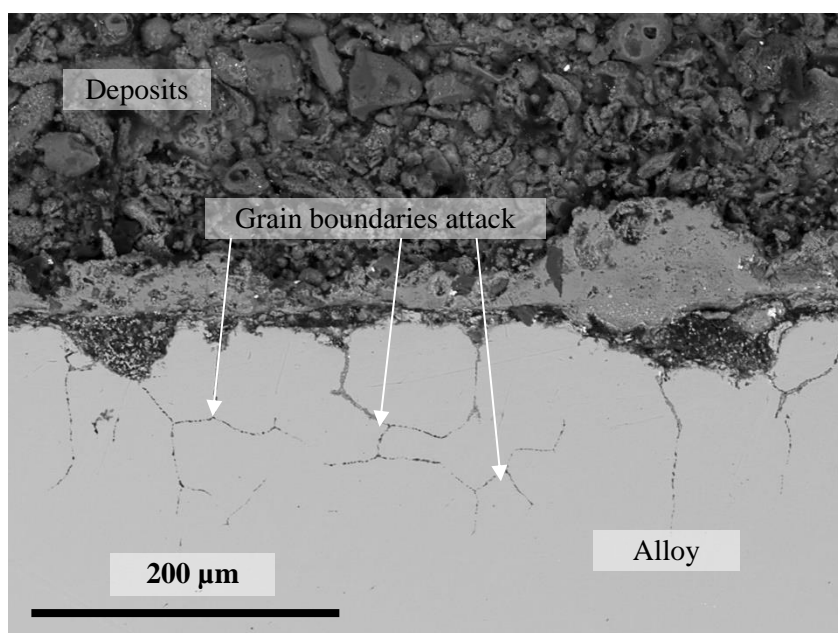

Figure 27: SEM image using BSE of the cross section of a 304L sample exposed for 24 hours at 600 °C in a CFB boiler burning a waste mix (SRF+bark) [14].

In order to investigate the accelerated corrosion attack observed at the steel grain boundaries, a detailed EDX map of Figure 26c was performed and is shown in Figure 28. The corrosion products detected within the grain boundaries consisted of an oxide with the following composition: O (53-56%), Cr (18-21%), Fe (15-19%) and Ni (7-9%) in at-%. Voids and holes were observed along the grain boundaries. Small amounts of chlorine were also detected within the grain boundaries. However, more study is required to understand the exact role of chlorine in the corrosion process. These features have also been found in other laboratory studies, however, not equally severe as the present study [24, 67, 68].

This novel laboratory exposure setup with continuous KCl deposition has shown that the corrosion morphology of field exposed samples can be mimicked more closely, in a well-controlled manner. Thus, the causes behind, e.g. grain boundaries attacks, can be investigated in a better way.
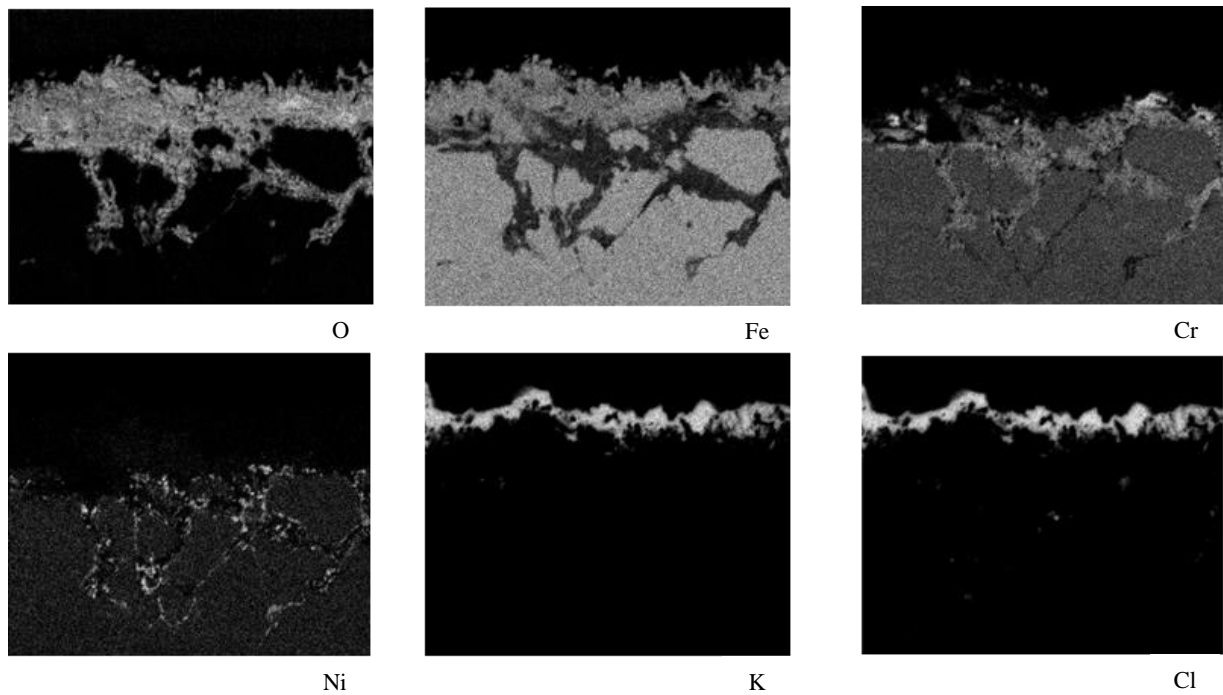
Figure 28: EDX map of the cross-sectional view in Fig.26c

9.1.2. <u>High-alloyed stainless steel Sanicro 28</u>

<u>Characterization of the "low amount of KCl"-area of Sanicro 28</u>

Sanicro 28 showed no deposition of KCl(s) with visual inspection. The lack of KCl(s) visually observable was confirmed with SEM/EDX analysis where the presence of KCl(s) was also negligible, see Figure 29. The surface consisted of both thin and thick iron oxides that covered it. Small agglomerates of potassium chromates ($K_2CrO_4(s)$) were observed on top of the oxide scale. The presence of $K_2CrO_4(s)$ was pronounced at the grain boundaries and in the middle of the grains. The "low amount of KCl"-area exhibited similar features to a sample with 0.1 mg/cm^2 of KCl deposited onto the surface prior to exposure, see Figure 30 [69].

Figure 29: SEM image using BSE of the plan view of a "low amount of KCl"-area from a Sanicro 28 sample after 24-hour exposure at 600 °C in 5% O_2 + 20% H_2O under continuous KCl deposition.

Figure 30: SEM image using SE of the plan view of a Sanicro 28 sample after 24-hour exposure at 600 °C in 5% O_2 + 40% H_2O with 0.1 mg/cm^2 KCl(s) [69].
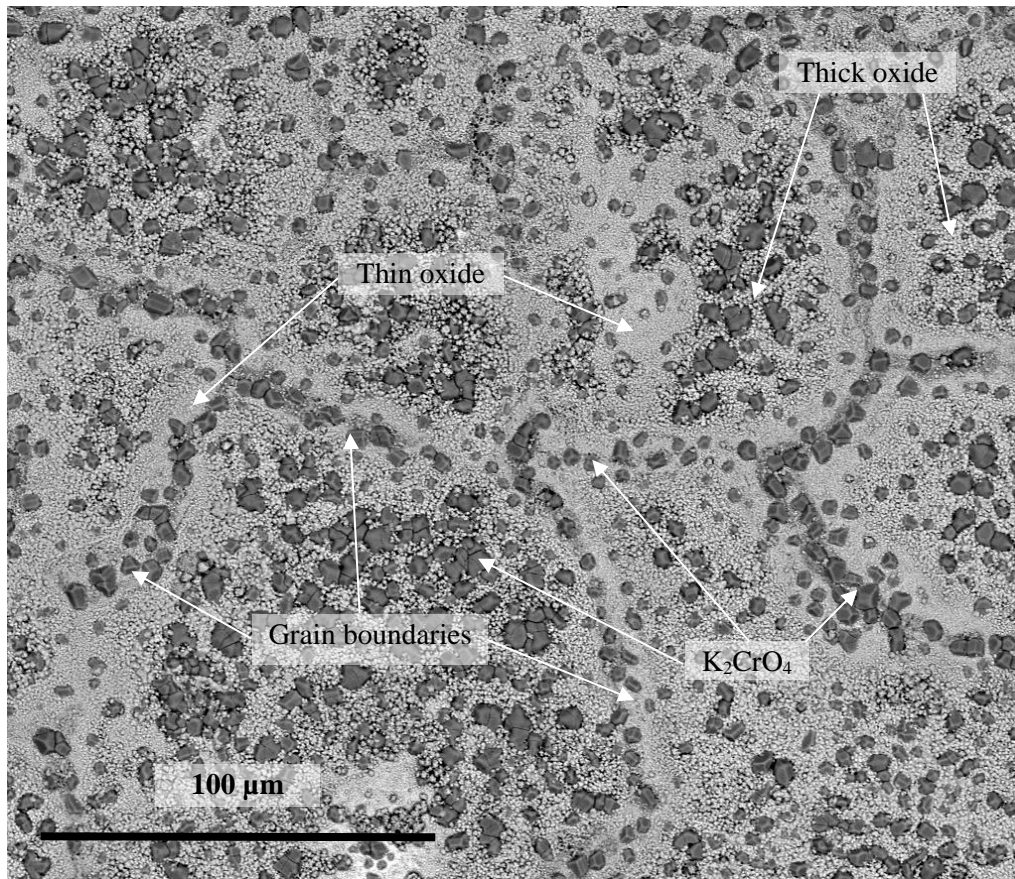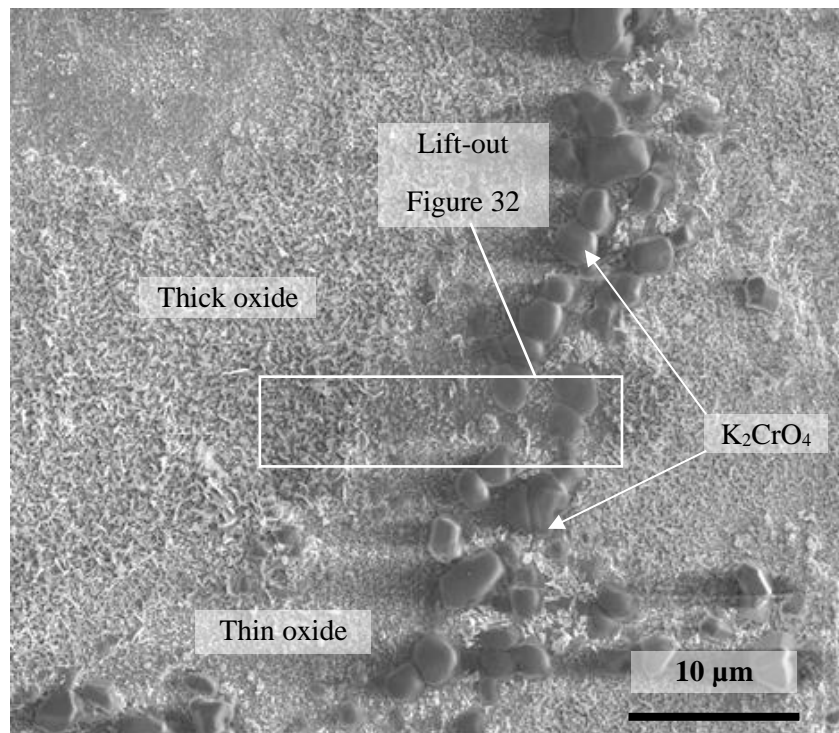
Despite the lack of detection of KCl(s) in the "low amount of KCl"-area on Sanicro 28, breakaway oxidation did occur. However, the corrosion attack was not as pronounced as for 304L. The presence of a thin oxide between 750 and 820 nm and potassium chromates were observed in Sanicro 28, see Figure 31. This means that breakaway oxidation was triggered in the "low amount of KCl"-area as no chromium-rich layer (primary protection) was observed on the surface. However, the thin oxide on the surface is a sign of good secondary protection. Even so, the initiation of a grain boundaries attack was also observed. The maximum depth of the attack was approximatively 2.2 µm.

Figure 31: SEM image using BSE of the cross section of a "low amount of KCl"-area from a Sanicro 28 sample after 24-hour exposure at 600 °C in 5% O_2 + 20% H_2O under continuous KCl deposition.

Grain boundaries attack was also observed in previous studies investigating a Sanicro 28 sample with 0.1 mg/cm^2 of KCl applied prior to exposure (see Figure 32). The depth of the attack was similar in both exposures, which reached 2-3 µm.
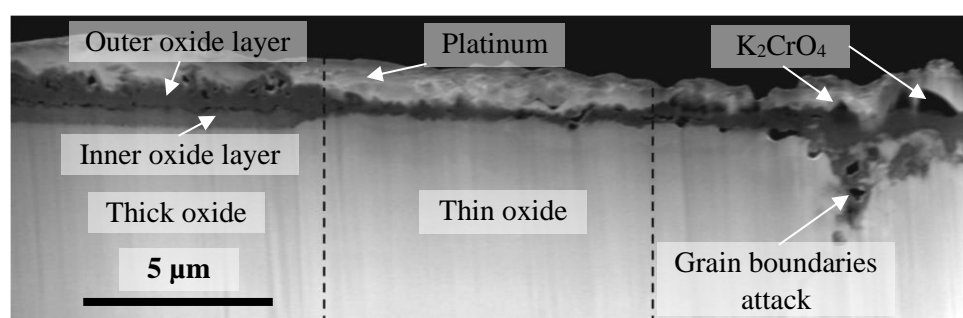
Figure 32: SEM image using SE of the cross section a Sanicro 28 sample (Figure 30) after 24-hour exposure at 600 °C in 5% O_2 + 40% H_2O with 0.1 mg/cm^2 KCl(s) [69].

In Figure 33, the oxide that formed on Sanicro 28 in the "low amount of KCl"-area after breakaway is shown with a higher magnification. Despite the loss of the primary protection, the oxide scale is rather thin. It appears that this thin oxide is actually composed of two oxide layers:

- An outward-growing oxide layer (brighter): a thickness varying between 400 and 600 nm, and a composition of Cr (~20%), Fe (~44%) and Ni (~36%) in at%.
- An inward-growing oxide layer (darker): a thickness varying between 300 and 460 nm, and a composition of Cr (~40%), Fe (~32%) and Ni (~28%) in at%.

The elemental compositions of the two thin oxides indicate that they may be spinel oxides $(Fe,Cr,Ni)_3O_4$. However, the resolution was too low at 20 kV with the current magnification (Figure 33), and it was not possible to accurately reach a conclusion on the elemental compositions of these thin oxides using EDX. Neither XRD analysis revealed signs of spinel oxides. Thus, it is necessary to perform more advanced analyses to identify these two thin oxide layers.
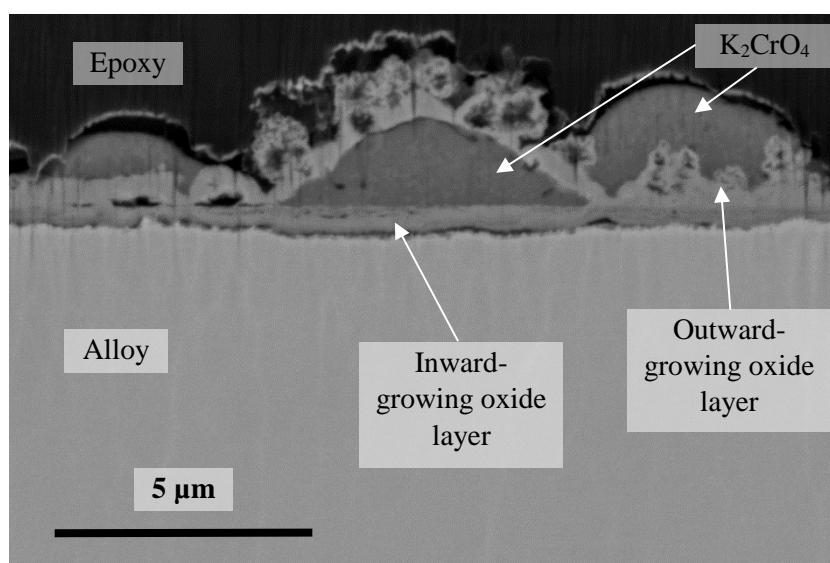
Figure 33: SEM image with higher magnification using BSE of the plan view of a "low amount of KCl"-area from a Sanicro 28 sample after 24-hour exposure at 600 °C in 5% O_2 + 20% H_2O under continuous KCl deposition.

The corrosion morphology of the samples with KCl(s) applied prior to exposure is consistent with the features observed on the samples exposed under continuous KCl deposition. In both cases the primary protection is lost by the presence of KCl(s), resulting in a thin oxide growing on top. The oxide layer is composed of two oxides, presumably two spinel oxides. The initiation of grain boundaries attack was also observed in the two types of exposure. Thus, the areas designated as "low amount of KCl"-areas exhibit corrosion features similar to the corresponding exposures where the salt had been applied prior to exposure.

Characterization of the "high amount of KCl"-area of Sanicro 28

In contrast to 304L, where the surface was covered mostly by large agglomerations of KCl(s) crystals, the surface morphology of Sanicro 28 consisted of potassium chromate, potassium chloride, and an oxide layer (Figure 34).
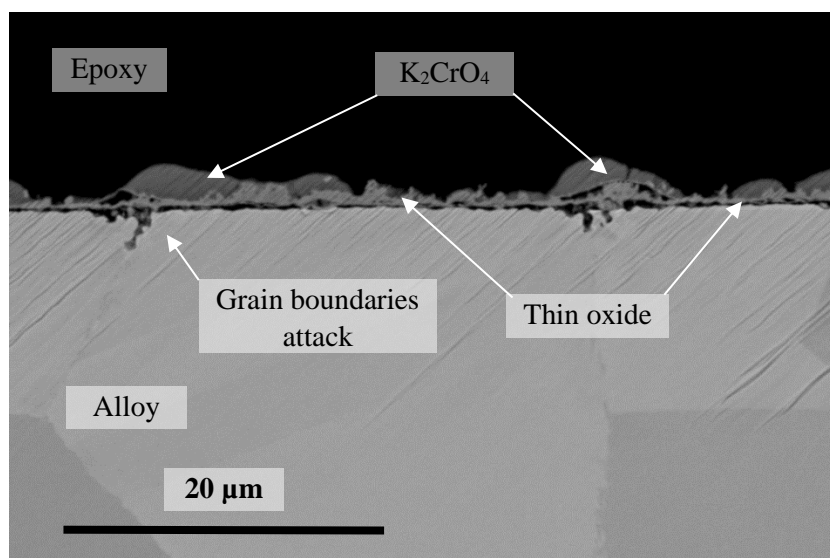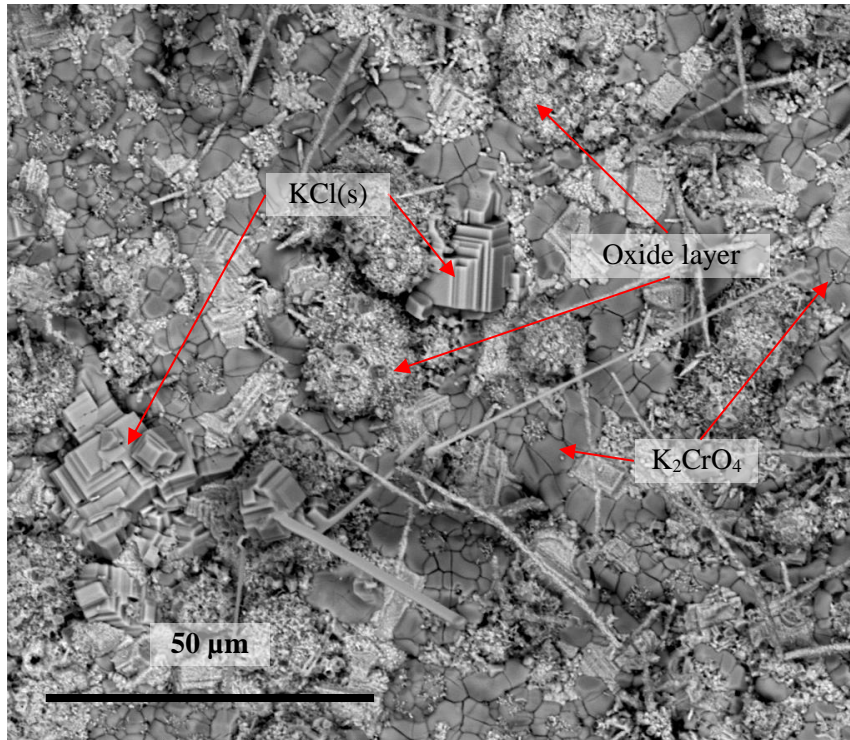
Figure 34: SEM image using BSE of the plan view of a "high amount of KCl"-area from a Sanicro 28 sample after 24-hour exposure at 600 °C in 5% O_2 + 20% H_2O under continuous KCl deposition.

The sample began to exhibit signs of breakaway oxidation as a thick oxide scale grew. This was confirmed with the cross-sectional view in Figure 35. The features of the corrosion morphology are more prominent, with grain boundaries attacks that reached a depth between 5 and 14 µm which is much deeper than the previous cases where 3 µm was the maximum depth.

Figure 35: SEM image using BSE of the cross section of a "high amount of KCl"-area from a Sanicro 28 sample after 24-hour exposure at 600 °C in 5% O_2 + 20% H_2O under continuous KCl deposition.

Figure 36 shows a more detailed image of the corrosion products/substrate interface. Potassium chromate and potassium chloride were detected on top of the corrosion products. In the "high amount of KCl"-area, the corrosion products consisted of two oxide layers:

- An outward-growing oxide layer (region between the blue dashed lines): a thickness varying between 600 and 1400 nm, and a composition of Cr (~21%), Fe (~63%) and Ni (~16%) in at%.

47

- An inward-growing oxide layer: a thickness varying between 1 and 6 µm, and a composition of Cr (~40%), Fe (~24%) and Ni (~36%) in at%.

A comparison of the outward-growing layers between "low and high amount of KCl"-areas shows that, the oxygen and iron contents increased. This process can continue until the layer becomes pure iron oxide, most likely hematite. For the inward-growing layers between "low and high amount of KCl"-areas, the iron content decreased while the nickel content increased (from "low" to "high amount of KCl"-area). The inward-growing oxide layer may become similar to the inward-growing spinel oxide seen in stainless steels as it was observed in section 9.1.1 for 304L. A small region located between the two oxide layers at the grain boundaries also appeared to be $(Fe,Cr)_2O_3$ in the EDX analysis Cr (~40%), Fe (~57%) and Ni (~4%) in at% and confirmed using XRD. Additionally, another region between the orange dashed lines corresponds to a nickel-rich area caused by the depletion of chromium and iron. This region has formed probably caused by the diffusion of iron and chromium had towards the inward-growing oxide layer. This nickel-rich region appears to be located under the inward-growing oxide layer. Only small amounts of chlorine were detected along the grain boundaries and the oxides.

The differences in corrosion morphology compared to 304L were thinner oxides, smaller grain boundaries attacks and nickel-rich inclusions in the inward growing oxide layer.

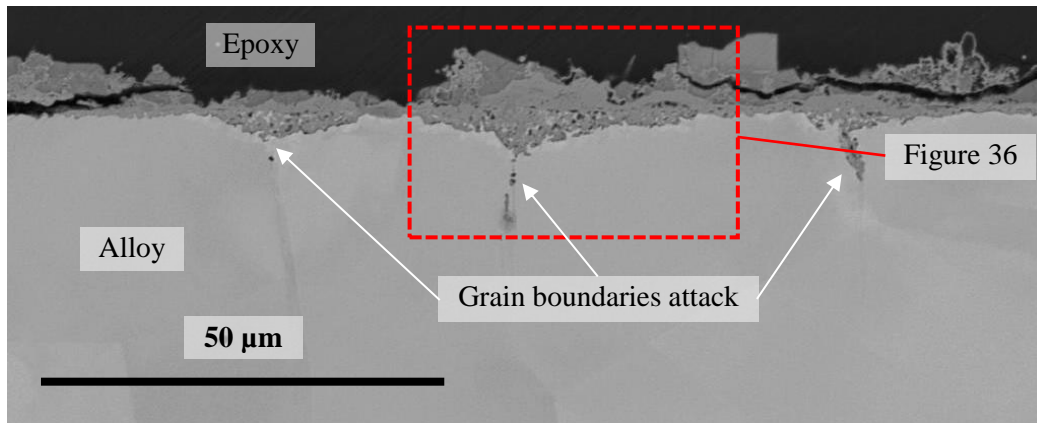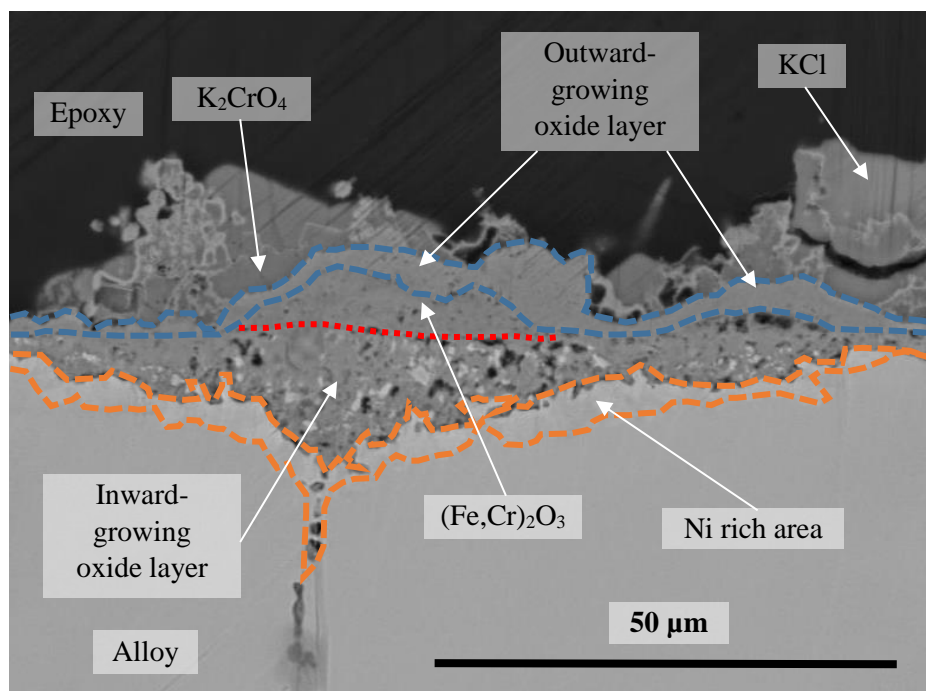*Figure 36: SEM image with higher magnification using BSE of the cross section of a "high amount of KCl"-area from a Sanicro 28 sample after 24-hour exposure at 600 °C in 5% O_2 + 20% H_2O under continuous KCl deposition.*

The grain boundaries attacks that started from the lowest parts of the inward-growing oxide layer exhibited voids and corrosion products. Therefore, during the corrosion attack, the inward-growing oxide layer continued to grow within the grain boundaries, resulting in deeper grain boundaries but also a wider attack as the grains began to oxidize on the sides of the grain boundaries. As an oxide continues to grow along the grain boundaries, it may also connect to other grain boundaries being oxidized, which

would lead to a connection of these oxides and the isolation of the grain (Figure 37b), as it was found for the 304L sample (Figure 26).
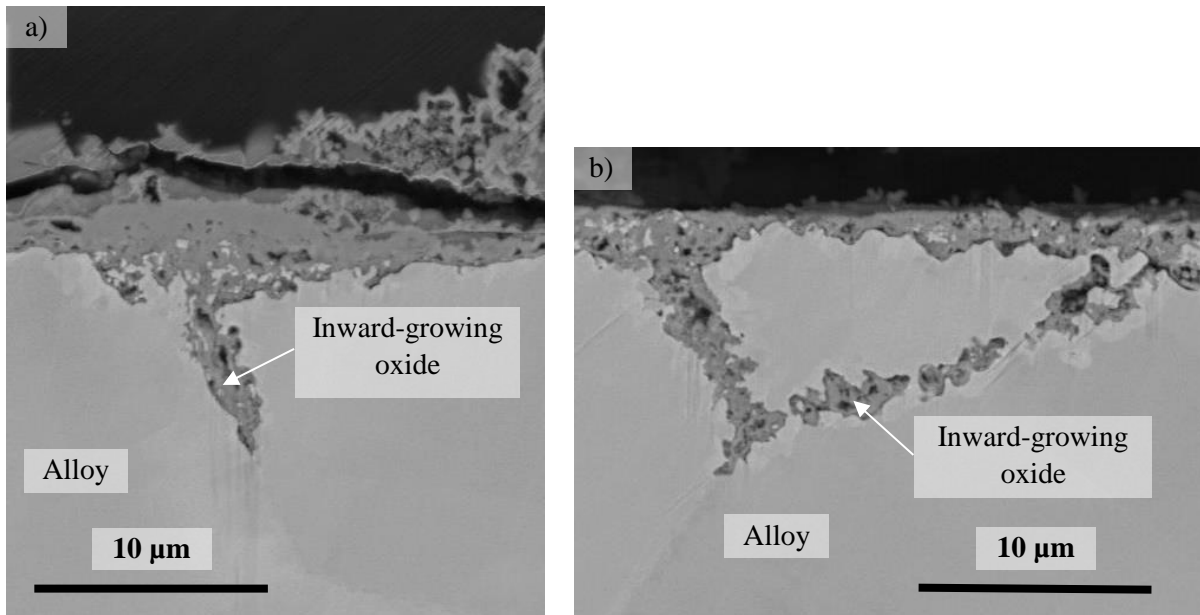
Figure 37: SEM image using BSE of the cross section of two other "high amount of KCl"-areas from a Sanicro 28 sample after 24-hour exposure at 600 °C in 5% O_2 + 20% H_2O under continuous KCl deposition showing a) growth of oxide along the grain boundaries and b) isolation of a grain by a connection of two grain boundaries attacks.

However, the corrosion front is not only located at the grain boundaries, internal corrosion seems to occur also within the grain creating a more uniform nickel-rich and iron/chromium-depleted front (Figure 38).
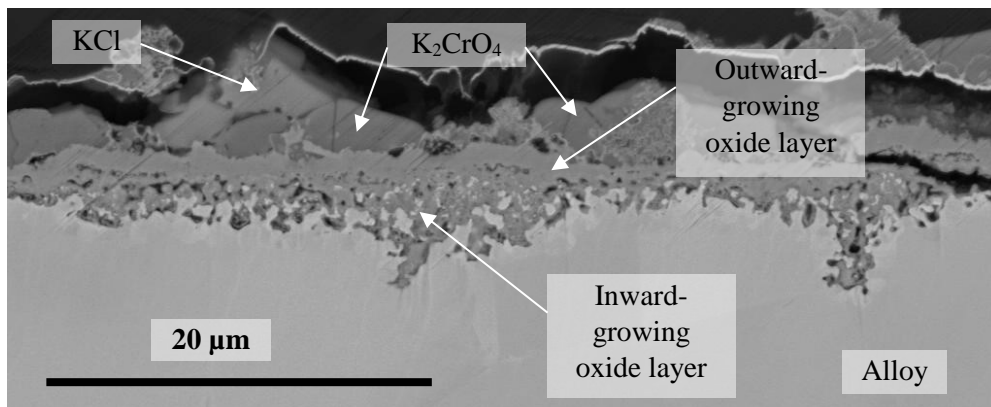
Figure 38: SEM image using BSE of the cross section of another "high amount of KCl"-area from a Sanicro 28 sample showing internal corrosion after 24-hour- exposure at 600 °C in 5% O_2 + 20% H_2O under continuous KCl deposition.

"Low amount of KCl"-areas for the Sanicro 28 samples exhibited corrosion features similar to previous studies that applied small amount of KCl(s) (0.1 mg/cm^2) onto the samples prior to exposure. These features include a thin oxide layer (secondary protection) and the initiation of grain boundaries attacks. However, the "high amount KCl"-areas displayed a more complex corrosion morphology that was characterized by the growth of two thin oxide layers, such as in the "low amount of KCl"-area, deeper grain boundaries attacks as well as internal corrosion within the grains.

9.2. Solutions for mitigation of corrosion

9.2.1. Mitigation of corrosion by improving materials: Coatings

It is well known that high-alloyed steels, which are considered as good corrosion resistant materials, are more expensive than low-alloyed steels, which are considered as low corrosion resistant materials. The price and the properties are directly linked to the different alloying elements added during the fabrication of the material. However, the additions, such as, Cr, Si, Al, and Ni, that improves the corrosion properties of the final material have an impact on the mechanical properties of the material usually in a negative way [70-72]. This results in shorter lifetimes, lower pressure-bearing capabilities, and reduced fabricability. Using high-alloyed steels as coatings is one compromise. The combination of the mechanical properties of a low-alloyed steel as a substrate with the corrosion properties of a high-alloyed steel could lead to an adequate solution, technically and economically.

The use of coatings for corrosion resistance has been previously investigated. These coatings have been made using different thermal spraying techniques, such as arc spray or High Velocity Oxy Fuel (HVOF). The characterization of the produced coatings, however, revealed numerous problems regarding porosity, oxide formation during spraying, and poor adhesion of the coating on the substrate. Such issues usually result in failure of the coating with respect towards corrosion resistance [25, 26]. Porosity plays a major role in coatings; the denser the coating, the better its performance. More recently, a new thermal spraying technique called High Velocity Air Fuel (HVAF) has been developed. This technique can produce coatings with low porosity, reduced oxide formation during spraying, and elemental loss [27, 73]. This is achieved due to lower temperatures and higher particle velocities [29, 73, 74].

The present study of the protectiveness of three different HVAF-sprayed coatings with different compositions (NiAl, NiCr and NiCrAlY) was conducted in two different laboratory environments: a mildly corrosive environment (consisting of O_2 + H_2O) and a highly corrosive environment (consisting of O_2 + H_2O + KCl). The study was performed using gravimetry and microstructural analyses. As these coatings are to be used in biomass- and waste-fired boilers, these environments were chosen due to the high level of water vapor and the amount of corrosive species present in these boilers.

A M3^{TM} HVAF gun was used to spray the three different coatings onto a 16Mo3 substrate. Grit blasting using aluminum oxide was performed prior to the thermal spraying in order to enhance the adhesion between the coating and the substrate. The remaining aluminum oxide could be observed at the coating/substrate interface.

Mildly corrosive environment: 5% O_2 + 20 % H_2O + N_2

In the absence of KCl, the samples exhibited mass gains between 0.1 and 0.2 mg/cm^2, see Figure 39. A sample of 304L was also exposed as a reference in this environment (without KCl) and showed lower mass gains than the coated samples. The mass gains of the coated samples decreased slightly from NiCr to NiAl and finally NiCrAlY. The oxide thicknesses calculated from the mass gains were considered to

be between 0.6 and 1.0 μm, considering nickel oxide (NiO) as the only oxide. However, the surfaces of the coated samples had a shiny appearance, which is a sign of a thin oxide in the order of 50 and 200 nm. This difference implies that oxidation within the coating occurred as no thick oxide could be found on the surface.
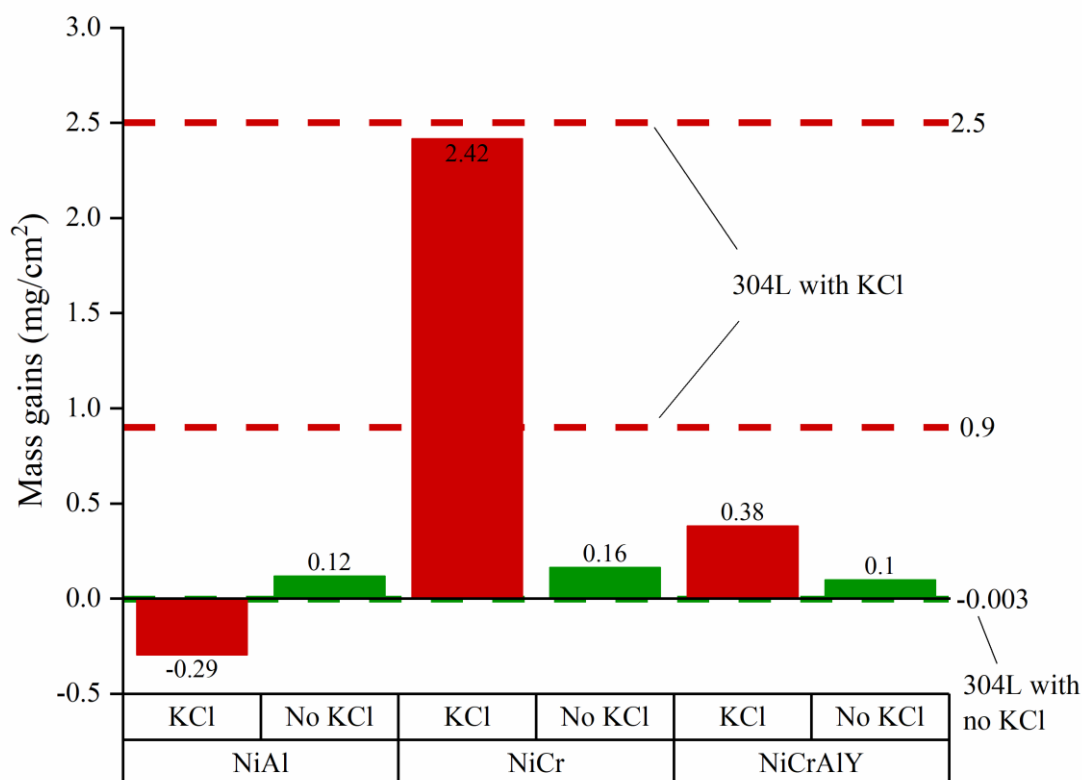
Figure 39: Mass gains of the coated samples after 168 hours exposure in 5% O_2 + 20% H_2O + N_2 at 600 °C with and without KCl. The dashed reference lines represent the mass gains of 304L in the presence of KCl (red dashed lines) and without it (green dashed line). The mass gains of 304L were calculated based on oxide thickness.

NiCr did not form a thick oxide on the surface, but oxygen was detected in the coating down to the coating/substrate interface (see Figure 40). As no oxygen was detected in the coating of a non-exposed sample (Figure 41), it can be concluded that oxide formation occurred during exposure and not during thermal spraying. The exposures of NiAl and NiCrAlY resulted in no signs of oxide formation within the coating (except for the aluminum oxide residues from the grit blasting). This implies that the mass gain measured was probably caused by flaws in the coatings, that induced local corrosion attacks (Figure 42 and Figure 43).

Consequently, NiCr cannot be considered as a good potential coating because oxide formation occurred within the coating in this mildly corrosive environment. In contrast, NiAl and NiCrAlY are more promising because thin and protective oxides on the surface were observed, and no oxide formation was seen within coatings.

Figure 40:SEM image using BSE of a cross section of a NiCr-coated sample after exposure in 5% O_2 + 20% H_2O + N_2 at 600 °C for 168 hours. The signal for oxygen from the EDX analysis is located at the bottom left of the picture. A higher magnification of an area of the coating is shown at the top right. The dashed line represents the coating/substrate interface.
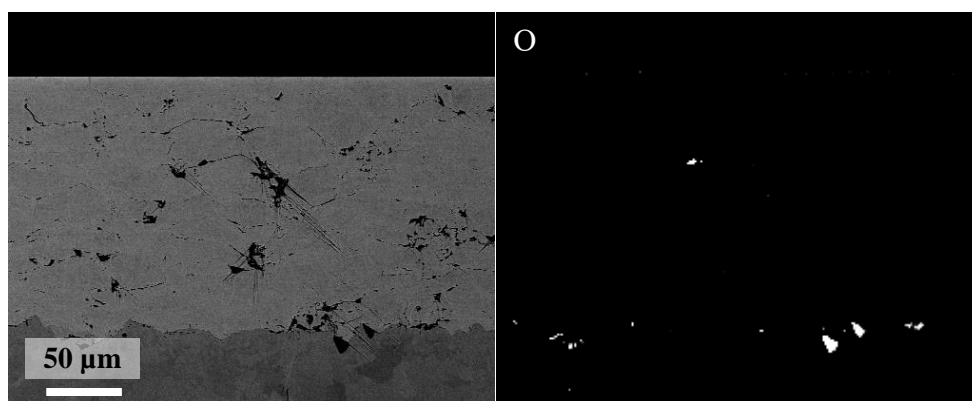
Figure 41: SEM image using BSE of a cross section of a non-exposed NiCr-coated sample (left) and the signal for oxygen from the EDX analysis of the area (right).
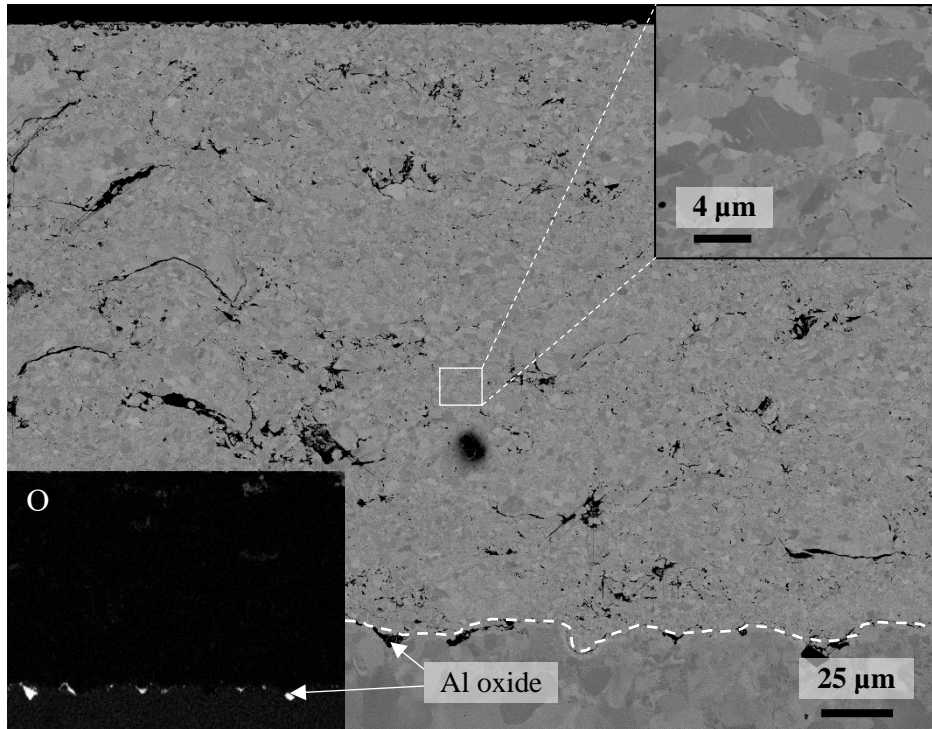
Figure 42: SEM image using BSE of a cross section of a NiAl-coated sample in 5% O_2 + 20% H_2O + N_2 at 600 °C for 168 hours. The signal for oxygen from the EDX analysis is located at the bottom left of the picture. A higher magnification of an area is shown at the top right. The dashed line represents the coating/substrate interface.

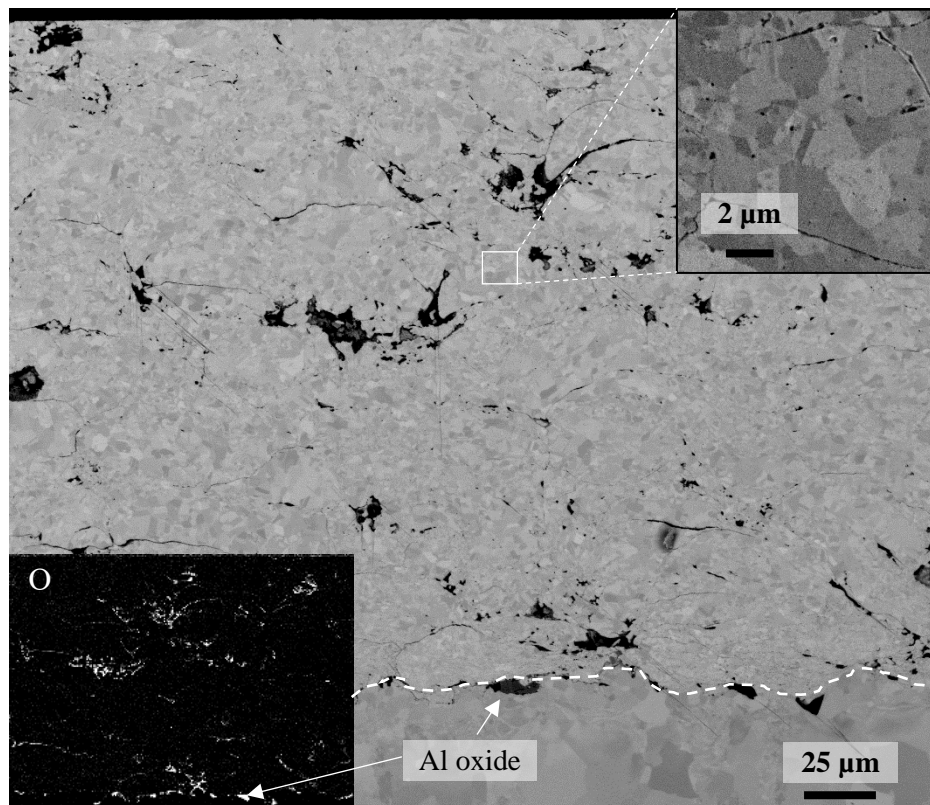*Figure 43: SEM image using BSE of a cross section of a NiCrAlY-coated sample in 5% O_2 + 20% H_2O + N_2 at 600 °C for 168 hours. The signal for oxygen from the EDX analysis is located at the bottom left of the picture. A higher magnification of an area is shown at the top right. The dashed line represents the coating/substrate interface.*
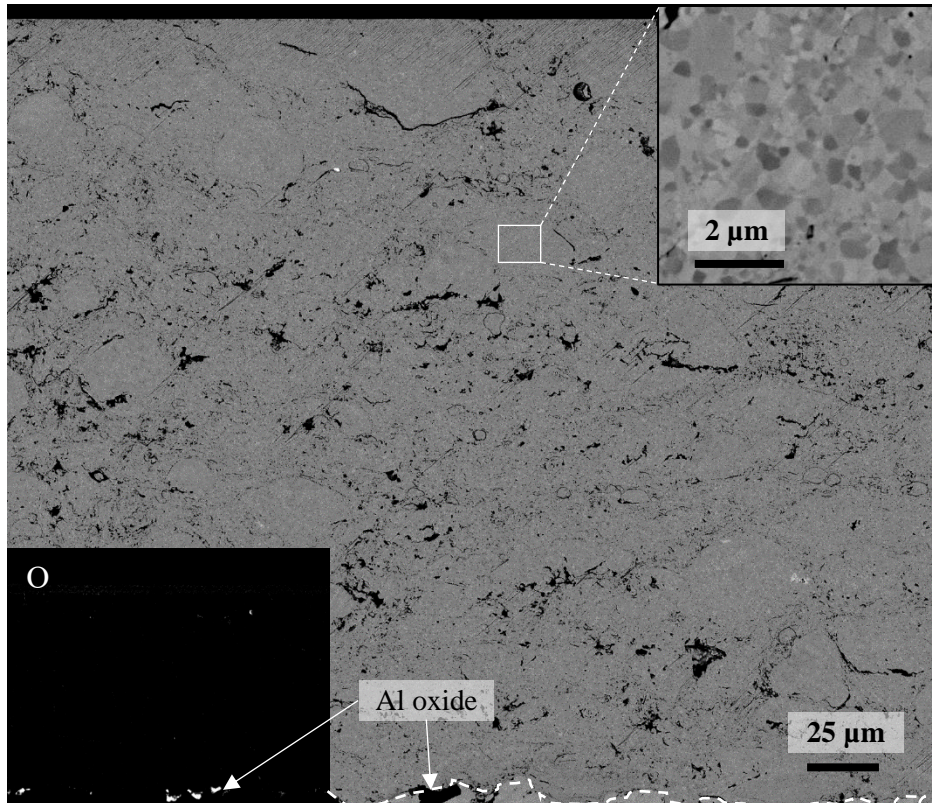
The microstructure of the coatings was quite similar with some porosity. The NiCr coating exhibited larger pores, mostly distributed along the splat boundaries. NiAl and NiCrAlY displayed smaller pores evenly distributed within the coating. It is well known that porosity plays a major role in corrosion resistance, as pores act as open doors for corrosive species. The amount of open or connected pores is an important parameter. It was assumed that a high number of closed pores would result in less severe corrosion than a large number of open pores, as the penetration of the corrosive species would be more tedious.

Grain size differed somewhat within the three coatings (Figure 40, Figure 42, and Figure 43). NiCr and NiAl exhibited grain sizes between 0.5 and 5 µm while NiCrAlY showed between 0.2 and 1 µm. Smaller grains influence the diffusion of chromium and/or aluminum towards the surface and promote the formation of chromia (Cr_2O_3) and alumina (Al_2O_3).

In coating applications, a common problem at high temperatures is the interdiffusion of alloying elements from the coating to the substrate [75]. This phenomenon not only leads to a depletion of elements that enhance the corrosion resistance of the coating (such as chromium and aluminum), but also to a decrease in mechanical strength at the interdiffusion zone [76]. This results in reduced pressure-bearing capabilities and spallation of the coating.

After the exposures to both environments, all three coatings exhibited an interdiffusion area at the coating/substrate interface, see Figure 44.
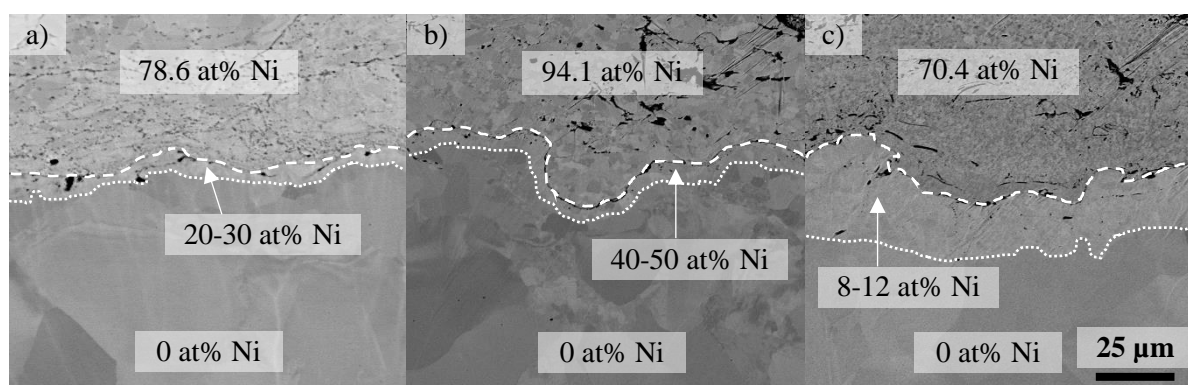
Figure 44: SEM images using BSE of cross-sections of a) NiCr coating, b) NiAl coating, and c) NiCrAlY coating at the coating/substrate interface, after an exposure in 5% O_2 + 20% H_2O + N_2 at 600 °C for 168 hours. The regions between the dashed lines are the austenitized areas.

The driving force was high as the substrate material 16Mo3 does not contain any nickel. EDX point analysis revealed that the NiAl sample had the highest nickel content in the interdiffusion zone with 40-50 at%, followed by the NiCr sample with 20-30 at% and the NiCrAlY sample with 8-12 at%. Not only does the nickel content differ among the samples at this interdiffusion zone but also the depth of this area. The NiCrAlY sample exhibited the deepest area compared to the two other coated samples.

Austenitization occurred due to the high nickel content in that zone. This could lead to mechanical issues caused by the higher coefficient of thermal expansion of the austenitic phase compared to the ferritic phase [77, 78]. Mechanical stresses would, therefore, be introduced during thermal cycling, which could cause spallation of the coating. The nickel content in the interdiffusion zone increased when the nickel

54

content in the coating increased. This is due to the gradient of nickel between the coating and the substrate that induces the driving force for diffusion: the more nickel content in a coating, the stronger the driving force. However, no negative effects of the interdiffusion on the performance of the coatings were observed for 168-hour exposures. It is, therefore, necessary to investigate this aspect further with thermal cycling and/or longer exposure times.

Highly corrosive environment: 5% O_2 + 20 %H_2O + N_2 + 1.0 mg/cm^2 KCl

The corrosion behavior of the three coatings tested in this study were also exposed to air at 600 °C with KCl for 168 hours [79]. The general trend in the study previously mentioned is that the coatings remain overall protective, however, the corrosion protection differed between the coatings. The NiCr coating formed an outward-growing oxide scale as well as an inward growing-oxide scale, reaching a depth of about 30 µm. For the NiCrAlY coating, a low corrosion attack was observed with only minor oxide formation. The NiAl coating exhibited good performance regarding corrosion resistance.

As water vapor and alkali chlorides are present simultaneously in flue gas during the combustion of biomass and waste [6, 80], it is relevant to include both of them in the simulated environment.

In the presence of KCl and water vapor, the mass gains are presented in Figure 39. The NiCr coating exhibited the highest mass gain with around 2.4 mg/cm^2, corresponding to a thickness of 17 µm. The NiCrAlY coating showed a lower mass gain compared to the NiCr coating with roughly 0.38 mg/cm^2, which corresponds to an oxide thickness of about 3 µm. In contrast to the other two coatings, the NiAl coating displayed a mass loss that implies that the oxidation rate was lower than the evaporation rate of the deposited KCl. As a comparison, the mass gains of 304L varied between 0.9 and 2.5 mg/cm^2 (calculated from the oxide thickness).

The high mass gain of NiCr can be explained by the presence of a thick oxide of 30-50 µm on the surface, which can be seen as two different layers (Figure 45). The EDX analysis revealed that the outermost layer was composed of a nickel- and a chromium-containing oxide, with potassium chromate (K_2CrO_4). The oxide layer beneath the outermost layer is composed of a porous chromium oxide. This oxide layer is outward growing, marked by a straight horizontal line at its base. Below this line, an inward-growing layer with a maximum thickness of about 15 µm was observed. It grew along the splat boundaries and was composed of nickel and chromium oxide. The presence of voids was also observed due to the separation of splats, resulting in wider inter-splat boundaries. This feature was observable up to 75 µm of depth. Chromium chlorides were detected deeper down in the coating, more specifically, at the splat boundaries (EDX map in Figure 45). Hence, Cl has diffused through the coating, towards the coating/substrate interface where metal chlorides have formed also within the substrate (Figure 46).

Figure 45: SEM image using BSE of a cross section of a NiCr-coated sample after exposure in 5% O_2 + 20% H_2O + N_2 + 1.0 mg/cm² at 600 °C for 168 hours. The signal for chlorine from the EDX analysis is located at the bottom left of the picture. A higher magnification of the thick oxide layer is shown at the top right. The dashed line represents the coating/substrate interface.

Figure 46: SEM image using BSE of a cross section of the coating/substrate interface of a NiCr-coated sample after exposure in 5% O_2 + 20% H_2O + N_2 + 1.0 mg/cm² at 600 °C for 168 hours. The signal for chlorine from the EDX analysis is located at the bottom left of the picture. The dashed line represents the coating/substrate interface.

The NiAl coating exhibited the lowest corrosion attack and did not form any thick oxide on the surface but a non-continuous aluminum oxide of 5 µm thickness, see Figure 47. No oxide formation nor chlorides were detected within the coating. This means that the aluminum oxide formed on top prevented species (e.g. chlorine) from penetrating the coating. Compared to the NiCr coating, no breakdown of the oxide scale on the surface was observed, i.e. the primary protection is still present on the NiAl coating. This is explained by KCl only reacting with a chromium-rich oxide and not an aluminum-rich oxide. However, the most protective form of aluminum oxide is α-Al_2O_3, which was not considered in this study because the exposure temperature would be too low for the formation of α-Al_2O_3. It was, therefore, assumed that a transient form of alumina γ-Al_2O_3 had formed. It has been shown that this transient form exhibits less corrosion resistance in the presence of KCl [81], however, in the present study, it exhibited a sufficiently protective behavior that prevented Cl penetration.
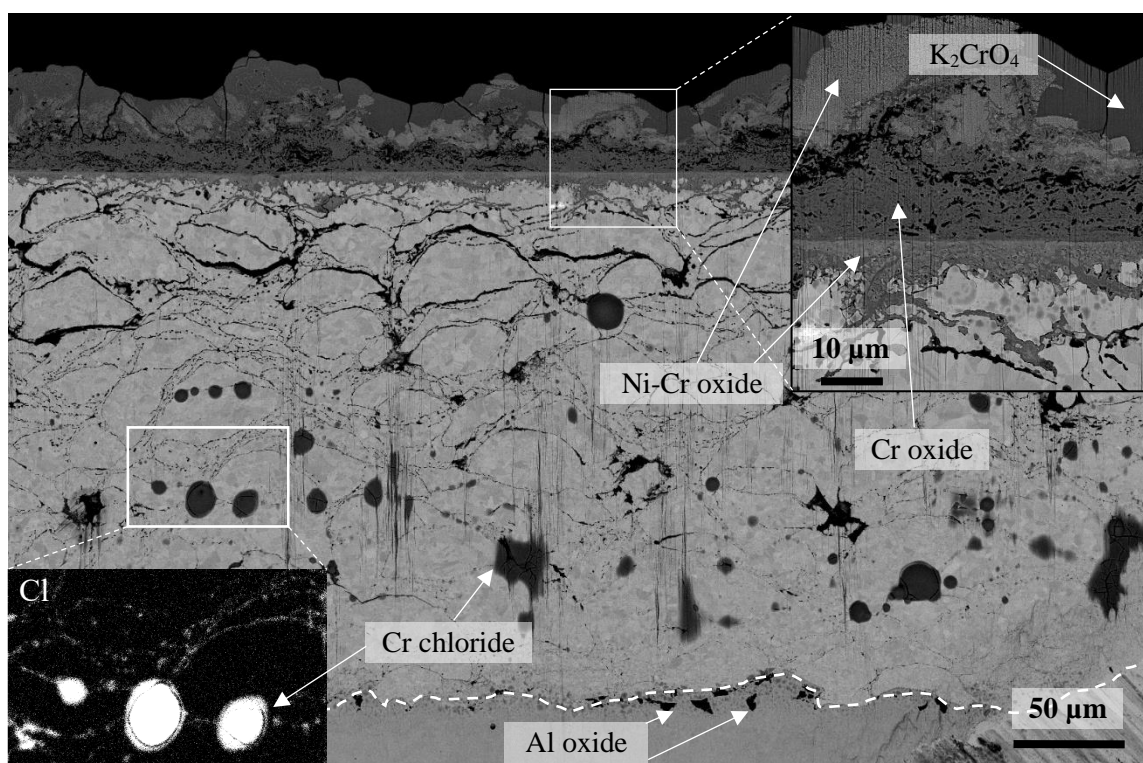

Figure 47: SEM image using BSE of a cross section of a NiAl-coated sample after exposure in 5% O_2 + 20% H_2O + N_2 + 1.0 mg/cm^2 at 600 °C for 168 hours. The dashed line represents the coating/substrate interface.

The overall corrosion resistance of NiCrAlY was much better than for NiCr but lower than NiAl. This is probably due to the presence of chromium in the coating; the chromium reacted with KCl to form K_2CrO_4 particles on the surface (Figure 48). An enrichment of chromium at the splat boundaries just beneath these particles was observed (EDX map in Figure 48). This was probably caused by the diffusion of chromium towards the surface, as this element was depleted due to the reaction with KCl. Despite the formation of potassium chromate, no thick oxide scale was formed on the surface. Furthermore, no sign of oxide formation nor chlorine penetration was observed within the coating. Consenquently, the thin oxide formed on the on the surface remained protective, preventing the intrusion and diffusion of corrosive species. Therefore, the NiCrAlY coating managed to protect the substrate from a corrosion attack. However, it is unknown how the performance of the coating would be affected by further depletion of chromium with longer exposure durations and larger amounts of KCl.

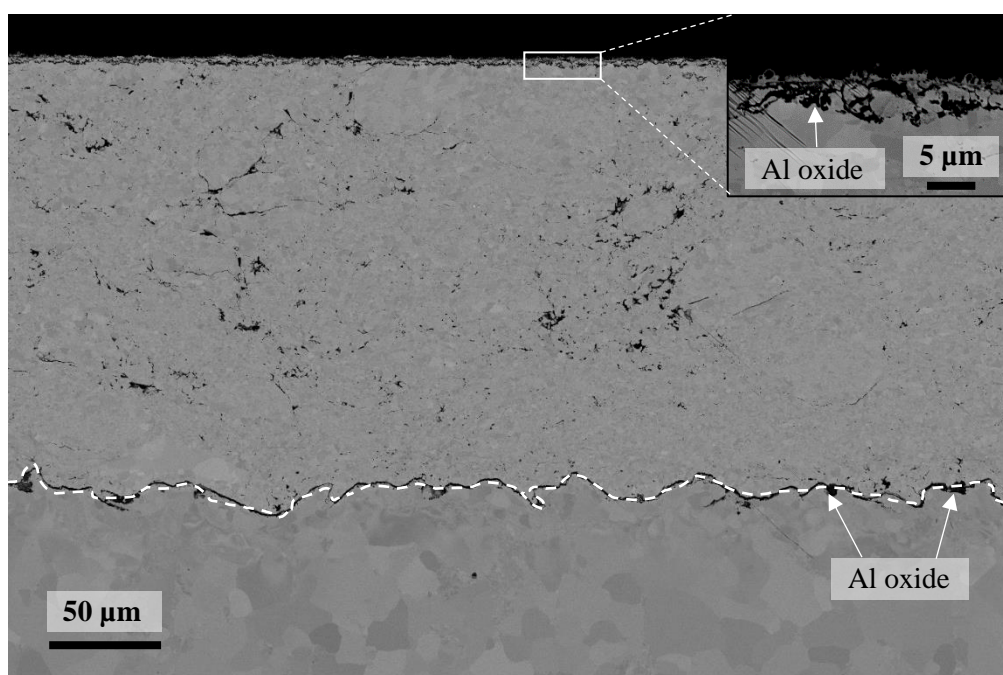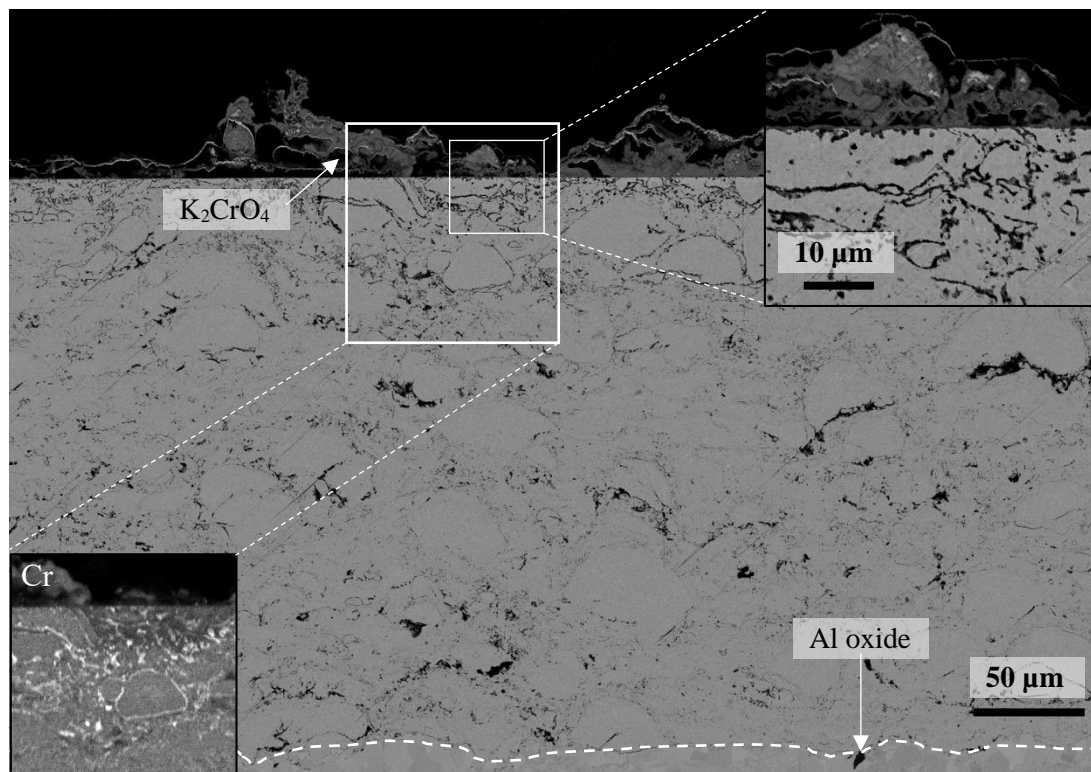*Figure 48: SEM image using BSE of a cross section of a NiCrAlY-coated sample after exposure in 5% O_2 + 20% H_2O + N_2 + 1.0 mg/cm² at 600 °C for 168 hours. The signal for chromium from the EDX analysis is located at the bottom left of the picture. A higher magnification of the surface is shown at the top right. The dashed line represents the coating/substrate interface.*

<u>Comments regarding thermal spraying techniques</u>

Porosity has always been a weakness for coatings. Pores must be kept to a minimum in order to obtain good performance of the final product. Other than HVAF, the thermal spraying techniques flame spraying, plasma spraying and HVOF have been analyzed as-sprayed [82]. It was found that the three techniques exhibited a lot of porosity compared to HVAF. However, it was also found that the spraying parameters of the HVOF techniques could be optimized to obtain a denser coating. T. Hussain et al. have characterized the microstructures of HVOF-sprayed coatings of different compositions, and found not only a large spread in porosity but also that the composition of the powders used has an impact on the final microstructure of the coating [83]. A previous study has compared the microstructure of as-sprayed HVOF and HVAF coatings with the same composition [84]. It was shown that the HVAF-sprayed coatings exhibited less porosity than the HVOF-sprayed coatings. Consequently, this novel HVAF technique seems to have the potential to produce a better corrosion protection.

The HVAF-sprayed coatings used in this thesis seemed to show more porosity than some HVOF- and plasma-sprayed coatings used in previous studies [82, 83, 85]. The reason behind this observation is suggested to be as follows: in the present study, mechanical polishing was not used to prepare the cross sections of the coatings, instead, BIB milling was used, which resulted in very smooth surfaces. The difference between mechanical polishing [86] and BIB milling is shown in Figure 49. It can be noticed that when BIB milling is used, more porosity appears as no potential plastic deformations caused by

58

mechanical polishing occurs, which probably makes the pores less visible. It is, consequently, difficult to directly compare the microstructure of the coatings prepared in these two different ways. However, regardless of cross-sectional technique, the observation underlines that the spraying parameters must be optimized in order to reduce porosity.
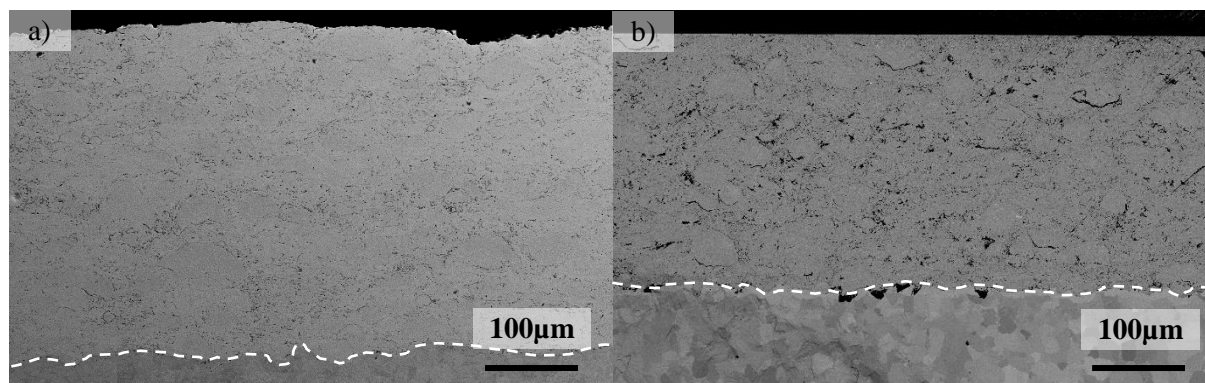
Figure 49: SEM image using BSE of the cross-section of the NiCrAlY coated sample after a) mechanical polishing and after b) broad ion milling (BIB). The dashed line indicates the coating/substrate interface.

9.3. Mitigation of corrosion by altering the environment of materials [87]

Field exposures are as important as laboratory exposures, and both of these are needed in order to fully understand the corrosion phenomena that occur in boilers and, subsequently, find adequate corrosion mitigation solutions. Field exposures are relevant as the materials tested are surrounded by the real environmental conditions, more complex and usually more corrosive than the simulated environment in a laboratory.

Two types of test are usually conducted in boilers to investigate corrosion:

- A deposit test: samples are exposed inside the boiler at the area of interest to collect ashes or deposits that are to be characterized.
- A corrosion test: the samples are exposed inside the boiler in order to generate new knowledge on the corrosion behavior of the materials.

9.3.1. Deposit tests

The deposits tests were performed in order to evaluate the influence of the boiler's settings on the chemical composition of the deposit at the new possible superheater position. 29 settings were tested by inserting probes inside the boiler for 2 hours to collect ashes and/or deposits. After each different setting, the samples were removed for characterization and photographs were taken for optical inspection. Ion Chromatography (IC) was performed in order to quantify the amount of corrosive species present within the deposits, and SEM/EDX was used on selected deposits in cross sections.

Figure 50 shows three different deposits on the samples. These range from a) a very small amount, to b) a moderate amount, and to c) a large amount. These different amounts of deposit were caused by the different boiler settings. The photograph in Figure 50c) shows a piece of hard deposit removed from the tip of the probe. In this manner, optical inspection gave insight into the influence of the boiler's settings on the amount of deposits accumulated on the materials at the new possible superheater position.

Figure 50: Photographs of three different amounts of deposits accumulated on Sanicro 28 for three different settings after 2-hour exposures. A) small amount, b) moderate amount, and c) large amount.

Ion Chromatography (IC)

It is well known that chlorine, alkali compounds, and sulfur are considered corrosive towards superheaters and, more specifically, stainless steels. Therefore, the analysis focused on these species in the deposit.

Figure 51 shows that the chlorine content in the deposits. The concentration of Cl varied between 3.5 at% for the setting with the least amount, and 20.9 at% for the setting with the highest amount. Figure 52 shows the amount of deposits collected for each setting. It is important to note that the amount of chlorine does not correlate to the amount of deposits. One of the settings marked in red (Figure 51 and Figure 52) was chosen during for the corrosion probe test. This setting shows a small amount of chlorine with very few deposits. Furthermore, the distribution of chlorine within the deposits was analyzed with SEM coupled with EDX.

The deposit analysis showed that the composition of the deposit was sensitive to the boiler's settings, and in this case, the settings over the grid. Natural variations in the flue gas composition/deposit formation occurred due to the variations in combustion and fuel. However, the large variations observed herein regarding the amount of deposits accumulated on the samples, and the amount of chlorine present within the deposits, show that the operation settings of a boiler do have an impact on the corrosiveness of the deposits at the new possible superheater position.
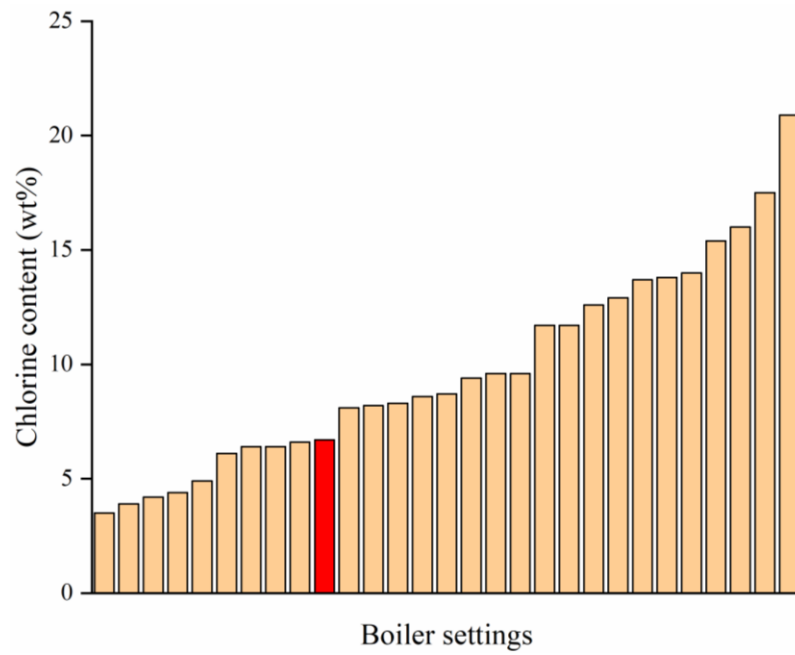
Figure 51: Chlorine content (wt%) in the deposits accumulated on an air-cooled probe at the Steamboost position, for the 29 different boiler settings for 2 hours.
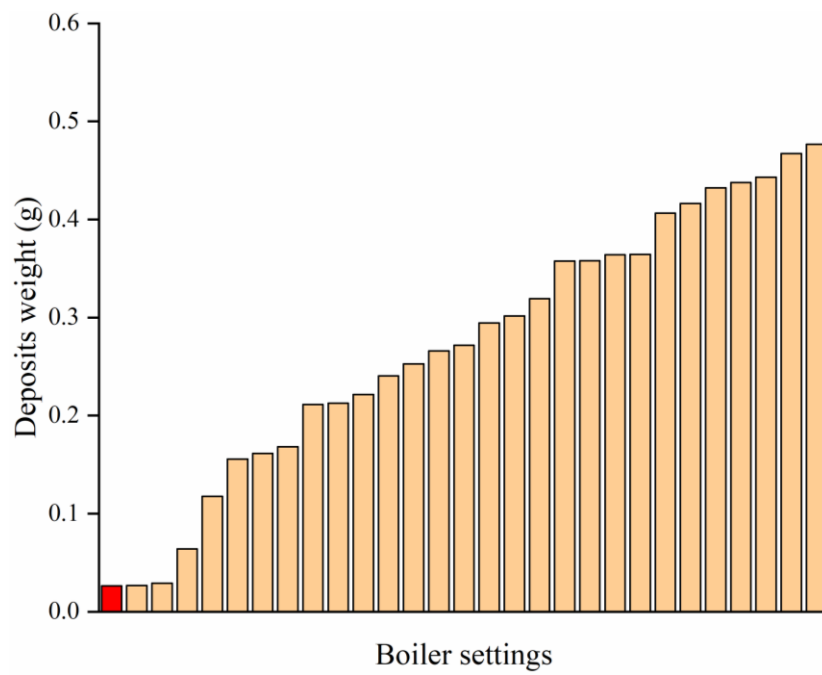

Figure 52: Amount of deposits accumulated on the air-cooled probe for the 29 different settings for 2 hours.

9.3.2. Corrosion tests

Corrosion tests were performed using corrosion probe exposure as well as a fixed installation consisting of three loops connected to the main steam of the plant and carrying several different superheater tubes welded together. The inlet temperature of the steam was 340 °C at the entrance to the first superheater loop and 470 °C at the outlet, resulting in a metal temperature of approximatively 525 °C. The fixed installation was exposed for 8000 hours.

Material loss was performed on the samples using ultrasound measurements in order to quantify the corrosion tests of the fixed installed materials. The thickness was measured at eight points on each sample along the ring using an Olympus 27MG ultrasonic thickness gage with a 0.01 mm resolution.

The present study focused on the fixed installed material 347H. The material loss is presented in Figure 53. The steam entered the inlet of the first loop at 340 °C and left the fixed installation via the outlet of the third loop at 470 °C. The material temperatures were estimated to be 395 °C at the inlet of the first loop and 525 °C at the outlet of the third loop. The material loss increased when the temperature increased (from loop 1 to loop 3).
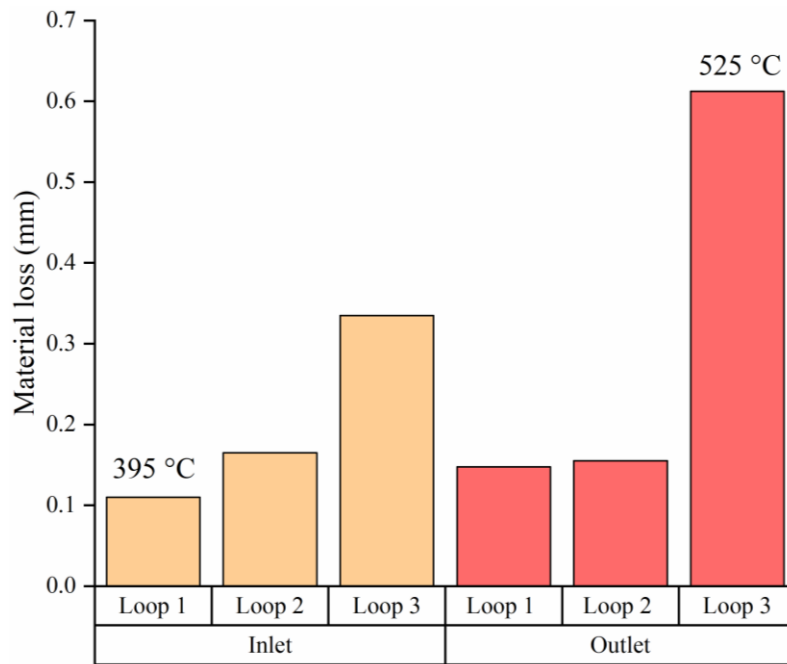
Figure 53: Material loss of 347H samples exposed at 600 °C at six different locations for 8000 hours.

The 347H sample exposed at the highest material temperature was analyzed in detail with microscopy investigation. The sample was exposed at the outlet of the third loop with a material temperature of approximatively 525 °C. Very small amounts of deposits were found on the sample as the boiler was cleaned before removing the sample. Figure 54 shows a SEM image acquired with the BSE of a representative area. A thick oxide scale of about 250 µm, consisting of a complex layered scale was observed. The EDX analysis shown in Figure 55 reveals that the outer parts were made of fully oxidized Fe-Cr scale with some areas/alloy grains in the middle that were not oxidized. A grain boundaries attack

was seen at the scale/substrate interface, where nickel enrichment seemed to occur in the alloy. The steel grain boundaries attack is in good agreement with the features observed in lab-scale exposures using continuous deposition of KCl on 304L (see Section 9.1.1.).

Indications of alkali chromates were confirmed with EDX point analysis. Low chlorine concentrations were also detected in the corrosion products. The overall observation is that the 347H sample was in a breakaway regime which correlates well with the material loss measurements. As described in Section 6.2, the chromium from the protective layer (primary protection) may react with the alkali compounds to form alkali chromates, depleting the protective layer of chromium. This leads to a fast-growing iron oxide (secondary protection). Only low levels of metal chlorides were detected at the metal/oxide interface. This also correlates well with the deposit tests where small amounts of chlorine were detected in the deposits.

Figure 54: SEM image using BSE of 347H material exposed in the outlet of loop 3 at the Steamboost position for 8000 hours.
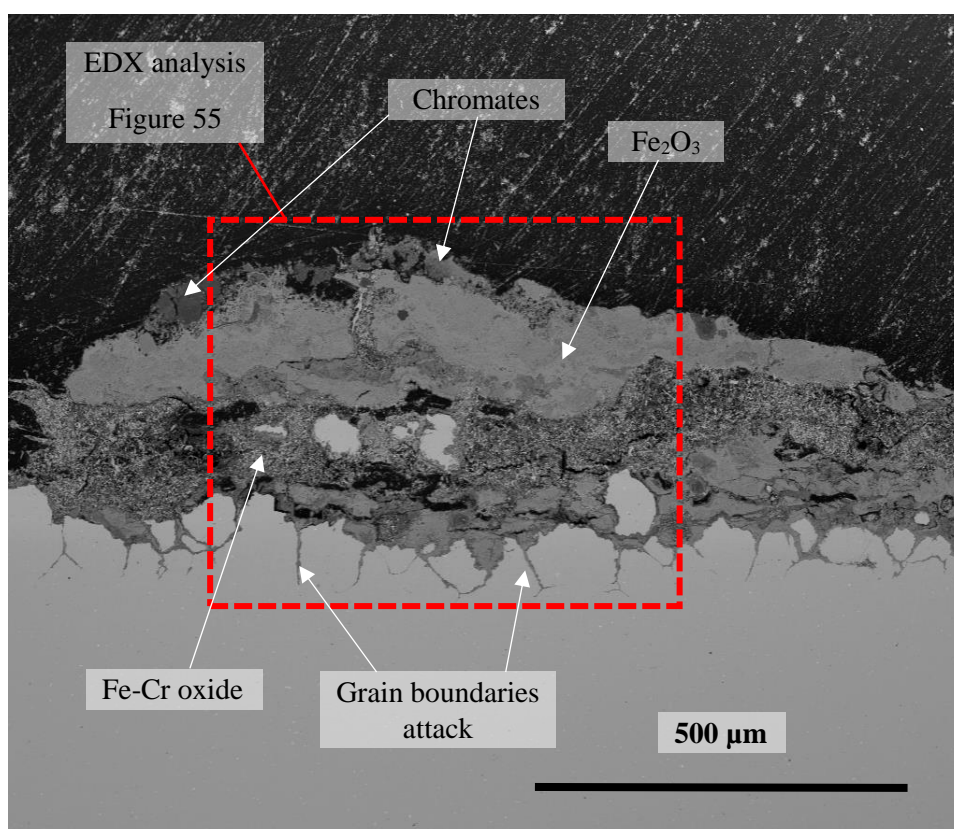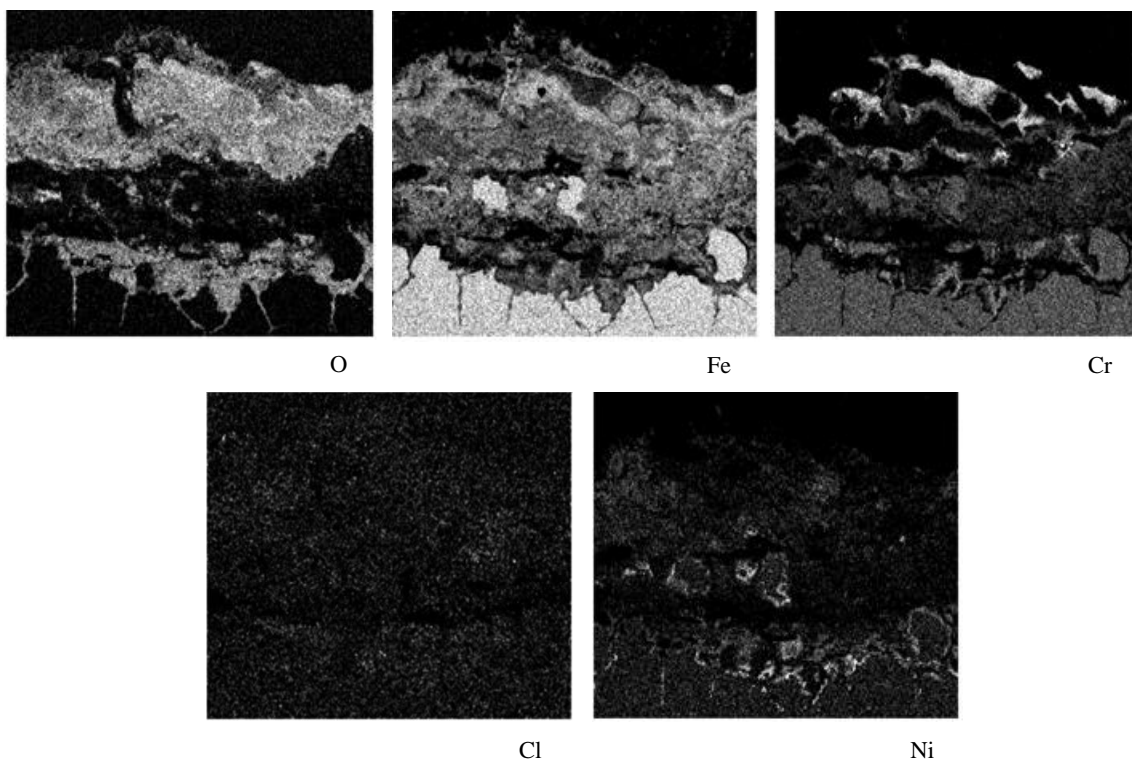
O

Fe

Cr

Cl

Ni

Figure 55:EDX analysis of the marked area in Figure 54.

10. Conclusions and Future Work

10.1. Investigation of accelerated corrosion caused by continuous KCl addition

This study focused on a laboratory setup with continuous deposition of KCl on the surfaces of two stainless steels: 304L and Sanicro 28. A new setup was developed, and the deposition was characterized over time as well as over the sample. The setup generated a deposit rate on the sample's surface with heterogeneous amounts of deposited KCl(s). Part of the samples showed a corrosion morphology similar to samples with small amounts of KCl(s) deposited prior to exposure, i.e. breakaway followed by oxidation of secondary protection. In contrast with the previous method of spraying salt on the samples prior to exposure, more areas of the sample's surface suffered from severe corrosion attack. The corrosion attack of 304L could be divided into mainly two major areas:

- An area with small amounts of KCl(s) that caused breakaway corrosion and secondary protection.
- An area with large amounts of KCl(s) that caused faster corrosion rates and grain boundaries attack.

Moreover, the corrosion morphology observed on the regions with large amounts of KCl(s) on the 304L sample is more similar to the corrosion features (e.g. grain boundaries attack) observed in samples exposed to a boiler environment, e.g. as observed in the field exposure of 347H.

The morphology and type of corrosion attack on the Sanicro 28 (Ni- and Cr-rich alloy) was similar to the 304L samples. However, the corrosion resistance was improved compared to 304L. An improved secondary protection is suggested to enhance the corrosion resistance of Sanicro 28 (Ni- and Cr-rich alloy). For both materials, the overall corrosion attack was more severe than the previous studies that deposited KCl(s) *ex-situ* prior to exposure.

Thus, this newly developed setup may, in a better way, simulate the boiler corrosion attack in a laboratory environment.

Future work using this method will provide new knowledge on the propagation of corrosion and accelerated corrosion by performing longer exposures in a simulated boiler environment. The mechanisms that link grain boundaries attack with the amount/way of depositing KCl will be investigated through detailed electron microscopy. The influence of Cr and Ni on the corrosion resistance of stainless steels in this newly developed environment will be investigated as well using model alloys.

10.2. Solutions for mitigation of corrosion

10.2.1. Mitigation of corrosion by improving materials: Coatings

The aim of this study was to evaluate the performance of three different nickel-based coatings HVAF-sprayed on a low-alloyed steel when exposed to two different environments.

Regardless of the type of environment, several features were found:
- The three coatings showed good adhesion to the substrate without any signs of spallation.
- A region of interdiffusion was observed at the coating/substrate interface, where nickel diffused from the coating towards the substrate, leading to austenitization of the area. A higher nickel content in a coating resulted in a higher content of nickel in the interdiffusion region.

In the mildly corrosive environment (5% O_2 + 20% H_2O + N_2 at 600 °C), all three coatings formed a thin protective oxide on top. However, the NiCr sample showed signs of oxide formation within the coating.

In the highly corrosive environment (5% O_2 + 20% H_2O + N_2 + 1.0 mg/cm^2 KCl at 600 °C), the level of corrosion attack differed among the coatings:
- The NiCr sample exhibited a high level of corrosion attack, resulting in the formation of a thick oxide on top of the coating, as well as chlorine penetration that reached the coating/substrate interface.
- The NiAl and NiCrAlY samples showed signs of good corrosion resistance with no chlorine penetration.

Future research on the three coatings will investigate of the coating/substrate adhesion by performing thermal cycling tests, as the interdiffusion zone could cause issues attributable to mechanical stresses. Longer exposures in a harsh environment must also be performed to study the influence of the depletion of chromium from the coating on its performance.

10.2.2. Mitigation of corrosion by altering the environment of materials

The purpose of this study was to investigate the corrosiveness of a potentially new position for superheaters in a boiler. This concept has been labelled "Steamboost". Previous CFD calculations indicated that this position should exhibit a milder environment [59], for this reason, deposit tests and corrosion tests were conducted.
- The deposit investigation showed that it is possible to influence both the amount as well as the corrosiveness of the deposit formed at the new superheater position over the grid, by optimizing boiler settings.
- The corrosion investigation showed that at the highest temperature of the fixed installation, the 347H stainless steel loses its protectiveness and enters the breakaway regime. The morphology

of the grain boundaries attacks is in good agreement with the lab-scale exposure using continuous deposition of KCl.

Overall, the data acquired during the field exposures linked to CFD calculations indicate a new potential position for superheaters. However, the variations in fuel during combustion coupled with the complex processes that occur over the grid make the study more complex. Therefore, future work regarding the Steamboost position is need in order to understand the influence of the position on corrosion mechanisms.

References

1. *NASA - Global Climate Change*. Available from: https://climate.nasa.gov/.
2. *Paris Agreement - COP 21*. Available from: https://ec.europa.eu/clima/policies/international/negotiations/paris_en.
3. *A sustainable energy and climate policy for the environment, competitiveness and long-term stability*. Available from: https://www.iea.org/policiesandmeasures/pams/sweden/name-42459-en.php.
4. Karlsson, S., L.-E. Åmand and J. Pettersson. *Reducing high temperature corrosion when burning waste by adding digested sewage sludge*. in *Swedish-Finnish Flame Days, January 26-27 2011 in Piteå, Sweden, The Swedish and Finnish National Committees of the International Flame Research Foundation (IFRF) and The Scandinavian-Nordic Section of the Combustion Institute (SNCI)*. 2011.
5. Kassman, H., L. Bäfver and L.-E. Åmand, *The importance of SO2 and SO3 for sulphation of gaseous KCl – An experimental investigation in a biomass fired CFB boiler*. Combustion and Flame, 2010. **157**(9): p. 1649-1657.
6. Kassman, H., M. Broström, M. Berg and L.-E. Åmand, *Measures to reduce chlorine in deposits: Application in a large-scale circulating fluidised bed boiler firing biomass*. Fuel, 2011. **90**(4): p. 1325-1334.
7. Kassman, H., J. Pettersson, B.-M. Steenari and L.-E. Åmand, *Two strategies to reduce gaseous KCl and chlorine in deposits during biomass combustion—injection of ammonium sulphate and co-combustion with peat*. Fuel Processing Technology, 2013. **105**: p. 170-180.
8. Li, Y., P. Murphy and C.-Y. Wu, *Removal of elemental mercury from simulated coal-combustion flue gas using a SiO2–TiO2 nanocomposite*. Fuel Processing Technology, 2008. **89**(6): p. 567-573.
9. Nielsen, H.P., F.J. Frandsen and K. Dam-Johansen, *Lab-scale investigations of high-temperature corrosion phenomena in straw-fired boilers*. Energy & Fuels, 1999. **13**(6): p. 1114-1121.
10. Nielsen, H.P., F.J. Frandsen, K. Dam-Johansen and L.L. Baxter, *The implications of chlorine-associated corrosion on the operation of biomass-fired boilers*. Progress in Energy and Combustion Science, 2000. **26**(3): p. 283-298.
11. Davidsson, K.O., L.-E. Åmand, B. Leckner, B. Kovacevik, M. Svane, M. Hagström, J.B.C. Pettersson, J. Pettersson, H. Asteman, J.-E. Svensson and L.-G. Johansson, *Potassium, Chlorine, and Sulfur in Ash, Particles, Deposits, and Corrosion during Wood Combustion in a Circulating Fluidized-Bed Boiler*. Energy & Fuels, 2007. **21**(1): p. 71-81.
12. Folkeson, N., J. Liske, C. Pettersson, L.-G. Johansson, E. Skog, B. Å. Andersson, S. Enestam, J. Tuiremo, A. Jonasson, B. Heikne and J.-E. Svensson, *Fireside Corrosion of Stainless and Low Alloyed Steels in a Waste-Fired CFB Boiler; The Effect of Adding Sulphur to the Fuel*. Vol. 595-598. 2008. 289-297.
13. Grabke, H.J., E. Reese and M. Spiegel, *The effects of chlorides, hydrogen chloride, and sulfur dioxide in the oxidation of steels below deposits*. Corrosion Science, 1995. **37**(7): p. 1023-1043.
14. Karlsson, S., L.-E. Åmand and J. Liske, *Reducing high-temperature corrosion on high-alloyed stainless steel superheaters by co-combustion of municipal sewage sludge in a fluidised bed boiler*. Fuel, 2015. **139**: p. 482-493.
15. Kiamehr, S., K.V. Dahl, M. Montgomery and M.A.J. Somers, *KCl-induced high temperature corrosion of selected commercial alloys*. Materials and Corrosion, 2015. **66**(12): p. 1414-1429.
16. Lehmusto, J., D. Lindberg, P. Yrjas and L. Hupa, *The Effect of Temperature on the Formation of Oxide Scales Regarding Commercial Superheater Steels*. Oxidation of Metals, 2018. **89**(1): p. 251-278.
17. Lehmusto, J., P. Yrjas, B.J. Skrifvars and M. Hupa, *High temperature corrosion of superheater steels by KCl and K2CO3 under dry and wet conditions*. Fuel Processing Technology, 2012. **104**: p. 253-264.

18.   Okoro, S.C., S. Kiamehr, M. Montgomery, F.J. Frandsen and K. Pantleon, *Effect of flue gas composition on deposit induced high temperature corrosion under laboratory conditions mimicking biomass firing. Part I: Exposures in oxidizing and chlorinating atmospheres.* Materials and Corrosion, 2017. **68**(5): p. 499-514.

19.   Okoro, S.C., M. Montgomery, F.J. Frandsen and K. Pantleon, *High temperature corrosion during biomass firing: improved understanding by depth resolved characterisation of corrosion products.* Materials at High Temperatures, 2015. **32**(1-2): p. 92-101.

20.   Pettersson, J., N. Folkeson, L.-G. Johansson and J.-E. Svensson, *The Effects of KCl, K2SO4 and K2CO3 on the High Temperature Corrosion of a 304-Type Austenitic Stainless Steel.* Oxidation of Metals, 2011. **76**(1): p. 93-109.

21.   Sui, J., J. Lehmusto, M. Bergelin and M. Hupa, *The Effects of KCl, NaCl and K2CO3 on the High-Temperature Oxidation Onset of Sanicro 28 Steel.* Oxidation of Metals, 2016. **85**(5): p. 565-598.

22.   Pettersson, J., H. Asteman, J.-E. Svensson and L.-G. Johansson, *KCl Induced Corrosion of a 304-type Austenitic Stainless Steel at 600°C; The Role of Potassium.* Oxidation of Metals, 2005. **64**(1): p. 23-41.

23.   Lai, G.Y., *High-temperature corrosion and materials applications.* 2007: ASM international.

24.   Karlsson, S., E. Larsson, T. Jonsson, J.-E. Svensson and J. Liske, *A Laboratory Study of the in Situ Sulfation of Alkali Chloride Rich Deposits: Corrosion Perspective.* Energy & Fuels, 2016. **30**(9): p. 7256-7267.

25.   Hjörnhede, A. and A. Nylund, *Adhesion testing of thermally sprayed and laser deposited coatings.* Surface and Coatings Technology, 2004. **184**(2): p. 208-218.

26.   Hjörnhede, A., P. Sotkovszki and A. Nylund, *Erosion-corrosion of laser and thermally deposited coatings exposed in fluidised bed combustion plants.* Materials and Corrosion, 2006. **57**(4): p. 307-322.

27.   Sadeghimeresht, E., J. Eklund, J.P. Simon, J. Liske, N. Markocsan and S.V. Joshi, *Effect of water vapor on the oxidation behavior of HVAF-sprayed NiCr and NiCrAlY coatings.* Materials and corrosion - Werkstoffe und Korrosion, 2018. **69**(10): p. 1431-1440.

28.   Sadeghimeresht, E., N. Markocsan and P. Nylén, *Microstructural and electrochemical characterization of Ni-based bi-layer coatings produced by the HVAF process.* Surface and Coatings Technology, 2016. **304**: p. 606-619.

29.   Zeng, Z., N. Sakoda, T. Tajiri and S. Kuroda, *Structure and corrosion behavior of 316L stainless steel coatings formed by HVAF spraying with and without sealing.* Surface and Coatings Technology, 2008. **203**(3): p. 284-290.

30.   Peña, J.A.P., *Bubbling Fluidized Bed (BFB), When to use this technology?* Industrial Fluidization South Africa, 2011: p. 1-12.

31.   *From resource economy to bioeconomy.* Available from: https://sweden.se/climate/#from-resource-economy-to-bioeconomy.

32.   Värme, E.O., *Change of fuel composition from 1991 to 2017 in Händeloverket.* 2018, E.On internal data.

33.   Kofstad, P., *High Temperature Corrosion.* 1988. 558.

34.   *Ellingham Diagram.* [cited 2018 18/06]; Available from: https://www.doitpoms.ac.uk/tlplib/ellingham_diagrams/ellingham.php.

35.   West, A.R., *Basic solid state chemistry.* 1999: John Wiley & Sons.

36.   Callister, W.D., *Materials Science And Engineering: An Introduction.* 2007: John Wiley & Sons.

37.   Khanna, A.S., *Introduction to High Temperature Oxidation and Corrosion.* 2002: ASM International.

38.   Heitjans, P. and J. Kärger, *Diffusion in condensed matter: methods, materials, models.* 2006: Springer Science & Business Media.

39.   Wagner, C., *Beitrag zur Theorie des Anlaufvorgangs*, in *Zeitschrift für Physikalische Chemie.* 1933. p. 25.

40.   Bhadeshia, H. and R. Honeycombe, *Steels: Microstructure and Properties.* 2017: Elsevier Science.

41.   Jones, D.A., *Principles and Prevention of Corrosion.* 1996: Prentice Hall.

42.   Jonsson, T., S. Karlsson, H. Hooshyar, M. Sattari, J. Liske, J.-E. Svensson and L.-G. Johansson, *Oxidation After Breakdown of the Chromium-Rich Scale on Stainless Steels at High Temperature: Internal Oxidation.* Oxidation of Metals, 2016. **85**(5): p. 509-536.

43.   Jonsson, T., B. Pujilaksono, H. Heidari, F. Liu, J.E. Svensson, M. Halvarsson and L.G. Johansson, *Oxidation of Fe–10Cr in O2 and in O2+H2O environment at 600°C: A microstructural investigation.* Corrosion Science, 2013. **75**: p. 326-336.

44.   Zahs, A., M. Spiegel and H. Jürgen Grabke, *Chloridation and oxidation of iron, chromium, nickel and their alloys in chloridizing and oxidizing atmospheres at 400–700°C.* Vol. 42. 2000. 1093-1122.

45.   Pettersson, C., T. Jonsson, C. Proff, M. Halvarsson, J.-E. Svensson and L.-G. Johansson, *High Temperature Oxidation of the Austenitic (35Fe27Cr31Ni) Alloy Sanicro 28 in O2 + H2O Environment.* Vol. 74. 2010. 93-111.

46.   Jonsson, T., S. Canovic, F. Liu, H. Asteman, J.E. Svensson, L.G. Johansson and M. Halvarsson, *Microstructural investigation of the effect of water vapour on the oxidation of alloy 353 MA in oxygen at 700 and 900°C.* Materials at High Temperatures, 2005. **22**(3-4): p. 231-243.

47.   Halvarsson, M., J.E. Tang, H. Asteman, J.E. Svensson and L.G. Johansson, *Microstructural investigation of the breakdown of the protective oxide scale on a 304 steel in the presence of oxygen and water vapour at 600°C.* Corrosion Science, 2006. **48**(8): p. 2014-2035.

48.   Asteman, H., J.-E. Svensson and L.-G. Johansson, *Evidence for Chromium Evaporation Influencing the Oxidation of 304L: The Effect of Temperature and Flow Rate.* Oxidation of Metals, 2002. **57**(3): p. 193-216.

49.   Asteman, H., K. Segerdahl, J.-E. Svensson and L.-G. Johansson, *The Influence of Water Vapor on the Corrosion of Chromia-Forming Steels.* Vol. 369-372. 2001. 277-286.

50.   Jenkins, B.M., L.L. Baxter, T.R. Miles and T.R. Miles, *Combustion properties of biomass.* Fuel Processing Technology, 1998. **54**(1): p. 17-46.

51.   Vassilev, S.V., D. Baxter, L.K. Andersen, C.G. Vassileva and T.J. Morgan, *An overview of the organic and inorganic phase composition of biomass.* Fuel, 2012. **94**: p. 1-33.

52.   Viklund, P., *Superheater corrosion in biomass and waste fired boilers : Characterisation, causes and prevention of chlorine-induced corrosion*, in *Trita-CHE-Report*. 2013, KTH Royal Institute of Technology: Stockholm. p. 55.

53.   McNallan, M., W. Liang, S. Kim and C. Kang. *Acceleration of the high temperature oxidation of metals by chlorine*. in *International Corrosion Conference Series*. 1983. NACE.

54.   Abels, J.M. and H.H. Strehblow, *A surface analytical approach to the high temperature chlorination behaviour of inconel 600 at 700 °C.* Corrosion Science, 1997. **39**(1): p. 115-132.

55.   Zahs, A., M. Spiegel and H.J. Grabke, *Chloridation and oxidation of iron, chromium, nickel and their alloys in chloridizing and oxidizing atmospheres at 400–700°C.* Corrosion Science, 2000. **42**(6): p. 1093-1122.

56.   Folkeson, N., L.-G. Johansson and J.-E. Svensson, *Initial Stages of the HCl-Induced High-Temperature Corrosion of Alloy 310.* Journal of The Electrochemical Society, 2007. **154**(9): p. C515-C521.

57.   Folkeson, N., T. Jonsson, M. Halvarsson, L.-G. Johansson and J.-E. Svensson, *The influence of small amounts of KCl(s) on the high temperature corrosion of a Fe-2.25Cr-1Mo steel at 400 and 500°C.* Vol. 62. 2011. 606-615.

58.   Sutton, A.P. and R.W. Balluffi, *Interfaces in crystalline materials*. 1995: Clarendon Press.

59.   Madsen, O.H., *Next Generation of Waste Fired Power Plants - Getting the most out of your trash!*, in *NAWTEC15-3205*. 2007: Miami, Florida USA.

60.   Paz, L., J. Pother-Simon, T. Jonsson and L. Mikkelsen, *Increased steam temperature with Steamboost superheater - The effect of the combustion in deposits and high temperature corrosion*. 2017.

61.   Cullity, B.D. and S.R. Stock, *Elements of X-ray Diffraction*. 2014: Pearson Education.

62.   Smart, L.E. and E.A. Moore, *Solid state chemistry: an introduction*. 2016: CRC press.

63.   Zhou, W., R. Apkarian, Z.L. Wang and D. Joy, *Fundamentals of scanning electron microscopy (SEM)*, in *Scanning microscopy for nanotechnology*. 2006, Springer. p. 1-40.

64. Shinata, Y., *Accelerated oxidation rate of chromium induced by sodium chloride.* Oxidation of Metals, 1987. **27**(5): p. 315-332.

65. Wang, C.-J. and T.-T. He, *Morphological Development of Subscale Formation in Fe–Cr–(Ni) Alloys with Chloride and Sulfates Coating.* Oxidation of Metals, 2002. **58**(3): p. 415-437.

66. Viklund, P., R. Pettersson, A. Hjörnhede, P. Henderson and P. Sjövall, *Effect of sulphur containing additive on initial corrosion of superheater tubes in waste fired boiler.* Corrosion Engineering, Science and Technology, 2009. **44**(3): p. 234-240.

67. Enestam, S., D. Bankiewicz, J. Tuiremo, K. Mäkelä and M. Hupa, *Are NaCl and KCl equally corrosive on superheater materials of steam boilers?* Fuel, 2013. **104**: p. 294-306.

68. Okoro, S.C., M. Montgomery, F.J. Frandsen and K. Pantleon, *Time and Temperature Effects on Alkali Chloride Induced High Temperature Corrosion of Superheaters during Biomass Firing.* Energy & Fuels, 2018. **32**(7): p. 7991-7999.

69. Proff, C., T. Jonsson, C. Pettersson, J.-E. Svensson, L.-G. Johansson and M. Halvarsson, *Microstructural investigation of the KCl-induced corrosion of the austenitic alloy Sanicro 28 (35Fe27Cr31Ni) at 600 C.* Materials at High Temperatures, 2009. **26**(2): p. 113-125.

70. Chen, S. and L. Rong, *Effect of silicon on the microstructure and mechanical properties of reduced activation ferritic/martensitic steel.* Journal of Nuclear Materials, 2015. **459**: p. 13-19.

71. Field, K.G., M.A. Snead, Y. Yamamoto and K.A. Terrani, *Handbook on the Material Properties of FeCrAl Alloys for Nuclear Power Production Applications.* 2017.

72. Song, L., E. Guo, L. Wang and D. Liu, *Effects of Silicon on Mechanical Properties and Fracture Toughness of Heavy-Section Ductile Cast Iron.* Metals, 2015. **5**(1): p. 150.

73. Sadeghi, E. and N. Markocsan, *Electrochemical Behavior of Bilayer Thermal-Spray Coatings in Low-Temperature Corrosion Protection.* Vol. 7. 2017.

74. Sadeghimeresht, E., N. Markocsan, P. Nylén and S. Björklund, *Corrosion performance of bi-layer Ni/Cr2C3–NiCr HVAF thermal spray coating.* Applied Surface Science, 2016. **369**: p. 470-481.

75. Pint, B.A., Y. Zhang, J.A. Haynes and I.G. Wright, *High temperature oxidation performance of aluminide coatings.* environments, 2003. **9**: p. 12.

76. Texier, D., D. Monceau, Z. Hervier and E. Andrieu, *Effect of interdiffusion on mechanical and thermal expansion properties at high temperature of a MCrAlY coated Ni-based superalloy.* Surface and Coatings Technology, 2016. **307**: p. 81-90.

77. Cverna, F., *Thermal properties of metals.* ASM International, Materials Park, OH, 2002.

78. Totten, G.E., *Handbook of residual stress and deformation of steel.* 2002: ASM international.

79. Jafari, R., E. Sadeghimeresht, T.S. Farahani, M. Huhtakangas, N. Markocsan and S. Joshi, *KCl-induced high-temperature corrosion behavior of HVAF-sprayed Ni-based coatings in ambient air.* Journal of Thermal Spray Technology, 2018. **27**(3): p. 500-511.

80. Steinmetz, P. and C. Rapin. *Corrosion of metallic materials in waste incinerators.* in *Materials science forum.* 1997. Trans Tech Publ.

81. Israelsson, N., *High Temperature Oxidation and Chlorination of FeCrAl Alloys.* 2014: Chalmers University of Technology.

82. Moskowitz, L., *Application of HVOF thermal spraying to solve corrosion problems in the petroleum industry—an industrial note.* Journal of Thermal Spray Technology, 1993. **2**(1): p. 21-29.

83. Hussain, T., T. Dudziak, N. Simms and J. Nicholls, *Fireside corrosion behavior of HVOF and plasma-sprayed coatings in advanced coal/biomass co-fired power plants.* Journal of thermal spray technology, 2013. **22**(5): p. 797-807.

84. Sadeghimeresht, E., N. Markocsan and P. Nylen, *Microstructural characteristics and corrosion behavior of HVAF-and HVOF-sprayed Fe-based coatings.* Surface and Coatings Technology, 2017. **318**: p. 365-373.

85. Varis, T., D. Bankiewicz, P. Yrjas, M. Oksa, T. Suhonen, S. Tuurna, K. Ruusuvuori and S. Holmström, *High temperature corrosion of thermally sprayed NiCr and FeCr coatings covered with a KCl–K2SO4 salt mixture.* Surface and Coatings Technology, 2015. **265**: p. 235-243.

86.   Sadeghimeresht, E., L. Reddy, T. Hussain, M. Huhtakangas, N. Markocsan and S. Joshi, *Influence of KCl and HCl on high temperature corrosion of HVAF-sprayed NiCrAlY and NiCrMo coatings.* Materials & Design, 2018. **148**: p. 17-29.

87.   Mikkelsen, L., T. Jonsson, L. Paz, J. Eklund, J. Liske, B. Jonsson, N. Israelsson, S. Selin, J. Hernblom, J. Högberg and J. Nockert Olovsjö, *Increased steam temperature in grate fired boilers - Steamboost*, in *KME 709*. 2017. p. 113.